



HAL
open science

Reflection control techniques of a plane wave using transformation optics and surface impedance modulation - Application to the flattening of the retro-directive reflector

Hassan Haddad

► **To cite this version:**

Hassan Haddad. Reflection control techniques of a plane wave using transformation optics and surface impedance modulation - Application to the flattening of the retro-directive reflector. Networking and Internet Architecture [cs.NI]. INSA de Rennes; Université Libanaise - Liban, 2018. English. NNT : 2018ISAR0025 . tel-02122834

HAL Id: tel-02122834

<https://theses.hal.science/tel-02122834>

Submitted on 7 May 2019

HAL is a multi-disciplinary open access archive for the deposit and dissemination of scientific research documents, whether they are published or not. The documents may come from teaching and research institutions in France or abroad, or from public or private research centers.

L'archive ouverte pluridisciplinaire **HAL**, est destinée au dépôt et à la diffusion de documents scientifiques de niveau recherche, publiés ou non, émanant des établissements d'enseignement et de recherche français ou étrangers, des laboratoires publics ou privés.

THESE DE DOCTORAT DE

L'INSA RENNES

COMUE UNIVERSITE BRETAGNE LOIRE

ECOLE DOCTORALE N° 602
*Mathématiques et Sciences
et Technologies*

de l'Information et de la Communication
Spécialité : *Télécommunications*

L'UNIVERSITÉ
LIBANAISE

*Ecole Doctorale de Sciences et
Technologies*

Par

Hassan HADDAD

Techniques de contrôle de la réflexion d'une onde plane à l'aide de l'optique de transformation et la modulation d'impédance de surface – Application à l'aplatissement du réflecteur rétro-directif

Thèse sera présentée et soutenue à Rennes, le 27/11/2018

Unités de recherche: IETR, UMR 6164 / LaSTRe, EDST, UL

Rapporteurs avant soutenance :

Géneviève MAZE-MERCEUR
Directeur de recherche, CEA-CESTA (HDR)
Eric LHEURETTE
Professeur, université de Lille 1

Composition du Jury :

Elodie RICHALOT / Présidente du Jury
Professeur à l'université Paris-Est Marne-la-Vallée
Géneviève MAZE-MERCEUR
Directeur de recherche, CEA-CESTA (HDR) / Rapporteur
Eric LHEURETTE
Professeur, université de Lille 1 / Rapporteur
Renaud LOISON
Professeur à l'INSA de Rennes / Directeur de thèse
Akil JRAD
Professeur à l'Université Libanaise / Co-directeur de thèse
Raphaël GILLARD
Professeur à l'INSA de Rennes / Co-encadrant
Ali HARMOUCH
Maître de Conférences à l'Université Libanaise / Co-encadrant / Invité

Intitulé de la thèse :

Techniques de contrôle de la réflexion d'une onde plane à l'aide de l'optique de transformation et la modulation d'impédance de surface - Application à l'aplatissement du réflecteur rétro-directif.

Hassan HADDAD

En partenariat avec :



Université Libanaise

École Doctorale
Sciences et Technologies

EDST, Université Libanaise

Document protégé par les droits d'auteur

Résumé

Table des matières

1.	Introduction.....	2
2.	Réflecteur Diédrique comprimé en utilisant l'optique de Transformation.....	3
3.	Réflecteur Diédrique comprimé en utilisant une combinaison de l'OT et la MIS	5
4.	Atténuation des réflexions parasites sur les panneaux MIS.....	6
5.	Modulation d'impédance de surface généralisée et son application pratique.....	8
6.	Conclusion	10

1. Introduction

Le réflecteur rétro-directif passif est un moyen simple et efficace pour obtenir la rétro-réflexion dans le domaine des hyperfréquences. Il est utilisé pour des nombreuses applications radar et antenne. Ces dernières années, un intérêt croissant est porté aux réflecteurs rétro-directifs aplatis [14,15, 43-46]. Les travaux proposent de minimiser l'épaisseur t du réflecteur diédrique conventionnel, trop encombrant pour s'intégrer dans certaines applications. Il faut noter que ses performances en Surface Equivalente Radar (SER) mono-statique (angle d'observation identique à celui de l'incidence) doivent être conservées pour toute épaisseur t comme indiqué dans la fig. 1.

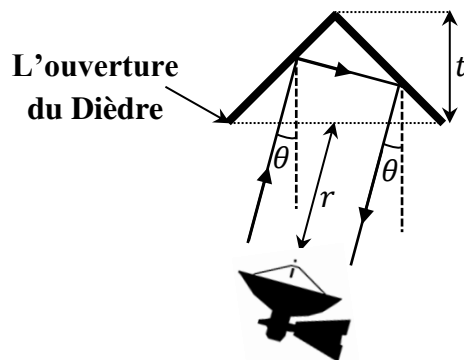


Figure 1. Concept de SER mono-statique dans une direction spécifique θ pour le réflecteur diédrique conventionnel.

Ainsi, nos contributions dans cette thèse comprennent l'exploration de différents domaines de recherche qui pourraient conduire à des profils plus faibles pour ce réflecteur. Au début, on explore l'utilisation de l'optique de transformation (OT) qui peut modifier son volume de remplissage.

Tout d'abord, en utilisant l'OT une transformation de coordonnées est effectuée pour apporter la distorsion souhaitée de l'espace. L'OT se base sur ce qu'on peut appeler l'invariance des équations de Maxwell [7]. Cela signifie qu'elle fournit une méthode pour modifier les paramètres constitutifs de l'espace physique (le volume qui remplit le dièdre dans notre cas) afin de simuler un milieu de propagation virtuellement distordu.

Les recherches conduites, en utilisant l'OT, sur l'aplatissement du réflecteur diédrique visent obtenir un profil aplati comme dans [14, 15]. Bien que très attrayantes, elles requièrent des matériaux très élaborés et ne pourraient se faire qu'au prix d'une réalisation très complexe.

D'autre part, la modulation d'impédance de surface (MIS) est une approche possible qui introduit une distribution d'impédance sur les panneaux d'un tel dispositif. Cette méthode consiste à utiliser des lois de phase bien spécifiques sur les surfaces des deux panneaux. Pour la mise en œuvre d'une telle méthode, des cellules passives déphaseuses, imprimées sur un substrat diélectrique disposé au-dessus d'un plan de masse sont utilisées à la place des panneaux métalliques mis en œuvre pour le réflecteur classique. Même si cette méthode n'est pas capable de réaliser un réflecteur parfaitement planaire, elle est facilement réalisable et dans [43-46] différents prototypes sont fabriqués et prouvent le concept.

Alors que la recherche qui adopte cette approche est capable de réduire le profil volumineux du réflecteur conventionnel, elle dégrade ses performances de rétro-directivité. Cela est dû aux panneaux MIS utilisés qui sont très sensibles à l'angle d'incidence.

On examine, au cours de cette thèse, la possibilité de combiner ces deux domaines de recherches (TO et MIS) pour minimiser les inconvénients de chacun.

La deuxième partie de cette thèse étudie les réflexions parasites, qui constituent l'un des inconvénients cachés des panneaux SIM. L'examen de l'historique de développement associé à ces réflexions parasites [47-50], fournit des explications à leur origine, ainsi que de nouvelles solutions pour les atténuer.

Enfin, on propose une implémentation pratique pour un réglage spécifique de la modulation d'impédance de surface généralisée. Une telle modulation utilise des impédances complexes capables de surpasser un panneau implémentant la modulation classique (MIS avec des impédances imaginaires pures).

2. Réflecteur Diédrique comprimé en utilisant l'optique de Transformation

Une nouvelle implémentation de l'OT est proposée pour concevoir un réflecteur diédrique comprimé (cf. fig. 2).

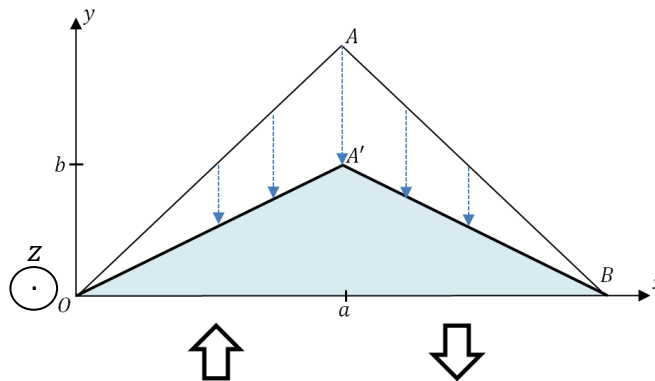


Figure 2. L'espace 2D (OAB) d'un réflecteur diédrique avec sa transformation proposée ($OA'B$).

En utilisant la procédure de l'OT, il faut un milieu anisotrope mais homogène pour remplir le volume du dièdre transformé ($\epsilon'_x = \mu'_x = \epsilon'_z = \mu'_z = \frac{a}{b}$, $\epsilon'_y = \mu'_y = \frac{b}{a}$).

En plus, ce dispositif montre qu'aucune loi physique de réflexion n'est violée durant le processus (puisque l'on garde la forme classique des équations de Maxwell). Par contre, on modifie les amplitudes de champ ($|E'_0| = \frac{a}{b}|E_0|$) lors de la réflexion comme illustré sur la fig. 3.

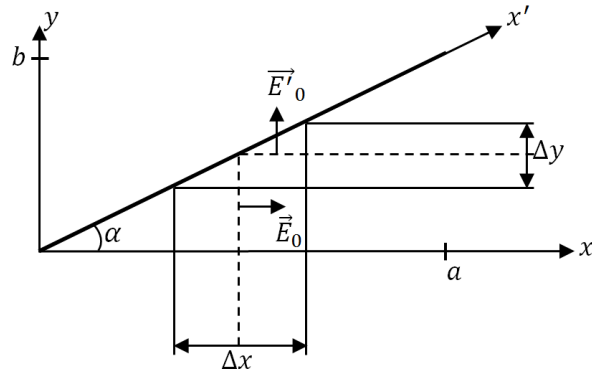


Figure 3. Propagation d'onde dans un réflecteur comprimé utilisant un milieu OT.

Des simulations avec COMSOL Multiphysics confirment que la rétro-directivité attendue est parfaitement atteinte pour une incidence normale. Ceci est illustré pour deux différents taux de compression sur la fig. 4.

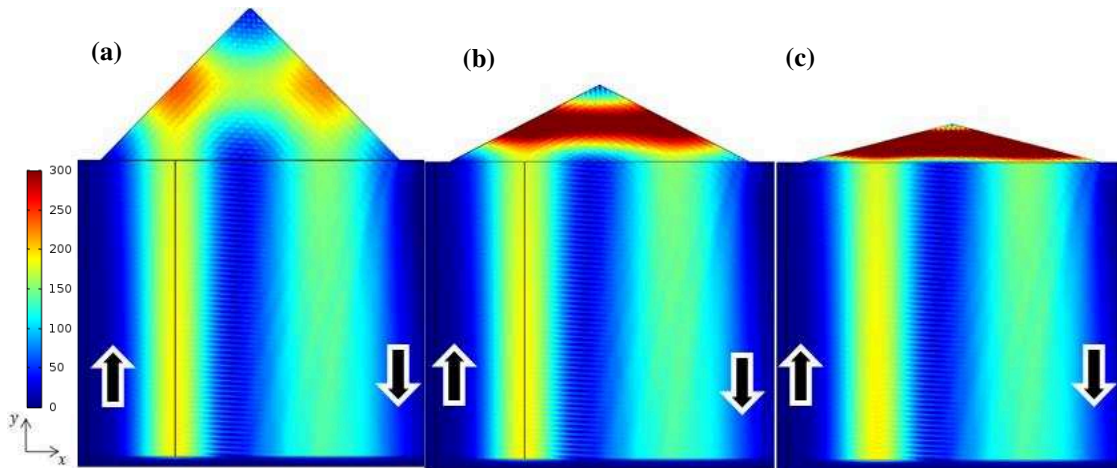


Figure 4. Amplitudes du champ électrique totale (en V/m) en incidence normale pour le dièdre classique (a), réflecteur comprimé utilisant OT pour $a = 2b$ (b) et $a = 4b$ (c).

De plus, dans le cas de la polarisation TM, un matériau non magnétique (ayant les composantes suivantes $\epsilon'_x = \epsilon'_z = \frac{a^2}{b^2}$, $\epsilon'_y = \mu'_x = \mu'_y = \mu'_z = 1$) peut être utilisé [54]. De légères pertes dues à la désadaptation sur l'interface entre l'air et le milieu OT sont inévitables dans ce cas mais elles peuvent toujours être atténuées en utilisant une couche d'adaptation placée sur l'ouverture du dièdre comprimé.

Par la suite, une implémentation pratique est discutée. Elle comprend un système à double couches [57] (avec $\epsilon_1 = 7,464$ et $\epsilon_2 = 0,5359$). Des études de convergence montrent que pour une épaisseur des couches, de l'ordre de $\lambda_g/70$, le comportement obtenu se rapproche du matériau anisotrope voulu. Les simulations COMSOL donnent des résultats prometteurs même pour une épaisseur $\lambda_g/50$ avec un coefficient de réflexion $\Gamma = -17,43\text{dB}$.

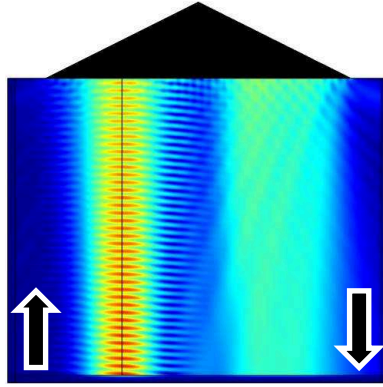


Figure 5. Amplitudes du champ électrique totale (en V/m) en incidence normale pour le dièdre comprimé ($a = 2b$) à système double couches avec 50 couches/ λ_g .

Alors que le système à double couches reproduit les performances du dièdre classique et permet d'atteindre une compression importante de ses dimensions, sa réalisation pratique reste encore irréaliste (à cause du nombre élevé de couches par λ_g).

3. Réflecteur Diédrique comprimé en utilisant une combinaison de l'OT et la MIS

Une nouvelle approche de compression des réflecteurs diédriques est présentée. Elle combine l'OT et la MIS, fournissant un outil unifié pour contrôler l'onde réfléchie d'un dièdre en agissant à la fois sur sa surface et sur les propriétés de son volume comme présenté dans la fig. 6.

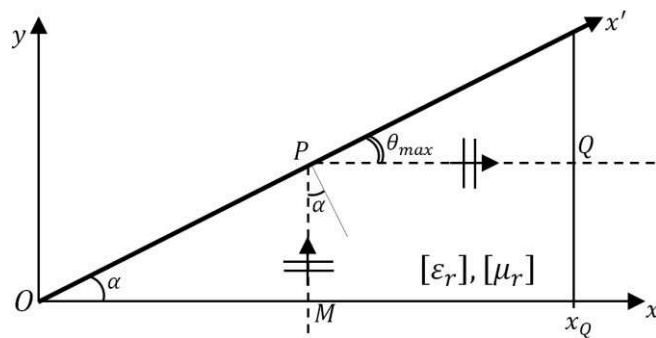


Figure 6. Configuration générale d'un panneau incliné (avec un angle d'inclinaison α) dans un milieu anisotrope.

Un gradient de phase généralisé est théoriquement calculé pour un panneau réfléchissant avec les conditions que $\theta_{max} = \alpha$ en présence d'un milieu anisotrope.

La possibilité d'effectuer un compromis entre le facteur d'anisotropie et le gradient de phase, lors de la conception d'un dièdre comprimé, est également démontrée. Cela offre un nouveau degré de liberté pour relâcher les contraintes sur le facteur d'anisotropie ρ du milieu étudié dans la partie 2 (pour une configuration OT pure $\rho = \frac{\epsilon_x}{\epsilon_y} = \frac{a^2}{b^2}$).

Différentes configurations d'impédance de surface sont vérifiées avec des simulations HFSS dans un premier temps.

Ensuite, un nouveau modèle physique OT/MIS est proposé. Les simulations ont confirmé le comportement rétro-directif attendu pour toutes les configurations étudiées. Elles ont également montré que l'introduction d'une petite dose de MIS peut servir pour réduire le facteur d'anisotropie requis par la configuration OT. En contrepartie, l'introduction d'un milieu anisotrope peut amplement améliorer les performances d'une configuration MIS pure mais au prix d'une réalisation plus complexe. La fig. 7. illustre les performances obtenues en SER mono-statique pour différents configurations d'aplatissement accordant une importance plus ou moins grande à la MIS.

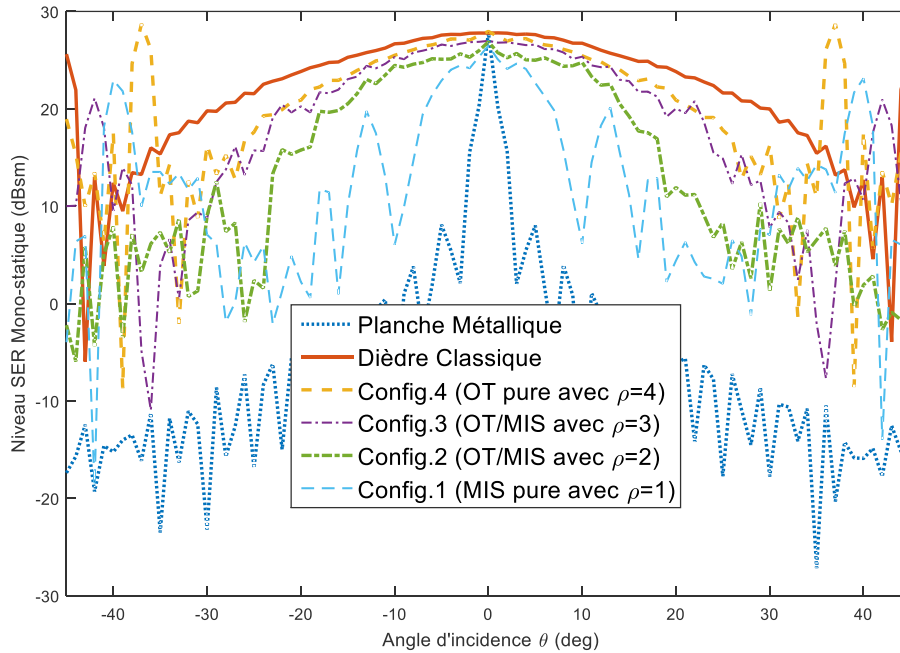


Figure 7. SER mono-statique pour différents configurations de réflecteurs diédriques comprimés (pour $a = 2b$) en comparaison avec le dièdre classique et une planche métallique (ayant une ouverture équivalente) selon l'angle d'incidence θ .

4. Atténuation des réflexions parasites sur les panneaux MIS

Une analyse des réflexions parasites pour les panneaux MIS semi-infinis est effectuée (cf. page 8). Les directions théoriques des harmoniques de Floquet sont déterminées pour les panneaux implémentant la MIS périodique (avec une période spatiale T_y) comme présenté par la fig. 8.

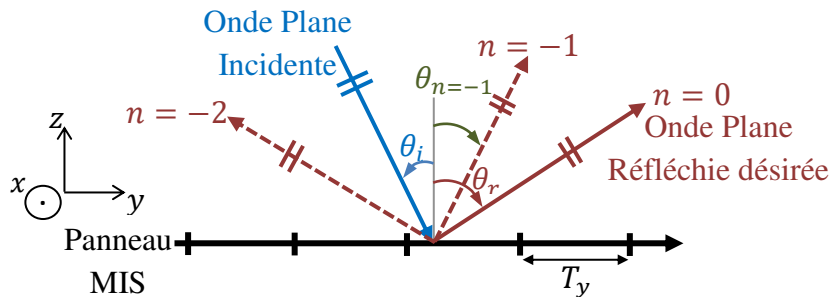


Figure 8. Trajectoires des ondes planes réfléchies d'un panneau MIS périodique.

Ces directions sont vérifiées avec des simulations électromagnétiques utilisant HFSS. Les lobes parasites rayonnés (θ_{-1} et θ_{-2}) en champ lointain confirment les directions obtenues dans l'analyse théorique comme démontré par la fig. 9.

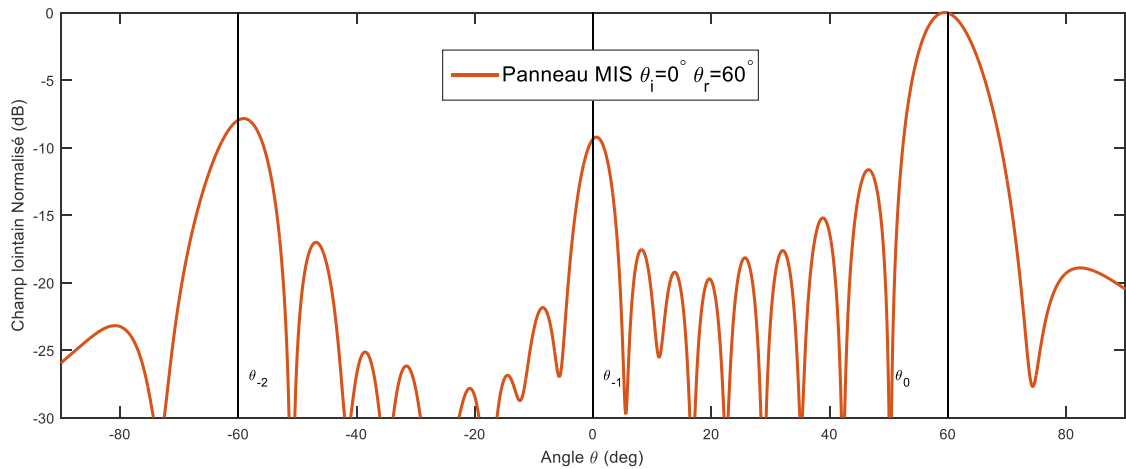


Figure 9. Champ rayonné normalisé (coupe du plan yz-champ E) pour une onde plane en incidence normale ($\theta_i = 0^\circ$) sur un panneau MIS ($\theta_r = 60^\circ$) ; Les lignes noires verticales sont les directions obtenues analytiquement pour les Harmoniques.

Une implémentation pratique, qui utilise des éléments imprimés sur un substrat diélectrique, est introduite par la suite pour les panneaux MIS [32]. Des simulations pour des panneaux pratiques semi-infinis (cf. exemple fig. 10) confirment également l'existence de lobes parasites rayonnés en plus du lobe principal désiré.

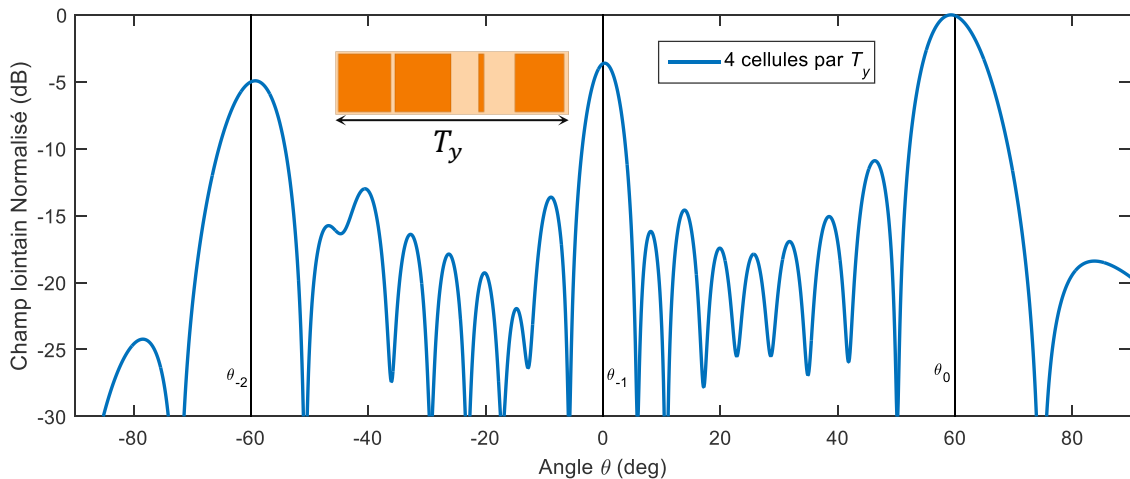


Figure 10. Champ rayonné normalisé (coupe du plan yz-champ E) pour une onde plane en incidence normale ($\theta_i = 0^\circ$) sur un panneau MIS pratique (utilisant des éléments imprimés).

Les différents résultats confirment également que de nouveaux degrés de liberté sont disponibles pour contrôler les lobes parasites. Les effets de la modification des dimensions des cellules unitaires, le nombre de cellules utilisées et l'état de phase sont discutés et reliés à la performance des panneaux.

La miniaturisation de l'élément imprimé d'une cellule montre aussi des résultats prometteurs pour l'atténuation des niveaux de lobes parasites.

De nouvelles métriques de réglage sont introduites pour obtenir des niveaux de lobes harmoniques parasites minimaux. Principalement, ceux-ci sont liés à la sensibilité de la phase d'une cellule unitaire S et au taux de résonance R de celle-ci. Par la suite, des critères spécifiques sont choisis afin d'atteindre les performances souhaitées du panneau et de minimiser les niveaux des lobes harmoniques (NLH) parasites comme présenté dans les résultats de différents panneaux pratiques (avec des paramètres de contrôle différents) dans la fig. 11. (zone définie par $R \leq 0,7$ et $|S| \leq 650 / \text{mm}$).

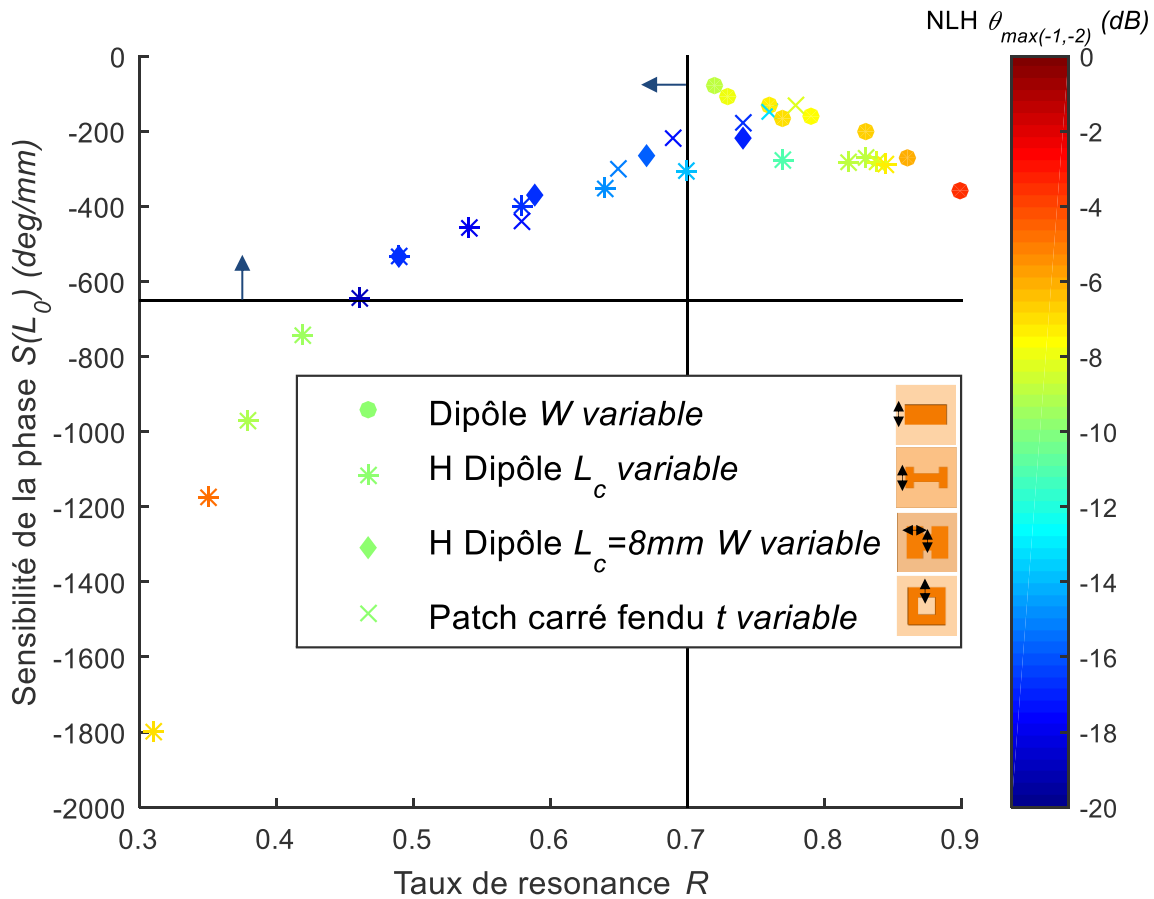


Figure 11. Niveaux maximums des lobes harmoniques parasites (NLH) en termes du taux de résonance et de sensibilité de la phase $S(L_0)$ pour différents panneaux ayant 3 cellules unitaires par T_y .

5. Modulation d'impédance de surface généralisée et son application pratique

Une nouvelle manière d'exploiter la MIS sur un panneau réfléchissant est proposée. Cela se fait en introduisant un coefficient de réflexion global Γ_G qui contrôle le niveau de d'énergie réfléchi.

En raison de la périodicité de l'impédance sur le panneau, les formulations classiques et généralisées entraînent l'excitation des harmoniques de Floquet d'ordre supérieur dans des directions indésirables. Des validations numériques sont effectuées avec des simulations HFSS démontrant l'efficacité de la technique. Des comparaisons avec une formulation SIM classique sont également présentées.

On observe que le coefficient de réflexion globale introduit un nouveau degré de liberté qui peut être utilisé pour diminuer les lobes parasites. À une valeur spécifique du coefficient de réflexion global ($|\Gamma_G| = 1$), la formulation généralisée présente des avantages en termes de diminution des niveaux de lobes parasites (cf. fig. 12).

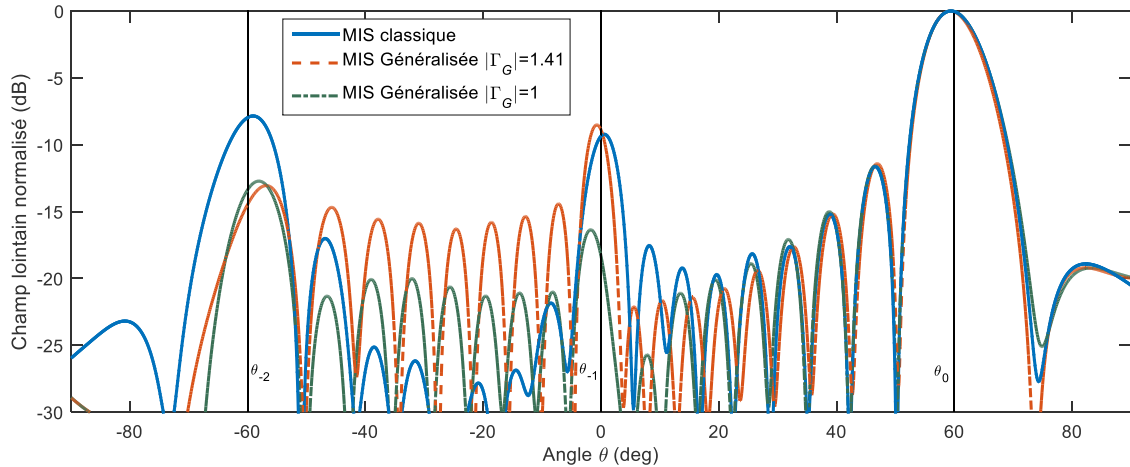


Figure 12. Champ rayonné normalisé (coupe du plan yz-champ E) pour un panneau MIS classique et deux autres panneaux MIS généralisée avec différents modules de coefficient de réflexion global (cas de conservation d'énergie $|\Gamma_G| = 1, 41$ et un autre avec $|\Gamma_G| = 1$).

Une application potentielle de la formulation généralisée avec un coefficient de réflexion global ajusté ($|\Gamma_G| = 1$) est présentée. On suggère d'utiliser des éléments à double couche pour contrôler à la fois l'amplitude et la phase de la distribution des coefficients de réflexion pour chacune des cellules conçues sur le panneau comme indiqué par la fig. 13.

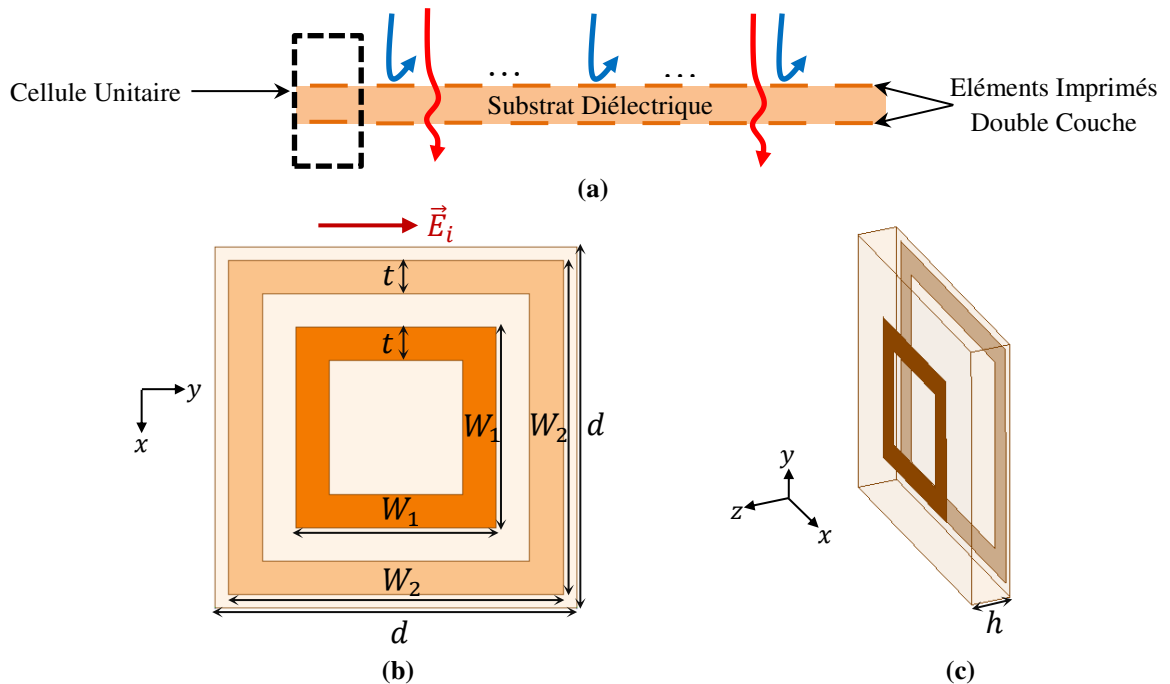


Figure 13. Illustration d'un panneau MIS généralisé pratique (vue en coupe); la puissance réfléchie est présentée par les flèches bleues, puissance transmise par les flèches rouges (a). Illustration de la cellule unitaire simulée utilisant des éléments de patch carré fendus sur les deux couches du substrat (ayant W_1 et W_2 comme paramètres de contrôle et $t = 2mm$ fixé). Vue de dessus (b) Vue 3D (c).

Cette méthode, clairement, élimine le besoin d'un plan de masse pour les panneaux réfléchissants pratiques. En même temps, elle permet d'atténuer les niveaux de lobes harmoniques parasites (NLH) comme présenté dans la fig. 14.

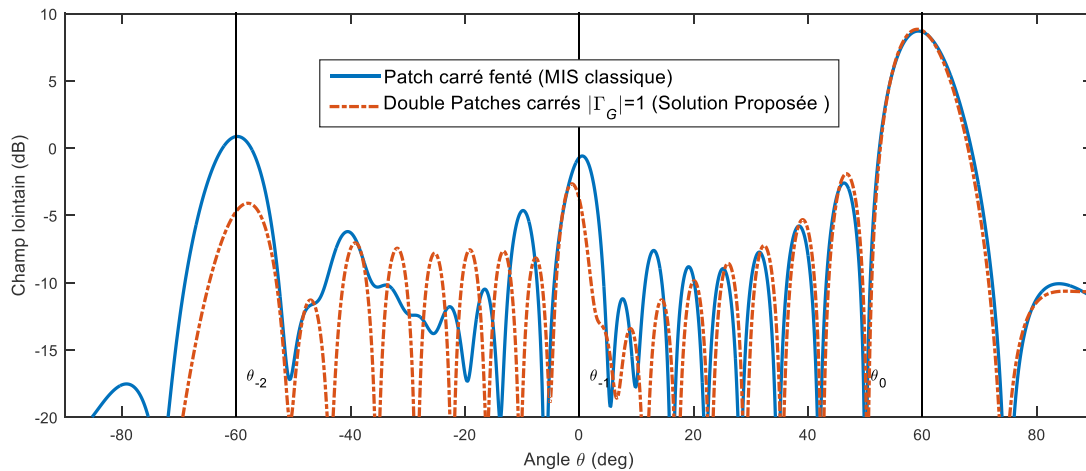


Figure 14. Champ rayonné (coupe du plan yz -champ E) pour un panneau patch carrés qui met en œuvre la distribution MIS classique et le panneau double patch qui met en œuvre la MIS généralisée avec $|\Gamma_G| = 1$.

6. Conclusion

Cette thèse introduit mise en œuvre simple de l'OT capable de comprimer le volume du réflecteur diédrique. On suggère de la réaliser grâce à un système diélectrique à double couche. Cependant, une telle fabrication nécessite un très grand nombre de couches diélectriques à épaisseur très fine ($\lambda_g/70$) ce qui la rend encore peu réaliste.

La combinaison entre OT (implémentée sur le volume) et MIS (sur la surface des panneaux) est capable d'atténuer les inconvénients des deux approches pour le réflecteur diédrique. Cette combinaison ouvre de nouvelles perspectives intéressantes vers différents dispositifs EM plus réalisables avec des performances améliorées.

Cette thèse a également permis de mieux comprendre la relation entre les niveaux de lobes harmoniques obtenus à partir des panneaux MIS périodiques. On a défini deux nouvelles métriques (la sensibilité de la phase et le taux de résonance) des éléments imprimés conçus. Les études conduites comprennent différents éléments passifs, y compris des dipôles imprimés, des dipôles en H et des patches à fente. Pour cette gamme d'éléments, ces métriques montrent qu'il est possible d'aboutir à des règles de conception assez simples et générales. Ainsi, en limitant la sensibilité des cellules utilisées et en éloignant leur état résonnant des bords de la maille, il semble possible de limiter l'apparition des réflexions parasites.

De plus, il est évident que toutes les recherches sur les panneaux MIS envisagent une onde plane incidente. Il est, toutefois, très intéressant de s'orienter vers des applications plus concrètes (par exemple, les réseaux réflecteurs). Dans ces structures, l'onde incidente sera produite par une source primaire à une distance bien définie du panneau réfléchissant.

Enfin, la méthode MIS généralisée avec un coefficient de réflexion globale ajusté ($|\Gamma_G| = 1$) présente des avantages par rapport à la MIS classique pour une configuration spécifique choisie (pour $\theta_i = 0^\circ$ et $\theta_r = 60^\circ$). Des analyses complémentaires pour certaines autres configurations (à incidence oblique par exemple) doivent être prises en compte pour confirmer l'intérêt de régler le coefficient de réflexion global introduit.

Table of Contents

List of Figures	17
List of Tables.....	23
List of Acronyms	25
Acknowledgement	27
General Introduction	29
Collaboration and Context	29
Outline	29
Chapter 1 - State of the Art.....	31
1. 1. Background on Retro-Directive Reflectors	31
1. 1. A. Overview on the Corner Reflector	32
1. 1. B. Radar Cross Section	33
1. 2. Background on Transformation Optics.....	35
1. 2. A. Coordinate Transformation	36
1. 2. B. Form Transformation of Maxwell's equations within TO	37
1. 2. C. Advances for flattened Dihedrals using TO media	38
1. 3. Background on Surface Impedance Modulated Panels	41
1. 3. A. Phase Shifting Unit Cell.....	42
1. 3. B. Advances in Flattened Dihedrals using SIM Panels.....	46
1. 4. The Image Lobe Concept.....	47
1. 5. Conclusion	48
Chapter 2 - Compression Technique for Retrodirective Reflectors Using Transformation Optics	49
2. 1. Background & Design of TO Compressed Reflectors.....	49
2. 1. A. Problem Statement	49
2. 1. B. Proposed Theoretical Design.....	50
2. 1. C. Analysis of TO Compressed Reflector at normal incidence	51
2. 1. D. Simulation Settings for TO Compressed Reflector	54
2. 1. E. Simulation Results of theoretical TO compressed reflectors	55
2. 2. Practical TO compressed reflector Designs	56
2. 2. A. 1st material simplification procedure	56
2. 2. B. 2nd material simplification procedure.....	56
2. 2. C. Simulation results of the practical TO compressed reflector design	57

2. 3.	Implementation of the Anisotropic Material	62
2. 3. A.	Double-layered System Design	62
2. 3. B.	Validation of the Double layered system using EMT.....	64
2. 3. C.	Simulation Results of the TO Compressed reflector using Double Layered system.	68
2. 4.	Conclusion.....	70

Chapter 3 – Combining Transformation Optics and Surface Impedance

Modulation for Retrodirective Reflectors..... 71

3. 1.	Theoretical Relations.....	72
3. 1. A.	Analytical Calculation of the Phase Gradient within Anisotropic Media for one inclined Panel	72
3. 1. B.	Parametric optimization between Anisotropic Factor and Phase Gradient	74
3. 2.	Implementing Surface Impedance Modulation (SIM)	76
3. 3.	Numerical Results	77
3. 3. A.	Validation of a Prescribed Surface Impedance.....	77
3. 3. B.	Verification of SIM array simulations with HFSS	79
3. 3. C.	Simulation Settings for a Compressed Reflector using a combination of TO and SIM	84
3. 3. D.	Simulation Results for the TO/SIM Compressed Reflectors.....	85
3. 3. E.	Radar Cross Section for the Compressed Reflectors	86
3. 4.	Conclusion.....	88

Chapter 4 - Mitigation of Parasitic Reflections over Surface Impedance

Modulated Panels 89

4. 1.	Reflection Analysis of SIM Panels	90
4. 1. A.	Extended phase gradient and Theoretical Plane Wave Directions	90
4. 1. B.	Verification of Floquet Harmonics using SIM Panels.....	92
4. 2.	Practical Implementation for SIM Panels	96
4. 3.	Mitigation of Parasitic Lobe Levels	100
4. 4.	Relation between Harmonic Lobe Levels, the Phase Sensitivity and Resonance of the unit cell.....	108
4. 4. A.	Proposed metrics.....	108
4. 4. B.	Simulation Settings.....	109
4. 4. C.	Simulation Results.....	109
4. 5.	Conclusion.....	112

Chapter 5 - Generalized Surface Impedance Modulation for Perfect Control of the reflected fields.....	113
5. 1. Theoretical analysis	114
5. 1. A. Variation of the surface impedance.....	114
5. 1. B. Power Conservation Model.....	115
5. 2. Numerical analysis.....	116
5. 2. A. Semi Infinite SIM Panel settings and Impedance Distributions.....	116
5. 2. B. SIM Simulation Results	118
5. 3. Practical Analysis	119
5. 3. A. Studied Configuration and Practical Panel Settings.....	119
5. 3. B. Reflection Response of the Unit Cell.....	121
5. 3. C. Radiated Field Simulations for Practical Panels	124
5. 4. Conclusion	126
General Conclusion.....	127
Perspectives	128
Publications.....	129
Bibliography	131

List of Figures

Figure 1. 1. Examples of Retro-Directive Reflectors.....	31
Figure 1. 2. Illustration (3D view) of a dihedral corner reflector (a) and trihedral corner reflector (b).....	32
Figure 1. 3. Illustration of a dihedral corner reflector (cross section view).....	32
Figure. 1. 4. Concept of Monostatic RCS in a specific direction θ for the dihedral corner reflector.....	33
Figure 1. 5. Light refraction phenomenon due to broken translation symmetry at the interface between air and water.....	35
Figure 1. 6. Virtual Grid (a) mapped into a physical grid (b). This transformation accomplishes a desired distortion of space along with the EM fields propagating in the physical domain.....	36
Figure. 1. 7. Dihedral corner reflector in the virtual space x, y (a). Proposed flat reflector in the transformed physical space x', y' (b). Black thick lines denote the PEC boundaries; red dashed lines delimit the free-space (a) and TO medium (b) regions involved in the transformation; grey thin arrowed lines indicate typical ray trajectories. The zoom in the inset highlights the negative refraction occurring in the transformation medium at the $y' = 0$ interface [14].....	38
Figure. 1. 8. Dihedral corner reflector in ABC along with the Proposed flat reflector with the TO (physical) domain denoted by AB'C. Black thick lines denote the PEC boundaries; dashed lines delimit the TO medium; a and b being the dimensions of the TO medium for a planar reflector of aperture AC with a length equal to 2a; red arrowed lines indicate typical ray trajectories in the classical dihedral [15]......	39
Figure. 1. 9. Near electric field distributions (time domain) of the proposed non-magnetic retrodirective reflector (dimensions $a = b$) for incident wave at incidence angle $\varphi = 90^\circ$ (a), $\varphi = 120^\circ$ (b), and $\varphi = 135^\circ$ (c). The thick black line indicates the planar PEC sheet and the incidence angle φ here is θ in our conventions. Normalized far-field scattering patterns (d). 40	40
Figure. 1. 10. SIM panel (along y -axis) redirects an incident plane wave that impinges with an angle θ_i into to a reflection angle $\theta_r \neq \theta_i$. This is done by introducing phase discontinuities along the panel.....	41
Figure 1. 11. Practical SIM panel geometry (cross section view) showing the incident and reflected plane waves; d being the unit cell's dimension.....	42
Figure 1. 12. Phase shifting unit cell with the conventions used for incidence and reflection.....	43
Figure 1. 13. Illustration of a Printed Dipole element unit cell as part of an infinite periodic structure (Phase De-embedding is represented by the dashed red line brought to the surface of the printed element)	44
Figure 1. 14. Reflection Phase Response versus element length for a simulated infinite array of identical dipoles using HFSS for $W = 2mm$, $f = 8GHz$, $\theta_i = 0^\circ$, unit cell dimension $d = 0.388\lambda$ with the substrate used "Cuclad 5880" with $h = 1.6mm$	45
Figure. 1. 15. Concept of a flattened dihedral reflector; α being the inclination angle (with $\alpha = 45^\circ$ for the conventional reflector), d the inter element spacing and γ the phase shift between two adjacent patches [14]......	46

Figure. 1. 16. RCS comparison between a flate plate, a conventional dihedral and the proposed flattened dihedral of the same aperture for TE polarization in [14].	46
Figure 1. 17. Practical SIM panel geometry (cross section view) showing the incident plane wave and the direction of the “image lobe”.	47
Figure. 2. 1. The original 2D space of a corner reflector with its proposed transformation.	50
Figure. 2. 2. Wave Propagation within the TO compressed Reflector.	51
Figure. 2. 3. Wave Propagation within the TO compressed Reflector.	53
Figure. 2. 4. Simulation Configuration for the Compressed Reflector using TO for $a = 2b$.	55
Figure. 2. 5. Total complex Electric field amplitudes (V/m) at normal incidence for Classical Reflector (a), Compressed Reflector using TO for $a = 2b$ ($\epsilon'x = \mu'x = 2, \epsilon'y = \mu'y = 0.5, \epsilon'z = \mu'z = 2$) (b), for $a = 4b$ ($\epsilon'x = \mu'x = 4, \epsilon'y = \mu'y = 0.25, \epsilon'z = \mu'z = 4$) (c).	56
Figure. 2. 6. Total complex E-field amplitudes (V/m) with Reduced μ' of the TO domain for $a = 2b$ ($\epsilon'x = \epsilon'z = 4, \epsilon'y = 1$) (a) and $a = 4b$ ($\epsilon'x = \epsilon'z = 16, \epsilon'y = 1$) (b).	58
Figure. 2. 7. Total complex E-field amplitudes (V/m) with $a=2b$ dimensions using (2-24) for $\epsilon'x = \epsilon'z = 1; \epsilon'y = 0.25$ (a) $\epsilon'x = \epsilon'z = 8; \epsilon'y = 2$ (b), $\epsilon'x = \epsilon'z = 12; \epsilon'y = 3$ (c) and $\epsilon'x = \epsilon'z = 16; \epsilon'y = 4$ (d).	59
Figure. 2. 8. Illustration of a TO compressed reflector with an impedance matching layer.	60
Figure. 2. 9. Total complex E-field amplitudes (V/m) with $a=2b$ dimensions using (2-24) for $\epsilon'x = \epsilon'z = 8; \epsilon'y = 2; \epsilon a = 2.82$ (a), $\epsilon'x = \epsilon'z = 12; \epsilon'y = 3; \epsilon a = 3.46$ (b) and $\epsilon'x = \epsilon'z = 16; \epsilon'y = 4; \epsilon a = 4$ (c).	61
Figure. 2. 10. Representation of the dielectric layers distribution using EMT.	62
Figure. 2. 11. ϵ_1 (a) ϵ_2 (b) relative permittivity values in terms of thickness ratio d for different effective distributions $\epsilon'x$ and $\epsilon'y$ used within the compressed reflector ($a = 2b$).	63
Figure. 2. 12. Comparative analytical study between homogeneous layer with $\epsilon x = 4$ (a) and double layered system with alternating $\epsilon_1 = 7.464$ & $\epsilon_2 = 0.5359$ (b).	64
Figure. 2. 13. Error Rates (%) of the magnitude and phase components for the reflection coefficient in terms of the number of layers per guided wavelength.	65
Figure. 2. 14. Illustration of the simulated configuration for the validation of the y permittivity tensor component.	67
Figure. 2. 15. Close up at Electric Field Distributions in Time Domain (V/m) within a double layered system with E-field vectors perpendicular to the layers for $2\text{layers}/\lambda gx$ (a) $4\text{ layers}/\lambda gx$ (b) $6\text{ layers}/\lambda gx$ (c) $8\text{ layers}/\lambda gx$ (d) $10\text{ layers}/\lambda gx$ (e).	67
Figure. 2. 16. Convergence of the y -component of the permittivity obtained from the double layered system versus the number of layers.	68
Figure. 2. 17. Total complex E-field amplitudes (V/m) for double-layered system with $\epsilon_1 = 7.464$ and $\epsilon_2 = 0.5359$ for (a) $10\text{ layers}/\lambda gx$ (total of 100 layers parallel to the x-axis) (b) $25\text{ layers}/\lambda gx$ (c) $50\text{ layers}/\lambda gx$.	69
Figure 3. 1. General configuration with one inclined panel in an anisotropic medium.	72
Figure 3. 2. Phase gradient versus the anisotropic factor for compressed reflector with different inclination angles α .	75

Figure 3. 3. General configuration of a compressed reflector with a combination of discretized SIM over the panels and TO domain filling the reflector's domain.....	76
Figure 3. 4. HFSS simulation of a prescribed surface impedance (Z_s) sheet positioned at the middle of a TEM waveguide.	78
Figure 3. 5. Magnitude (a) and phase (b) of the reflection coefficient as function of the reactance X_s	78
Figure 3. 6. HFSS configuration of prescribed Z_s at the boundary of a TEM waveguide (config. a.) and at the interface of a volumetric PEC positioned within the TEM waveguide (config. b.).	79
Figure 3. 7. Magnitude (a) and phase (b) components of the reflection coefficient for the different simulated configs in function of X_s	79
Figure 3. 8. Illustration of the chosen conventions for one SIM panel.	80
Figure 3. 9. Simulated configuration (xz plane visibility cut) for a normally incident plane wave over an array of planar sheets with prescribed impedances.	80
Figure 3. 10. Prescribed surface impedances used on each planar sheet of the simulated SIM panel for different normal incidence configurations ($\alpha = 0^\circ$).	81
Figure 3. 11. Comparison between the normalized array factor of a phased linear array and the simulated normalized directivity of the SIM panel with prescribed impedance for $\theta_{max} = 80^\circ$ (a), $\theta_{max} = 70^\circ$ (b) and $\theta_{max} = 60^\circ$ (c).	82
Figure 3. 12. Prescribed surface impedances for each planar sheet at oblique incidence configurations.	83
Figure 3. 13. Comparison between normalized array factor of a phased linear array with the simulated directivity of planar sheets for $\alpha = 10^\circ$ and $\theta_{max} = 70^\circ$ (a), $\alpha = 20^\circ$ and $\theta_{max} = 50^\circ$ (b) and $\alpha = \theta_{max} = 26.56^\circ$ (c).	83
Figure 3. 14. Theoretical anisotropic medium (highlighted in green) filling the Compressed Reflector's domain (Volumetric PEC highlighted in orange).	84
Figure 3. 15. Nearfield maps (time domain) for compact retro-directive reflector using (a) config. 1, (b) config. 2, (c) config. 3, (d) config. (4).	85
Figure 3. 16. Normalized Directivity (E-plane xy cut) for different configurations using a normally incident Gaussian beam.....	85
Figure 3. 17. Monostatic RCS response for different reflectors versus incidence angle θ	86
Figure 4. 1. General configuration used for the reflective SIM Panel.....	90
Figure 4. 2. Trajectories of plane waves reflected from a periodic SIM Panel.	91
Figure 4. 3. Simulated configuration for an incident plane wave over a semi-infinite SIM panel.	93
Figure 4. 4. Periodic Surface Reactance Distributions for different reflecting SIM panels.	94
Figure 4. 5. Normalized Radiated field cut (along yz plane) from a normally incident plane wave over config. 1 (table 4. 1.).	95
Figure 4. 6. Normalized Radiated field cut (along yz plane) from a normally incident plane wave over config. 2.	95
Figure 4. 7. Normalized Radiated field cut (along yz plane) from an oblique incident plane wave over config. 3.	95
Figure 4. 8. Illustration of a Practical SIM Panel.	96

Figure 4. 9. Illustration of the simulated unit cell (3D view) with a dipole element. Incident E-field along $+y$	97
Figure 4. 10. Reflection Phase Response for a unit cell versus the dipole's length in Floquet's simulation.....	97
Figure 4. 11. Complete Spatial periods Ty (Top View) for four different Dipole widths $W = 4mm$ (a) $W = 6mm$ (b) $W = 8mm$ (c) $W = 10mm$ (d).....	98
Figure 4. 12. Simulated semi-infinite panel using printed dipoles as unit cell elements.....	98
Figure 4. 13. Normalized Radiated field cut (along yz plane) from a normally incident plane wave over the corresponding practical panel with 4 unit cells per Ty and $Lt = 9Ty$. Black vertical lines represent the directions calculated from eq. (4-5) with $\theta_0 = \theta_r = 60^\circ$; $\theta_{-1} = 0^\circ$ and $\theta_{-2} = -60^\circ$	99
Figure 4. 14. Reflection Phase Response for a unit cell versus the dipole's length in Floquet's simulation.....	100
Figure 4. 15. Normalized Radiated field cut (along yz plane) using a panel containing 3 unit cells per Ty and $Lt = 9Ty$	101
Figure 4. 16. Normalized Radiated field cut (along yz plane) using panels with dipole widths $W=10mm$ for 3 and 4 unit cells per Ty (their top view included).....	102
Figure 4. 17. Choosing two different offset from the reflection phase response of a unit cell with a dipole element.	103
Figure 4. 18. Geometrical variation for complete periods Ty (Top View) of a panel configuration with dipoles widths at $W = 2mm$ and phase offsets $\phi\Gamma_1 = 28^\circ$ (a) $\phi'\Gamma_1 = 53^\circ$ (b).....	103
Figure 4. 19. Normalized Radiated field cut (along yz plane) for different dipoles widths at W and phase offsets (a) with a close up at the specular reflection θ_{-1} (b).....	104
Figure 4. 20. Illustration of the simulated unit cell (Top View) with an H dipole element. Incident E-field along $+y$	105
Figure 4. 21. Reflection phase response for a unit cell versus the miniaturized H dipole's length L for different fixed arms length Lc in Floquet's simulation.....	106
Figure 4. 22. Normalized Radiated field cut (along yz plane) using a panel containing 3 unit cells per Ty and $Lt = 9Ty$ (a) with a close up at the reflection $\theta - 2$ (b) and specular reflection θ_{-1} (c).	107
Figure 4. 23. Illustration of the simulated unit cell (Top View) using slotted square patch element. Incident E-field along $+y$	109
Figure 4. 24. Maximum Harmonic Lobe Levels (HLL) in terms of the unit cell's resonance ratio R and their phase sensitivity $S(L0)$ for panels using 3 unit cells per Ty with $Lt = 9Ty$	110
Figure 4. 25. Maximum Harmonic Lobe Levels (HLL) in terms of the unit cell's resonance ratio R and their phase sensitivity $S(L0)$ for panels using 4 unit cells per Ty with $Lt = 9Ty$	110
Figure 5. 1. General configuration of a SIM panel within free space.....	114
Figure 5. 2. Incident and Reflected waves for power conservation model.....	115

Figure 5. 3. Values of the real (a) and imaginary (b) parts of Z_{si} over the panel for $\{\theta_i = 0^\circ; \theta_r = 60^\circ\}$.	117
Figure 5. 4. Normalized Radiated far field, E-plane cut (along yz), for the classical SIM distribution and Generalized SIM distributions with two different Γ_G . The vertical black lines represent the analytical directions for each harmonic lobe.	118
Figure 5. 5. Magnitude (a) and phase (b) local reflection coefficient distributions needed over the practical panel.	120
Figure 5. 6. Illustration of a Practical Generalized SIM Panel (Cross Section View). (The reflected power is presented in blue arrows; Transmitted power in red arrows).	121
Figure 5. 7. Illustration of the simulated unit cell Top View (a) 3D view (b) using slotted square patch elements; Incident E-field along $+y$.	121
Figure 5. 8. Magnitude (a) and phase (b) reflection response obtained for the unit cell in infinite periodic environment.	122
Figure 5. 9. Spatial period T_y (Top View) for the double squared patch panel.	123
Figure 5. 10. Normalized radiated field E-plane cut (along yz plane) for Generalized SIM panel with $\Gamma_G = 1$ (from fig. 5. 4.) and Double Square Patch Panel implementing the same solution (from table 5. 1.).	124
Figure 5. 11. Illustrations (Cross Section Views) of a grounded square patch panel implementing classical SIM (a) and double square patches panel implementing Generalized SIM with $\Gamma_G = 1$ (b).	124
Figure 5. 12. Radiated field E-plane cut (along yz plane) for Grounded Square Patch Panel implementing Classical SIM distribution and Double Square Patch Panel implementing Generalized SIM with $\Gamma_G = 1$.	125

List of Tables

Table 2. 1. Comparison of Reflection Losses for different Retrodirective Reflectors.....	58
Table 2. 2. Comparison of Reflection Losses for different tensor components.	60
Table 2. 3. Comparison of Reflection Losses for compressed reflectors with matching layers.	61
Table 2. 4. Comparison of Reflection Losses for different layer densities.	69
Table 3. 1. Parameters used for simulated Configurations.....	84
Table 3. 2. Main performance for the different reflectors.	87
Table. 4. 1. Parameters used for the simulated semi-infinite Configurations.	93
Table 5. 1. Unit Cell Parameters used for the simulated Configuration of a panel with Generalized SIM distribution with $ \Gamma_G = 1$	123

List of Acronyms

TO	Transformation Optics
EM	Electromagnetic
2D	Two Dimensional
3D	Three Dimensional
PEC	Perfect Electric Conductor
PMC	Perfect Magnetic Conductor
TE	Transverse Electric
TM	Transverse Magnetic
EMT	Effective Medium Theory
SIM	Surface Impedance Modulation
RCS	Radar Cross Section
HPBW	Half-Power Beam Width
HLL	Harmonic Lobe Levels

Acknowledgement

As is often the case of overseas students, I have found the experience during my thesis fascinating but full of challenges at the same time. Today when I finish this thesis and retrospect, I find that all the challenges came together with rewards. During these three years, I appreciate and honor all the people that have participated in my life and offered help generously. I would like to spend my ink on the words of gratitude for them all.

I would like to begin with thanking my thesis supervisors, Prof. Renaud LOISON, Prof. Raphael GILLARD, Prof. Akil JRAD and last but not least Dr. Ali HARMOUCH, all of whom welcomed me into their respective research teams in IETR, INSA-Rennes and in EDST-UL.

The subject of the thesis they offered was brand new and very interesting to me.

They showed me nothing but patience and motivation especially at the lows of my research work. I deeply appreciate every piece of advice and guidance they have once given me.

In addition, I need to also express my gratitude for the opportunities to get to meet and collaborate with many great colleagues at the IETR, they were actually more like a second family than research buddies.

Moreover, I also want to thank my all-time best friends, Mohamad Laurent YASSIN, Nadine KHODOR, Hassan ISMAIL, Samara Gharbieh and Sahar YASSINE for all the support and love they have given me throughout this experience. Much love and respect to each and every one of them.

Next, I would like to sincerely thank my parents Samira and Mohamad Saffouh who have encouraged me at each step of the way. They have given me every ounce of love, supported me unconditionally and asked nothing in return but to become a better man first and researcher second.

Last, I would like to express my gratitude to Philippe AYMARD and Jean David BIGONI who put their trust in me, be there at my defense and support me to carry on with what was started at IETR of INSA Rennes.

General Introduction

Collaboration and Context

This thesis was carried out as a first collaboration between the Institute of Electronics and Telecommunications of Rennes (IETR), on the campus of the National Institute of Applied Sciences of Rennes (INSA-Rennes) and the Laboratory of Electronic Systems, Telecom and Networks (LaSTRe) from the Lebanese University. From the French part, it was supervised by Renaud Loison and co-supervised by Raphaël Gillard, both professors at INSA-Rennes. On the other hand, from the Lebanese part, it was supervised also by Akil Jrad, professor, and co-supervised by Ali Harmouch, lecturer, both at the Lebanese University.

It is a continuation of researches conducted on retrodirective reflectors, carried out within the IETR lab since 2012. In the context of this thesis, the dihedral reflector seems a simple and effective way to obtain retrodirectivity in the microwave domain. It is used for many radar and antenna applications but its bulkiness prevents it from being integrated in such applications. So, our contributions in this thesis include the exploration of different research domains that might lead to lower profiles of this reflector. At first, it explores the use of Transformation Optics that modifies the filling volume and Surface Impedance Modulation that introduces an impedance distribution over the surface panels of such a device. It also inspects the possibility of combining those two domains to compromise the disadvantages of each. The second part of this thesis investigates the source of parasitic lobes for surface impedance modulated panels and proposes new directions to mitigate their levels. Finally, it also proposes a practical implementation for a specific setting of the generalized surface impedance modulation. Such modulation makes use of complex impedances that is able to outperform a panel implementing the classical one (with pure imaginary impedances).

Outline

This thesis is structured in five chapters:

The first is a general presentation of the principles of the retrodirective reflector and the main challenges associated with it. State of the art for transformation optics and surface impedance modulation is also detailed along with their recent advances that marked the development of low profile reflectors.

In the second chapter, we apply a more practical TO approach to the dihedral reflector than what is used in literature. It consists of a compression technique for the conventional reflector as a viable alternative to being oriented towards a planar one. Such technique leads to anisotropic homogeneous medium with uniaxial constituting parameters. Then, the feasibility of practical implementation is discussed for the proposed medium. A multilayered dielectric stack-up is suggested and the proof of concept is given with simulations.

In the third chapter, we combine the conceived TO medium to Surface Impedance Modulated panels. Such a combination offers compromise between the inconvenients of both approaches. On one end, it relaxes the constraints that lead to the realization of the TO medium and on the

other it improves the performance of surface impedance modulation applied over the reflector's panels.

The fourth chapter first identifies anomalies over Surface Impedance Modulated panels that can be associated with harmonic reflections. Geometric parameters contributing to this parasitic effect are identified and design rules are derived to improve the design. It proposes formalization for the effect of phase sensitivity and a newly introduced parameter called the resonance ratio. When combined together, those parameters affect the reflection performance of the panels and offers possibilities to obtain low harmonic lobe levels.

In the last chapter, generalized surface impedance modulation that takes advantage of both its real and imaginary components is introduced. A new single parameter that identifies power conservation between incidence and reflection is then presented as a degree of freedom. For a given configuration, a practical implementation using double layered unit cells is introduced as a potential solution to mitigate the levels of higher order harmonic reflections.

Finally, we conclude with a global synthesis of the conducted work, emphasizing on the advances and considering the perspectives that might add merit to these studies.

Chapter 1 - State of the Art

In this chapter, the retrodirective reflector is first briefly introduced. The interest of using such a device for the microwave domain is discussed. The interest of lowering the profile of a dihedral corner reflector is presented. One of the methodologies that made this possible is Transformation Optics which acts over the filling volume of the reflector. On the other hand, Surface Impedance modulation (SIM) over the surface of the reflector's panels is presented as another viable methodology. Its practical employment using physical cells is also considered. A fairly unidentified inconvenience for such applications is their parasitic reflections that can greatly affect their overall performance. The source that might cause these reflections from theoretical or even practical SIM panels is then discussed along with possible ways to mitigate their levels.

1. 1. Background on Retro-Directive Reflectors

Retro-Directive reflectors are structures able to reflect an incident EM wave back towards the source, i.e. in the same direction as that of incidence. Many examples of these reflectors can be found in nature, especially in the optical domain. Man-made reflectors have also been developed at both optical and RF frequencies. Some examples are shown in fig. 1. 1.

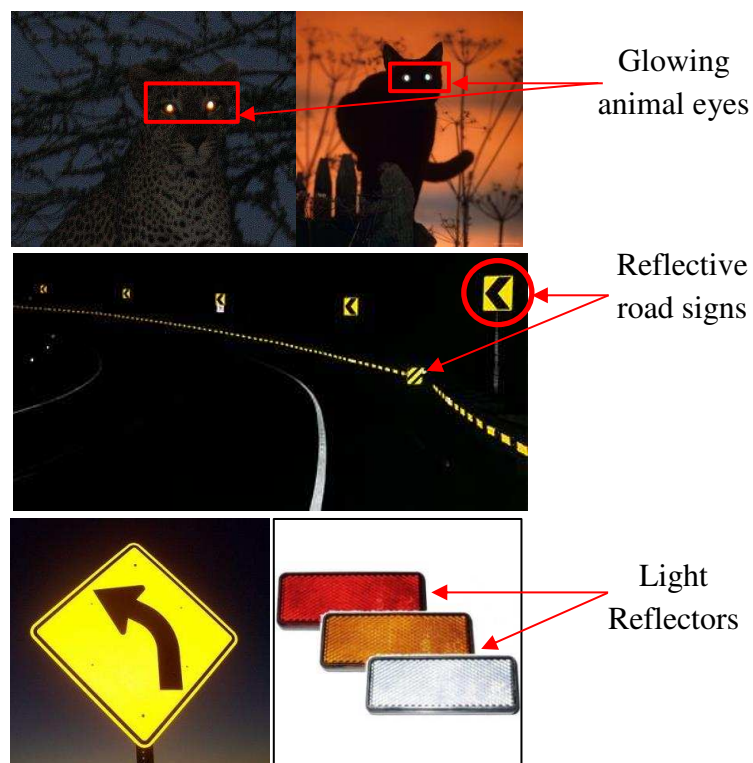


Figure 1. 1. Examples of Retro-Directive Reflectors.

The glowing eyes of animals are a typical example of a natural retro-directive structure. It relies on a specific form of the eye lens arrangement with several associated layers. Reflective road signs and light reflectors (for vehicles) have been designed to mimic the reflective properties of the cat's eye.

Alternatively, in the microwave domain, retro-directive reflectors are used for radar and antenna applications. The fact that it reflects back the incoming signal makes it ideal for radar identification purposes. At RF frequencies, the simplest retro-directive reflector is the corner reflector. It is commonly used to improve the radar detection of small vehicles [1] (sailing boats for instance) or in radar calibration [2]. The corner reflector is presented next.

1. 1. A. Overview on the Corner Reflector

This structure consists of two (dihedral) or three (trihedral) mutually orthogonal flat metallic panels as illustrated in Fig. 1. 2.

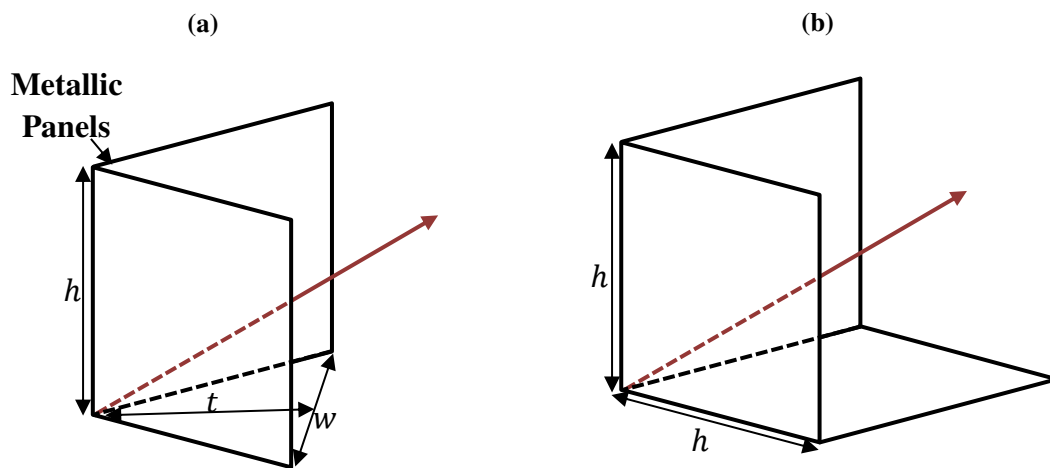


Figure 1. 2. Illustration (3D view) of a dihedral corner reflector (a) and trihedral corner reflector (b).

h and w represent the dimensions of the corner reflector and t being its depth. For simplicity, we only discuss here the dihedral corner reflector. Fig. 1. 3. presents in details the operating principal of a dihedral corner reflector.

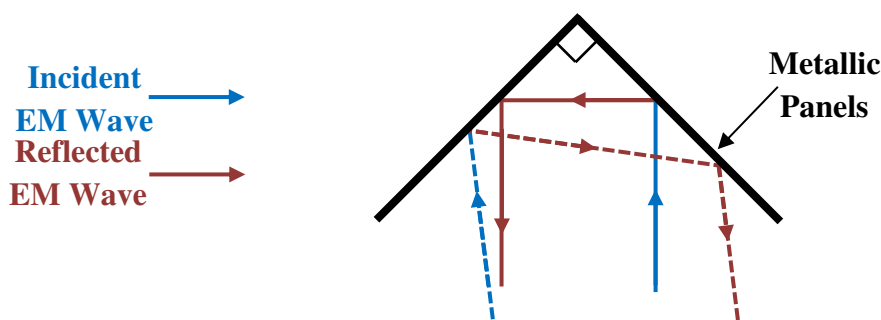


Figure 1. 3. Illustration of a dihedral corner reflector (cross section view).

From fig. 1. 3., it is clear that EM waves impinging on one panel are reflected onto the second and exit the structure back in the direction of incidence (for normal or oblique incidence alike).

The range of operation is actually limited by their size, especially when the application needed is in the microwave domain. For proper operation, the typical dimensions of the retro-directive reflector must be much larger than the operating wavelength. Indeed, the size

directly controls the Radar Cross Section (RCS), to be introduced in more details in the next sub-section.

1. 1. B. Radar Cross Section

The RCS of an object is a way of quantifying its response to a radar system. When exposed to an EM wave, an object scatters the incident energy in all directions. The RCS is defined as the effective area of the object that would reradiate the intercepted field isotropically into all directions. This area would produce the same power density at the receiver as the original target [3]. The RCS is a function of both the direction and polarization of the incident wave as well as the location of the observation point. The definition for the RCS σ [3] for a monostatic configuration (i.e. incident and reflected angles are identical) is as follows in eq. (1-1):

$$\sigma(\theta) = \lim_{r \rightarrow \infty} 4\pi r^2 \left| \frac{E_r}{E_i} \right|^2 \quad (1-1)$$

where $|E_i|$ and $|E_r|$ are the magnitude of the incident and reflected electric fields while r is the distance between the source and the target as shown in fig. 1. 4.

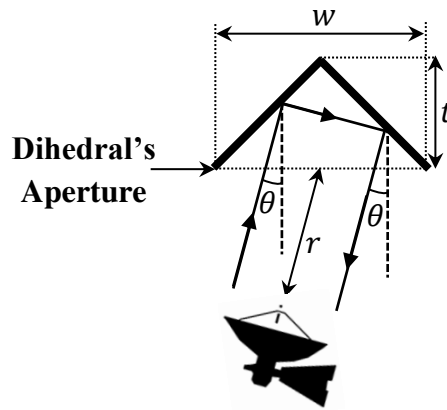


Figure 1. 4. Concept of Monostatic RCS in a specific direction θ for the dihedral corner reflector.

Maximizing the RCS for a given target allows for greater ease in its distinction and identification by a radar system. It is also well known that a corner reflector is one of the best targets that yield maximized monostatic RCS. When the field is normally incident upon the reflector's aperture, RCS of the dihedral is equivalent to a planar sheet having the same effective area as its aperture. It can be obtained from geometrical optics as follows:

$$\sigma(\theta = 0^\circ) = \frac{4\pi h^2 w^2}{\lambda^2} \quad (1-2)$$

Actually, the RCS is directly proportional to the aperture's dimensions as shown in eq. (1-2). The trade-off here is that with bigger dimensions for its aperture, the dihedral becomes much more bulky since its depth t is related to the aperture's width w (orthogonality between the panels should be conserved).

So, one of the challenges given for the dihedrals is to achieve lower profile and greater compactness (smaller depth t) while preserving their RCS performance. Two different

methodologies were used in literature to enhance the characteristics of passive dihedral reflectors which act on their dimensions. One acts over the filling volume of the reflector using the Transformation optics (TO) technique. The other acts over the surface of the reflector's panels using surface impedance modulation (SIM) which gives the ability to flatten the dihedral.

1. 2. Background on Transformation Optics

The geometry of wave propagation is not as linear as popularly thought before. It is well known that free space provides a flat geometry for waves to propagate in a straight line and at constant velocity. But, if we look at a pen in a cup of water it seems bent, due to some light refraction phenomena at the interface between air and water as shown in figure 1 .5.

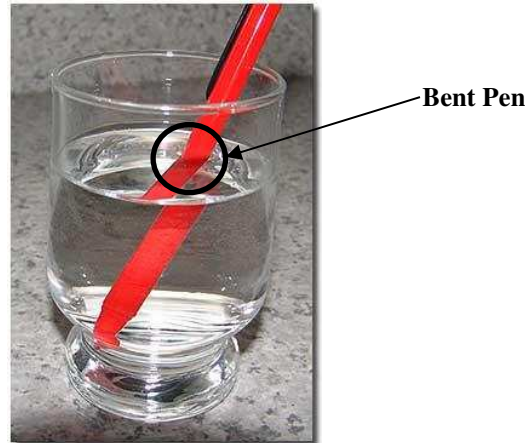


Figure 1. 5. Light refraction phenomenon due to broken translation symmetry at the interface between air and water.

As another example, objects seen through fire seem distorted. The temperature gradient from the fire makes the refractive index of air inhomogeneous, which creates a curved space and consequently geometries seem distorted. With these natural occurring phenomena in mind, Transformation Optics (TO) was first proposed in [4, 5] to formulate different methodologies that enable the manipulation of light or electromagnetic (EM) waves [6].

The key new ingredient in the EM design methodology is the fact that under a coordinate transformation, the field lines may be rearranged. More precisely, they behave as though they were fixed to the coordinate system. The distortion of the coordinates is obtained by modifying the properties of the propagation medium. The geometric interpretation of Maxwell's equations, utilized in the TO approach, provides a powerful and intuitive design tool for the manipulation of EM fields on all length scales [7]. These manipulations can be applied to design specific devices that aim at transforming an incident wave. The first attempted device was the famous invisibility cloak [4, 5]. Then came many different methodologies for controlling EM waves in different other ways and for a wide range of applications. Using these ideas, numerous novel devices have been designed, such as a cylindrical magnifying lens [8], flat focusing lens [9], carpet cloaks [10], planar reflectors [11], wave collimators, shifters and splitters [12], etc.

It is important to note that one of the ways to practically realize transformation optics media [19, 20] considers "Metamaterials". They are materials that are structured at a subwavelength scale to exhibit desired parameters. Achievable material parameters include those not found in nature [16-18]. Metamaterials are typically designed by presenting small inclusions in a three-

dimensional domain such that the resulting effective medium possesses desired bulk properties which is ideal in most cases for the realization of TO.

In order to provide the reader with the background information necessary to understand the second chapter of this manuscript, this section gives a brief introduction to the general TO methodology.

1. 2. A. Coordinate Transformation

First, a coordinate transformation is performed for a needed application. It introduces a desired conceptual distortion of space. In this process, a virtual space is mapped into a physical domain. The EM fields in the physical domain can be described as if propagating in the virtual space. Coordinate transformation is not limited to simple Cartesian, cylindrical, and spherical grids, but can also be distorted into any complex system, such as the one depicted in fig. 1. 6.

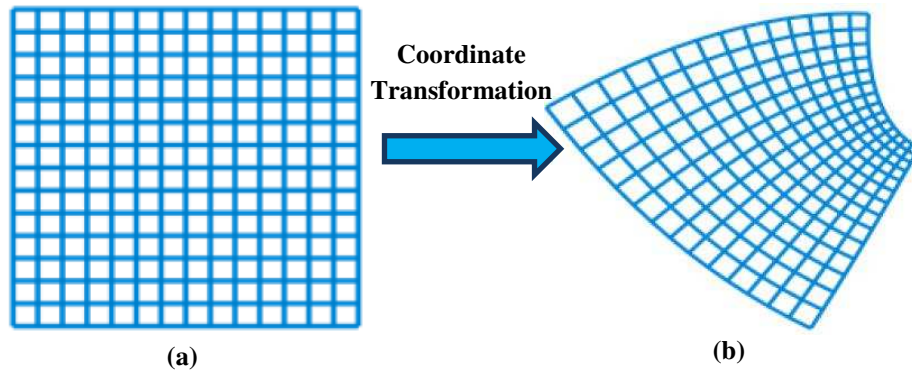


Figure 1. 6. Virtual Grid (a) mapped into a physical grid (b). This transformation accomplishes a desired distortion of space along with the EM fields propagating in the physical domain.

Starting with an arbitrary 3D coordinate transformation, we consider the following general case as in eq. (1-3):

$$\begin{cases} x'_1 = x'_1(x_1, x_2, x_3) \\ x'_2 = x'_2(x_1, x_2, x_3) \\ x'_3 = x'_3(x_1, x_2, x_3) \end{cases} \quad (1-3)$$

where x_i represents the virtual system's coordinate (x_1, x_2, x_3) and x'_i the resulting transformed coordinate (x'_1, x'_2, x'_3) from eq. (1-3).

The Jacobian matrix $[A]$ relates differential elements between the virtual and the physical space so each element is written according to the following eq. (1-4):

$$A_i^{i'} = \frac{\partial x'_i}{\partial x_i} \quad (1-4)$$

The vector field components are related to $[A]$ and written in their components notation, as follows in eq. (1-5):

$$\begin{cases} E_i = A_i^{i'} E_{i'} \\ H_i = A_i^{i'} H_{i'} \end{cases} \quad (1-5)$$

1. 2. B. Form Transformation of Maxwell's equations within TO

TO relies on what is termed the “form-invariance” of Maxwell's equations, which means that it provides a method to modify the EM fields by changing the constitutive parameters of the space.

Maxwell's equations can be rewritten in their transformed frame by applying eqs. (1-4) and (1-5). Through the use of various identities (space precludes the full derivation), it is possible to summarize the transformed Maxwell's equations as in Table 1. 1.

Table 1. 1. Summary of the transformation rules and Maxwell's transformed equations in their component form [7].

Transformation Rules	Transformed Maxwell's Equations
$\varepsilon_{i'j'} = \frac{A_i^{i'} A_j^{j'}}{ A } \varepsilon_{ij}$	$\varepsilon^{i'j'k'} \partial_{j'} H_{k'} = \varepsilon_{i'j'} \frac{\partial E_{j'}}{\partial t} + J_i'$
$\mu_{i'j'} = \frac{A_i^{i'} A_j^{j'}}{ A } \mu_{ij}$	$\varepsilon^{i'j'k'} \partial_{j'} E_{k'} = \mu_{i'j'} \frac{\partial H_{j'}}{\partial t}$
$J_i' = \frac{A_i^{i'}}{ A } J_i$	$\partial_{i'} \varepsilon_{i'j'} E_{j'} = \rho'$
$\rho' = \frac{\rho}{ A }$	$\partial_{i'} \mu_{i'j'} H_{j'} = 0$

where i, j and k are the indices that take value from 1 to 3, ρ being the electric charge density, J the electric current density, ε the permittivity and μ the permeability. ∂_i is short for $\partial/\partial x_i$ and the “Levi-Cevita” tensor is expressed by ε^{ijk} which has a value of plus or minus unity (± 1) depending on the order of the indices [13].

We can conclude, from table 1. 1., two different choices under an arbitrary coordinate transformation:

- If the same constitutive parameters are used for the virtual and the transformed (physical) space, then the form of Maxwell's equations is modified.
- The transformed Maxwell's equations conserve the same general form as their classical counterpart, so long as the constitutive parameters and source terms are multiplied by the appropriate factors of the Jacobian matrix $[A]$ and its determinant (shown on the left side of Table 1. 1.)

In the following, the invariant form of Maxwell's equations will be taken into consideration and the variation of the domain's constitutive parameters will be tuned accordingly. It is important to note that, depending on the type of the coordinate transformation, the synthesized

medium is usually strongly anisotropic and spatially inhomogeneous. This aspect has to be taken into account when a practical implementation is required.

In the next sub-section, we introduce the TO techniques used to lower the profile of dihedral reflectors and the tracks followed in this area.

1. 2. C. Advances for flattened Dihedrals using TO media

Conducted researches focused on flattening the dihedral reflector to achieve a planar profile using TO methodologies as in [14, 15].

The authors of [14] introduce a rectangular TO medium that, when used over a planar reflector panel, can simulate the same retrodirective performance of the dihedral of the same aperture as shown in fig. 1. 7.

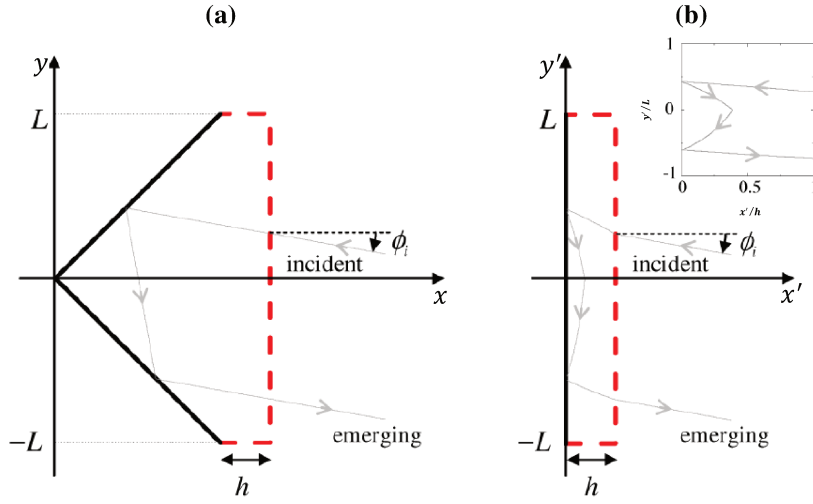


Figure 1. 7. Dihedral corner reflector in the virtual space (x, y) (a). Proposed flat reflector in the transformed physical space (x', y') (b). Black thick lines denote the PEC boundaries; red dashed lines delimit the free-space (a) and TO medium (b) regions involved in the transformation; grey thin arrowed lines indicate typical ray trajectories. The zoom in the inset highlights the negative refraction occurring in the transformation medium at the $(y' = 0)$ interface [14].

Using the general TO procedure (discussed in section 1. 1) they end up with the following material distribution ($[\varepsilon']$ and $[\mu']$ being the relative permittivity and permeability tensors) within the TO medium:

$$[\varepsilon'] = [\mu'] = \begin{bmatrix} \frac{h \left[1 + \left(\frac{x'}{h} - 1 \right)^2 \right]}{L + h - |y|} & \text{sgn}(y') \left(\frac{x'}{h} - 1 \right) & 0 \\ \text{sgn}(y') \left(\frac{x'}{h} - 1 \right) & 1 + \left(\frac{L - |y'|}{h} \right) & 0 \\ 0 & 0 & 1 + \left(\frac{L - |y'|}{h} \right) \end{bmatrix} \quad (1-6)$$

From eq. (1-6), the anisotropy is evident due to the different components obtained within the material distribution. Spatial inhomogeneity is also obtained since the material components vary along x and y .

While the authors argue that such a medium can be achieved using exotic materials, they do not offer any means to realize such a distribution. In fact, it is clear that it adds great complexity to the design of the planar reflector when compared to the easily implemented classical corner reflector (using two metallic panels only).

In [15], authors are able to push another TO medium conceived for the planar reflector towards realization. They obtain a non-magnetic material distribution within the TO domain (assuming the planar reflector operates at just one linear polarization). Eq. (1-7) describes the simplified material distribution for the conventions used in fig. 1. 8. with a TM polarization (E-field along the x -axis).

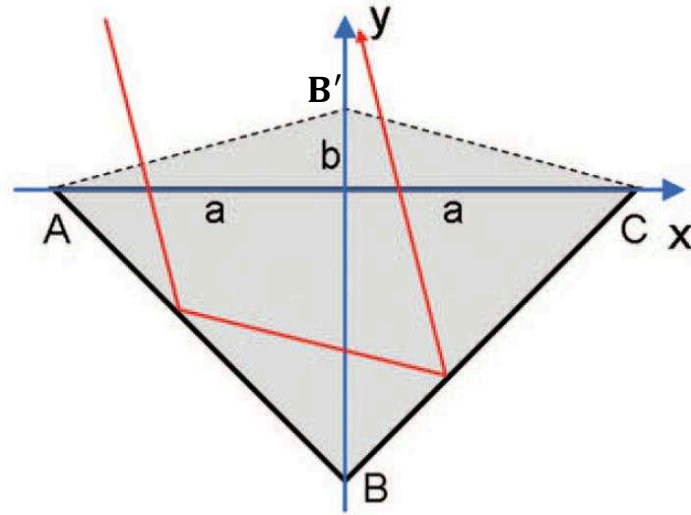


Figure 1. 8. Dihedral corner reflector in ABC along with the Proposed flat reflector with the TO (physical) domain denoted by AB'C. Black thick lines denote the PEC boundaries; dashed lines delimit the TO medium; a and b being the dimensions of the TO medium for a planar reflector of aperture AC with a length equal to 2a; red arrowed lines indicate typical ray trajectories in the classical dihedral [15].

$$[\varepsilon'] = \begin{bmatrix} \frac{(a+b)^2}{b^2} & -\text{sgn}(x) \frac{(a+b)}{b} & 0 \\ -\text{sgn}(x) \frac{(a+b)}{b} & 2 & 0 \\ 0 & 0 & \frac{(a+b)^2}{b^2} \end{bmatrix} \quad (1-7)$$

$$\text{and } [\mu'] = \begin{bmatrix} 1 & 0 & 0 \\ 0 & 1 & 0 \\ 0 & 0 & 1 \end{bmatrix}$$

From eq. (1-7), it is clear that such a distribution eliminates variations within the TO domain which lowers its complexity. The inconvenience here, is that they ended up with a TO

medium made of dielectrics that needs the exact same dimensions (for $a = b$) as the classical reflector for proper retrodirective operation as shown in fig. 1. 9.

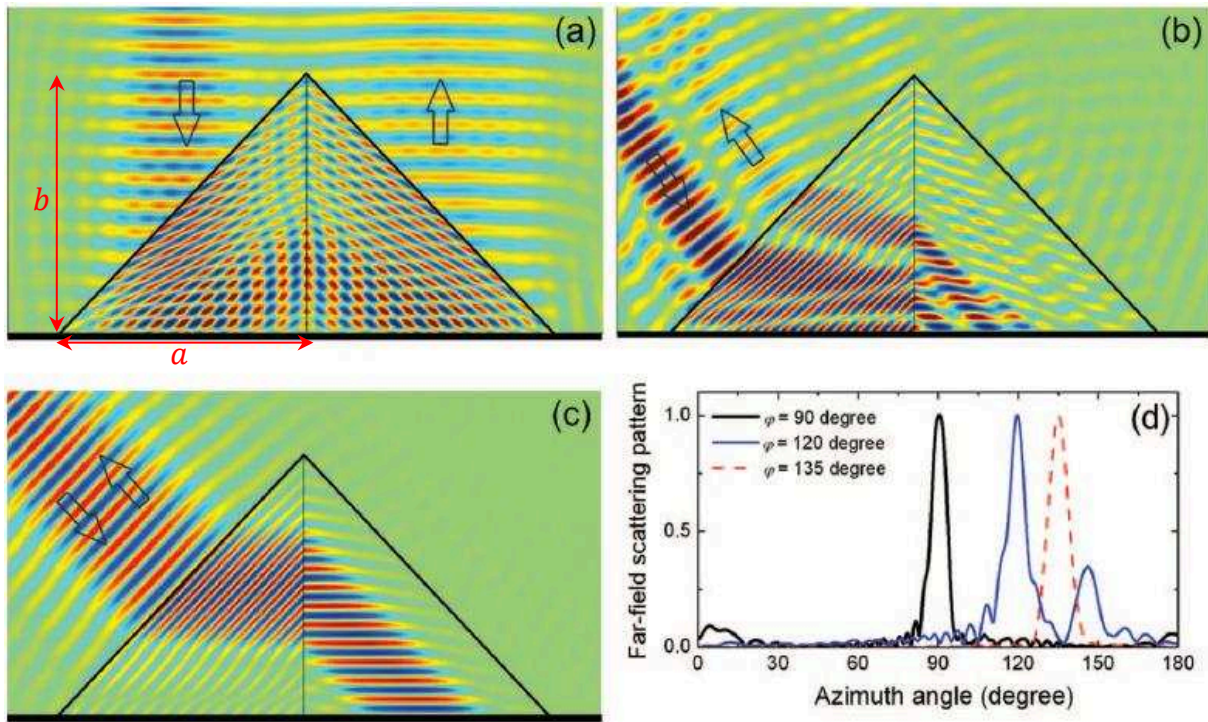


Figure 1. 9. Near electric field distributions (time domain) of the proposed non-magnetic retrodirective reflector (dimensions $a = b$) for incident wave at incidence angle $\varphi = 90^\circ$ (a), $\varphi = 120^\circ$ (b), and $\varphi = 135^\circ$ (c). The thick black line indicates the planar PEC sheet and the incidence angle φ here is θ in our conventions. Normalized far-field scattering patterns (d).

We can determine from the conducted researches using TO methodology that while very attractive, they all came at the cost of very complex realization for such profiles of the dihedral reflector. We now present Surface Impedance Modulation along with the advances in that domain.

1. 3. Background on Surface Impedance Modulated Panels

The desire to integrate EM devices onto the surfaces of satellites, vehicles and other existing platforms has driven huge interest in surface impedance panels in recent years. They are the two-dimensional counterpart of these volumetric metamaterials. They consist of scatterers or apertures, arranged along a surface, that exhibit unusual reflection, transmission, or dispersion properties [21]. They occupy less space, may exhibit lower losses, and are usually simpler to fabricate than volumetric metamaterials. One of the more popular, and perhaps more obvious, applications of impedance surfaces is low profile, high gain, planar antennas [22-26]. They are considered as tunable surface impedance antennas. They show great promise for consuming less power and occupying less space than power-demanding phased arrays [79] and bulky mechanical steering solutions. This thesis will focus primarily on reflective practical Surface Impedance Modulated (SIM) panels and their properties.

All SIM panels involve a reflection law that can be derived from geometrical optics. It is basically a phase discontinuity between the incident and reflected fields as detailed in [27]. Here, linear phase shifts along the localities that make up the panel are used to alter the direction of the incident field. We assume an incident plane wave is impinging over the panel and a plane wave is being reflected in a desired direction as shown in fig. 1. 10.

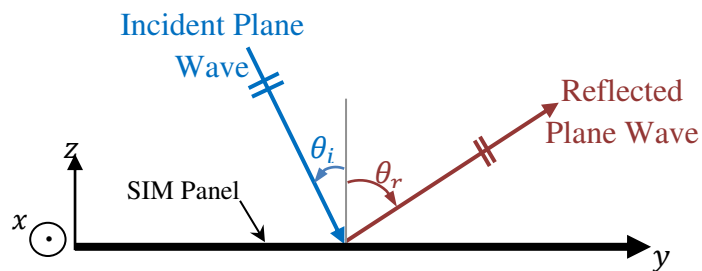


Figure 1. 10. SIM panel (along y-axis) redirects an incident plane wave that impinges with an angle θ_i into to a reflection angle $\theta_r \neq \theta_i$. This is done by introducing phase discontinuities along the panel.

These panels are then discretized into distinct elements often called “unit cells” and implemented using printed technologies and are often called “reflective metasurfaces”. They consist of a metallic cladding over a grounded dielectric substrate as illustrated in fig. 1. 11. In other words, the metallic top layer of the substrate is patterned in order to achieve the desired surface impedance.

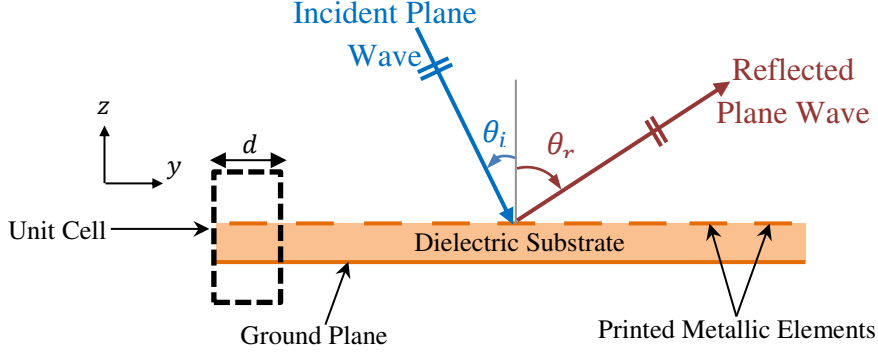


Figure 1. 11. Practical SIM panel geometry (cross section view) showing the incident and reflected plane waves; d being the unit cell's dimension.

In the next section, we first introduce the base element that constitutes the total practical SIM panel along with the procedure used in literature that leads to the implementation of the desired reflection law.

1. 3. A. Phase Shifting Unit Cell

The phase shifting cell is the base element of a practical SIM panel. In fact, for a given geometry, the global performance of the panel depends mainly on the performance of its constituting base element. For this sole purpose, an optimization procedure of the element or “Unit Cell” is needed in order to reduce losses and insure that the right phase law is applied over the panel. This in turn yields the desired direction for its reflected fields. In a passive panel, for instance, the phase of each cell is controlled by acting over its geometry.

1. 3. A. i. Calculation of the introduced phase

Consider a phase shifting cell illuminated by an incident plane wave, defined by its wave vector \vec{k}_i (which determines its direction of propagation) and its polarization (supposedly linear).

The impinging plane wave hits the surface of the cell with given incident angles (θ_i, ϕ_i) and polarization defined with the incident E-field vector $\vec{E}_i = \begin{bmatrix} E_i^\theta \\ E_i^\phi \end{bmatrix}$ (along \vec{a}_θ and \vec{a}_ϕ which are the unit vectors of the spherical system). Once the wave hits the surface of the cell, it is reflected with a phase shift introduced by the radiating element. If the cell is positioned in the center of a periodic infinite array, the reflected wave is considered as a plane wave. The direction of reflection is determined by the wave vector \vec{k}_r with (θ_r, ϕ_r) direction of propagation and polarization determined by $\vec{E}_r = \begin{bmatrix} E_r^\theta \\ E_r^\phi \end{bmatrix}$. The cell's response can then be represented with the following reflection matrix:

$$[\Gamma] = \begin{bmatrix} \Gamma_{\theta\theta} & \Gamma_{\theta\phi} \\ \Gamma_{\phi\theta} & \Gamma_{\phi\phi} \end{bmatrix} \quad (1-8)$$

Along with:

$$\begin{bmatrix} E_r^\theta \\ E_r^\phi \end{bmatrix} = [\Gamma] \begin{bmatrix} E_i^\theta \\ E_i^\phi \end{bmatrix} \quad (1-9)$$

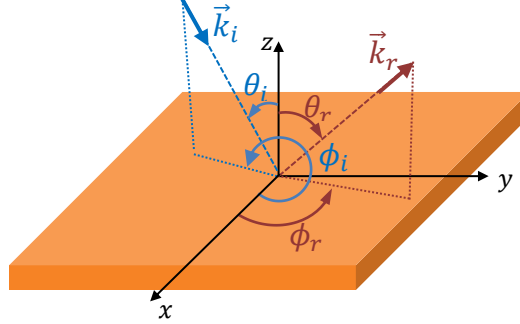


Figure 1. 12. Phase shifting unit cell with the conventions used for incidence and reflection.

The different $[\Gamma]$ components in eq. (1-8) are actually complex constants with each having a magnitude and phase.

In this thesis, for the sake of unification of the results, all SIM panel configurations are simulated with an E-field polarized along \vec{a}_θ with $\phi_i = 270^\circ$ and $\phi_r = 90^\circ$ (yz plane).

The phase introduced by the cell is equal to the phase ϕ_Γ of $\Gamma_{\theta\theta}$.

1. 3. A. ii. Phase Response of the Unit Cell

To realize the desired phase values for each unit cell, one should start by generating a set of data for the phase of the reflected field of a uniform infinite array of identical printed elements versus their control parameter (often their size). This infinite array approach [22, 28], which assumes all surrounding unit cells are identical, only approximates the final situation where different elements are put to constitute the practical SIM panel, but has been shown to be a good approximation. The desired phase that is to be produced by the element changes gradually on the surface of the panel. Therefore, each locality can be assumed to be an infinite periodic structure that is illuminated by a plane wave whose angle of incidence θ_i is defined from the desired configuration. The infinite periodic structure approximation also takes into account an approximation of the mutual coupling effects due to surrounding elements which gives additional importance to this approach.

In this thesis, the full-wave analysis to obtain the reflection phase response has been conducted using the commercial software ANSYS[®] HFSS[®]. HFSS is based on the finite element method (FEM), and simulates the infinite array approach by using appropriate periodic boundary conditions (theoretical waveguide simulation). Its reliability has been proved practically in [29] through comparing theoretical waveguide simulation results with the results of an equivalent experimental waveguide using the same element. Fig. 1. 13. shows an example of a printed dipole element unit cell in an infinite periodic simulation.

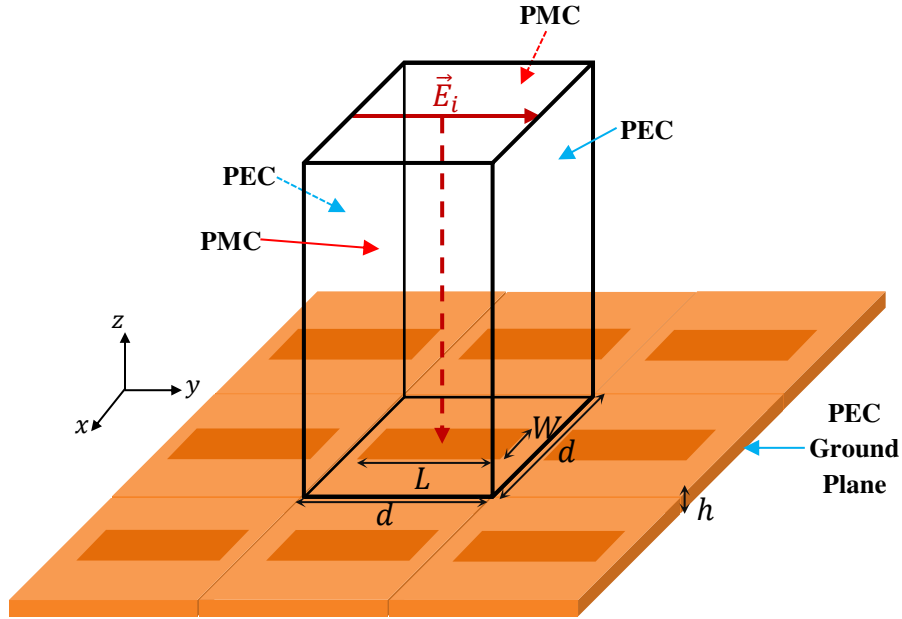


Figure 1. 13. Illustration of a Printed Dipole element unit cell as part of an infinite periodic structure (Phase De-embedding is represented by the dashed red line brought to the surface of the printed element) .

It should be noted, with reference to Fig. 1. 13., that the use of PEC and PMC sheets restricts the configuration to normal incidence. De-embedding is the reference plane chosen within the simulation to measure the phase component ϕ_{Γ} of the reflection coefficient (usually being the plane of the printed element). Second, if the E-field is y -directed then the dimension of the rectangular dipole element along the x -axis (width W) is fixed and its dimension along the y -axis (length L) is varied.

The phase response of the reflected field versus dipole's length is obtained using HFSS as shown in Figure 1. 14. Once the desired reflection phase response is obtained, the elements dimensions can be selected to satisfy any phase response ϕ_{Γ} required from the imposed phase law. In other words after all ϕ_{Γ} values are established, the corresponding required sizes, which satisfy these values, can be chosen from the generated reflection phase response.

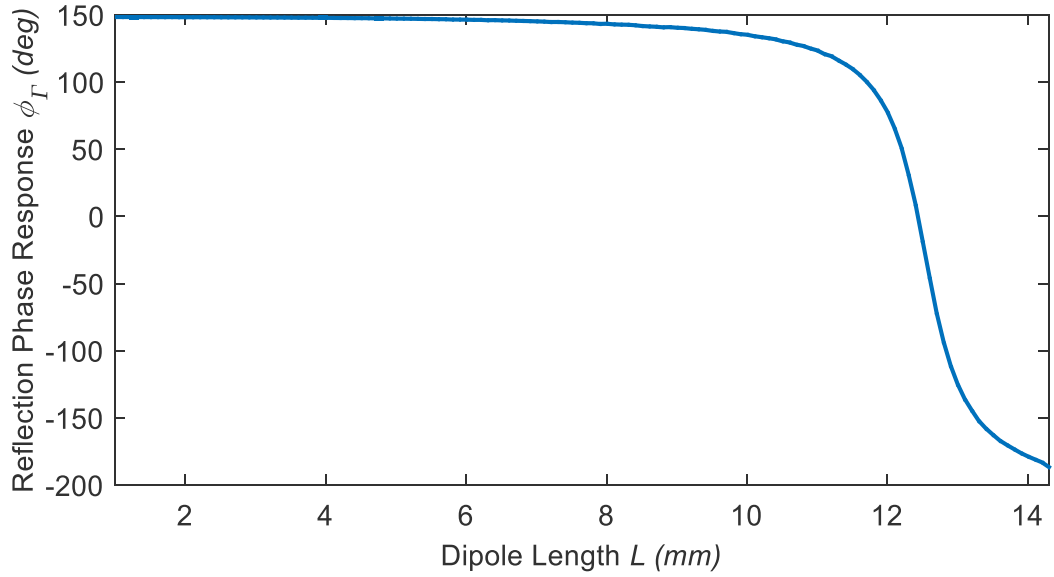


Figure 1. 14. Reflection Phase Response versus element length for a simulated infinite array of identical dipoles using HFSS for $W = 2mm$, $f = 8GHz$, $\theta_i = 0^\circ$, unit cell dimension $d = 0.388\lambda$ with the substrate used “Cuclad 5880” with $h = 1.6mm$.

In Fig. 1. 14., two phase related quantities are important. The first is the range of phase values actually achievable (ideally 360°). The second is the slope of the phase versus length curve. Regarding the attainable phase range, a 310° phase range is possible for dipole elements if a very thin substrate is selected ($h = 1.6mm$ in this case).

1. 3. A. iii. Types of Phase Shifting Unit Cells

One of the first proposed unit cells in printed technologies consisted of using a square patch element with fixed dimensions [30, 31]. The phase response of the reflected field is controlled using a stub with variable length protruding from the patch. To overcome the limitations introduced by the stub, a variable sized element was later introduced in [32]. The modification of the element’s size acts on the resonant state of the cell and consequently on the phase of the reflected field. The example scenario, discussed in section 1. 3. A. ii., uses this type of cell.

From these types of unit cells came along different multi-resonant [33, 34], mono-layered [35] and multi-layered passive solutions [36]. There exist in literature also many more different solutions including reconfigurable solutions as in [37-39].

Recently, research orientation is going towards miniaturizing the phase shifting unit cell. The slotted unit cell incited the implementation of miniaturized unit cells with dimensions $d < \frac{\lambda}{2}$. It is proven, in [40] that the smaller the interspacing between elements (which is equivalent to d in this case) the smoother is the phase shift along the panel and the better the bandwidth. Though decreasing d means a smaller phase range ($< 300^\circ$), many research showed promise specifically for reflectarrays as in [41, 42].

1. 3. B. Advances in Flattened Dihedrals using SIM Panels

This approach acts over the panels of the corner reflector. The authors of [43-46], use practical SIM Panels to lower the profile of the dihedral while preserving its retrodirective performance. This method consists of using given phase laws (discussed more in details in the next section) over both panels. For implementation, passive phase shifting cells with grounded dielectric substrate were used instead of the PEC panels found for the classical corner reflector. Though, this method is not able to achieve a planar reflector, it is easily realized and in [43-46] different prototypes are fabricated and prove the concept. An illustration of the flattened dihedral is shown in fig. 1. 15.

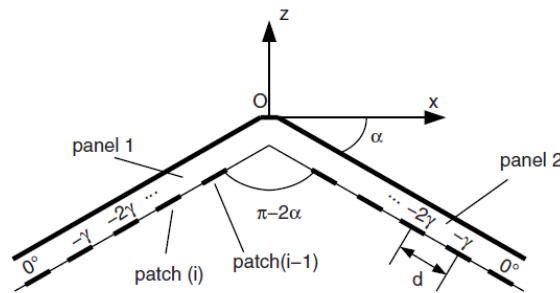


Figure 1. 15. Concept of a flattened dihedral reflector; α being the inclination angle (with $\alpha = 45^\circ$ for the conventional reflector), d the inter element spacing and γ the phase shift between two adjacent patches [43].

While the research, that adopts this approach, is able to lower the bulky profile of the conventional corner reflector, it degraded its retrodirectivity performance to certain extent. The panels used are correspondingly known to be quite sensitive to the incidence angle. The RCS results reported in fig. 1. 16. show a glimpse of the performance degradation obtained when comparing the flattened reflector to the conventional one.

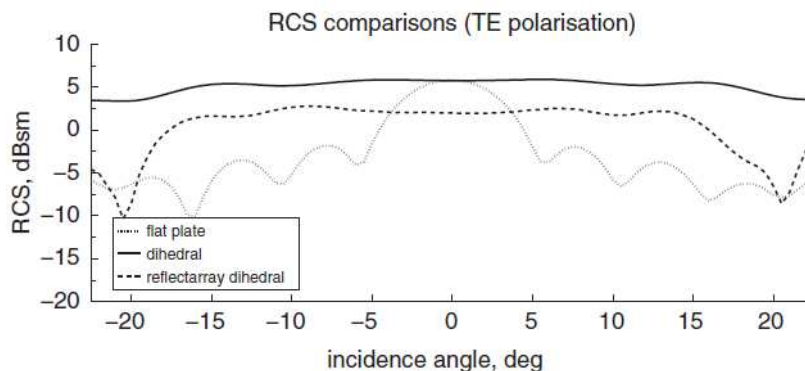


Figure 1. 16. RCS comparison between a flat plate, a conventional dihedral and the proposed flattened dihedral of the same aperture for TE polarization in [43].

To sum up this section, SIM panels allow flattening of the dihedral reflector but actually degrade the global retrodirective performance when compared to that of the conventional one.

1. 4. The Image Lobe Concept

While the practical SIM approach is interesting and pushes the theory towards more concrete panels that can be used for lowering the dihedral's profile. It introduces a new phenomenon related to the parasitic lobes which is widely known as the “image lobe”.

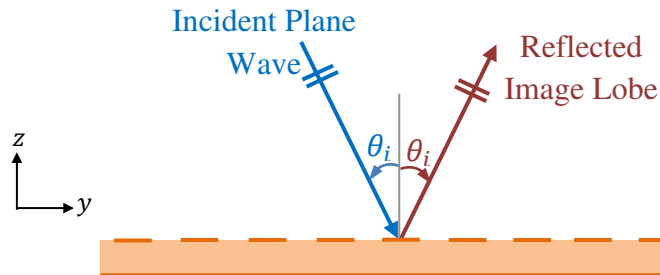


Figure 1. 17. Practical SIM panel geometry (cross section view) showing the incident plane wave and the direction of the “image lobe”.

The authors of [47] observed what is shown in fig. 1. 17. what is referred to as an “image lobe”, and attributed it to the scattering from the ground plane due to the fact that large portions of the panel’s ground plane are not “shadowed” by the printed elements and hence are directly exposed to the incident fields. To reduce the amount of uncovered surface on the plane of the elements, triangular unit cells were used in [47] instead of the conventional square one (discussed in section 1. 3.). Although the results in [47] showed a slight improvement of the measured image lobe level, it persisted. The authors of [48] adopted a similar view, and found through full-wave simulations of reflectarrays consisting of fixed width and variable length dipoles that as the width of the dipoles increases the image lobe level decreases, and thus suggested that the image lobe level might be proportional to the amount of ground plane directly exposed to the incident field.

On the other hand, the authors of [49, 50] deduced that the appearance of an image lobe in reflectarrays might be due to the periodic error occurring in the actual reflection phase of the elements. An abrupt change in the element size occurs almost periodically for such panels. This change causes the environment of the elements to depart significantly from that of the infinite periodic structure assumed in the calculation of the reflection phase response versus element size database. Hence, this leads to higher levels for this lobe than desired reflected fields in certain directions.

In this thesis, we show that the intuitive notions in [47-50] are partly true, but not entirely for the reasons given.

In [51] a description was given on how to “tune-out” the image lobe in reflectarrays by increasing the thickness of the substrate in order to result destructive interference between the reflected fields from the elements on the top layer of the panel and that from the ground plane. The use of this methodology is actually possible when all elements have fixed size, and element phases are controlled by stubs.

With the different types of elements we are using in this thesis, the range of achievable reflection phases versus elements size decreases significantly if the substrate thickness is increased. Thus the substrate height must be as thin as possible (a very small fraction of a wavelength) to end up with a good panel design, and so the technique proposed in [51] cannot be used here.

1.5. Conclusion

This first chapter briefly introduces the retrodirective reflector as a potential EM device used for radar and antenna applications. The need to lower its bulky profile is also discussed. Different methodologies are presented to reduce its size all the while preserving its performance.

Transformation optics offers a first possible solution that acts over the filling volume of the reflector. Different TO media show promise in lowering the dihedral's profile at the cost of complexity in realization.

Surface impedance modulation introduces another promising answer to decrease its size. Such a methodology acts over the surface panels of the dihedral to deviate the reflected fields to desired reflections which insures flattening of the reflector to some extent. Their practical implementation along with the existing base element models are categorized and analyzed. Parasitic reflections, which are one of the hidden inconvenients for SIM panels, are also analyzed. By reviewing the development history associated with those parasitic reflections, new revelations might offer explanations to their source along with new solutions to mitigate them.

In the next chapter, we apply a more practical TO approach to the dihedral than what is used in literature. It consists of a compression technique for the conventional reflector. Then, we push the conceivable TO medium towards realization.

Chapter 2 - Compression Technique for Retrodirective Reflectors Using Transformation Optics

Transformation optics (TO) promises the capability of bending light, EM waves and energy, in any desired manner and for any desired application. Maxwell's equations do not vary though coordinates transform. Hence, it is the values of permittivity and permeability that are modified.

By controlling the permittivity and permeability in a TO medium, it is possible to design an enhanced and engineered material. Therefore, TO is a new methodology for creating novel and unique optical and electromagnetic devices.

First proposed in [4, 5, 8], TO might present potential solutions for some of the drawbacks associated with a classical retrodirective reflector. Such limitations and some of the TO solutions are discussed in the next section. Thus, a retrodirective reflector with a TO medium is investigated in this chapter.

In the first section of the chapter, the problem is discussed along with a compression technique based on TO and applied on a classical reflector. A rigorous analysis of the compressed reflector's performance is also conducted for a normally incident wave. In the second part, the practicality of the design along with different simplifications and approximation procedures are discussed. In the third section, the effective medium theory (EMT) approach is proposed as an implementation of the theoretical design. Last, in the fourth part, concluding remarks are presented discussing the effects of the compression technique along with the impact of using the EMT approach to the implementation of such an application.

This chapter relies solely on Full wave simulations over COMSOL Multiphysics for validations.

2. 1. Background & Design of TO Compressed Reflectors

2. 1. A. Problem Statement

The retrodirective reflector is a device that can reflect EM waves back directly towards the source. Such a device is mainly useful for maritime and spatial radar identification applications as previously discussed in chapter 1. A classical retrodirective reflector can be designed using a corner reflector structure that consists of metallic conducting sheets with an angle of 90° in between.

However, for most applications mentioned, the classical reflector is quite cumbersome to be integrated. So, lower profile features are needed. Many researches have already applied successfully different TO methodologies to design low-profile EM reflectors including the retrodirective reflector in [14, 52, 53]. However, those attempts lead to inhomogeneous anisotropic materials covering the conducting sheets of the reflector.

These configurations, while they were attractive and close in performance to the classical reflector in theory and simulation, are either very complex or even unattainable with current fabrication technologies.

The latest research [15] in the field of corner reflectors is able to simplify the material distribution in the TO domain to a certain extent and obtain a planar profile. However, the retrodirectivity performance is quite degraded. Moreover, although the obtained profile is flat, the overall dimensions are not reduced. In the end, the main difference is that the bulkiness comes from dielectrics instead of the metallic sheets. In this chapter, the goal is to obtain a lower profile for the reflector and reduce its bulkiness by using a particular TO compression technique.

2. 1. B. Proposed Theoretical Design

Consider a retrodirective dihedral corner reflector as shown in figure 2. 1.

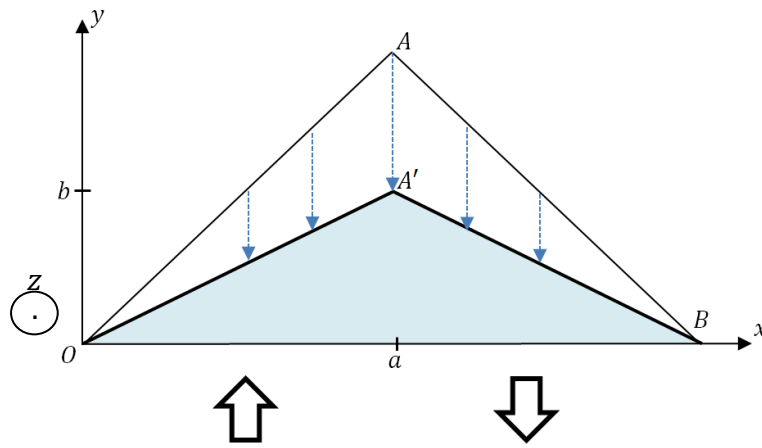


Figure. 2. 1. The original 2D space of a corner reflector with its proposed transformation.

For simplicity, it is restricted to a two dimensional (2D) space. The original dihedral reflector has two perfect conducting (PEC) planes OA and AB perpendicular to each other. The big arrows in figure 2. 1. represent the normally incident and reflected beams of the reflector.

Transformation optics methodology can be employed in order to transform such a corner reflector to a lower one. The coordinate transformation chosen in this scenario is schematically shown by the small arrows in fig 2. 1. from lines OA and AB to lines OA' and $A'B$. Only the y -coordinate has been transformed in a linear way as shown in equations (2-1, 2-2 and 2-3):

$$x' = x \tag{2-1}$$

$$y' = \frac{b}{a}y \tag{2-2}$$

$$z' = z \tag{2-3}$$

where a and b represent the dimensions of the compressed reflector.

Under this coordinate transformation, the virtual space of the classical reflector (OAB) is transformed into a compressed area (highlighted area in fig. 2. 2.) in the physical space ($OA'B$).

Based on the TO procedure as in [3] and table 1. 1., one could calculate the relative permittivity and permeability tensors of the TO material filling using the following equations:

$$[\varepsilon'] = \frac{[A].[A]^T}{|A|} \cdot [\varepsilon] \text{ and } [\mu'] = \frac{[A].[A]^T}{|A|} \cdot [\mu] \quad (2-4)$$

where $[A]$ is the Jacobian matrix from eq. (1-4) of the coordinate transformation used in (2-1,2-2 and 2-3). The y -coordinate transformation of the region yields the following eq. (2-5):

$$[\varepsilon'] = [\mu'] = \begin{bmatrix} \frac{a}{b} & 0 & 0 \\ 0 & \frac{b}{a} & 0 \\ 0 & 0 & \frac{a}{b} \end{bmatrix} \quad (2-5)$$

As seen from eq. (2-5), the advantage of choosing such linear coordinate transformation is that the resulting material, although anisotropic, is homogeneous.

2. 1. C. Analysis of TO Compressed Reflector at normal incidence

As shown in the previous sub-section, the material tensor components are linked with the geometrical parameters of the reflector using (2-5). Here, different theoretical analyses of the reflector under normal incidence are conducted. These analyses give physical explanations of the compressed reflector operation.

2. 1. C. i. Phase Analysis:

Here, we consider a normally incident plane wave polarized along the x -axis (TM) at the point M with an initial phase $\phi_M = 0$ and propagating along $+y$. It propagates till point P as shown in fig. 2. 2.

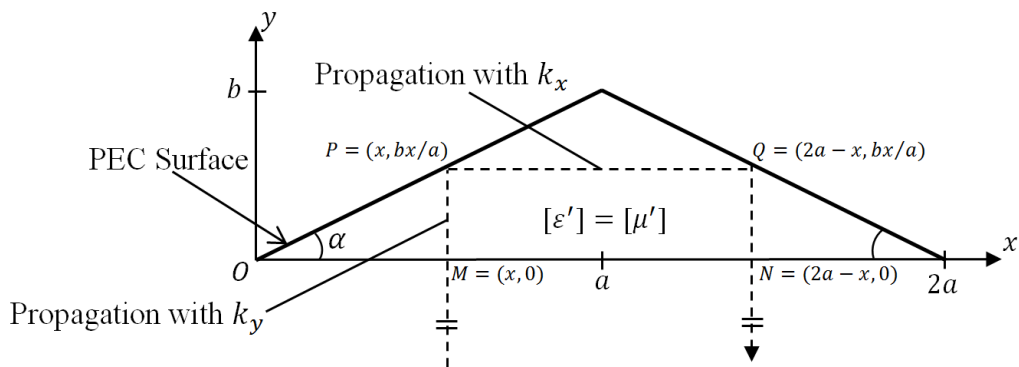


Figure. 2. 2. Wave Propagation within the TO compressed Reflector.

The Reflector domain is filled with the anisotropic material from eq. (2-5) so the wave propagation within this material depends on its tensor components. We note the wavenumbers as follows:

$$k_x = k_0 \quad (2-6)$$

for a wave polarized along $+y$ and propagating along x and

$$k_y = \frac{a}{b} k_0 \quad (2-7)$$

for a wave polarized along $+x$ and propagating along y .

The phase at point P is written as:

$$\phi_P = -k_0 x \quad (2-8)$$

The wave then undergoes a phase shift of π when it is reflected on the metallic panel. The reflected wave is redirected horizontally and then propagates along x with k_x . The wave now hits point Q after propagating a distance of $2a - x$. The phase at Q is given by:

$$\phi_Q = k_0 x + \pi - 2k_0 a \quad (2-9)$$

It undergoes then another phase shift and is redirected to point N with a phase given by:

$$\phi_N = 2\pi - 2k_0 a \quad (2-10)$$

This verifies that the redirected wave by the compressed reflector is independent of x . The anisotropy of the material thus guarantees that a plane wave at normal incidence will emerge in the form of a plane wave normally at the out bounds of the reflector.

2. 1. C. ii. Reflection Law Analysis:

We consider, first, that the incident field $\vec{E}^{inc}(M) = E_0 \vec{e}_x$ (no reflections over the reflector's interface Ox). The reflection law also requires that the tangential component of the total electric field vanishes on the PEC surface of the reflector.

We note:

$$E_x^{inc}(P) = E_0 e^{j\phi_P} \quad (2-11)$$

being the x component of the incident field at point P .

The resulting tangential component (along x' , see Fig. 2. 3.) at P can be written as follows:

$$E_{tan}^{inc}(P) = E_0 e^{j\phi_P} \cos \alpha \quad (2-12)$$

where α is the inclination angle of the reflector's PEC surface.

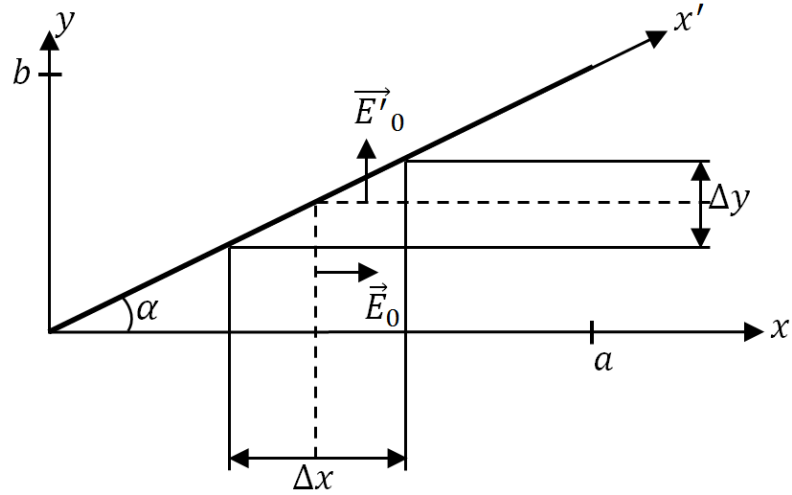


Figure. 2. 3. Wave Propagation within the TO compressed Reflector.

Similarly, we note:

$$E_y^{ref}(P) = E'_0 e^{j\phi'_P} \quad (2-13)$$

being the y component of the reflected field at point P . The resulting tangential component is:

$$E_{tan}^{ref}(P) = E'_0 e^{j\phi'_P} \sin \alpha \quad (2-14)$$

Now, using (2-12 and 2-14), in order to cancel out the total tangential component over the reflector's surface, the following should be met:

$$E_0 e^{j\phi_P} \cos \alpha = -E'_0 e^{j\phi'_P} \sin \alpha \quad (2-15)$$

Which leads to the following:

$$\begin{cases} E'_0 = \frac{a}{b} E_0 \\ \phi'_P = \phi_P + \pi \end{cases} \quad (2-16)$$

So the phase of the reflected field at P is shifted with π but also the amplitude is modified with a ratio of $\frac{a}{b}$.

2. 1. C. iii. Power Analysis:

To better see the impact of this amplitude modification from eq. (2-16), we calculate the power transported by the incident wave in a Δx beam width as shown in figure 2. 3.

The wave impedance for the incident field is:

$$\eta_y = \eta_0 \quad (2-17)$$

The power is then proportional to the following:

$$\frac{|E_0|^2}{\eta_0} \Delta x \quad (2-18)$$

Now for the reflected field, the wave impedance is as:

$$\eta_x = \eta_0 \quad (2-19)$$

The power is concentrated within Δy and is written as:

$$\frac{|E'_0|^2}{\eta_0} \Delta y \quad (2-20)$$

On the other hand, from fig. 2. 3., we have:

$$\Delta y = \frac{b}{a} \Delta x \quad (2-21)$$

The power is also proportional to the following:

$$\frac{|E'_0|^2}{\eta_0} \frac{b}{a} \Delta x \quad (2-22)$$

Using (2-18 and 2-22) to insure power conservation between incidence and reflection, we get the following:

$$\frac{|E'_0|^2}{\eta_0} \frac{b}{a} \Delta x = \frac{|E_0|^2}{\eta_0} \frac{a}{b} \Delta x \quad (2-23)$$

So (2-23) leads to $|E'_0| = \frac{a}{b} |E_0|$ which is the same condition obtained for the tangential components in (2-16). Power conservation is then clearly guaranteed for the TO compressed Reflector since it is in line with the use of the anisotropic medium.

In conclusion, the reflection phase analysis and the power conservation model agree over the fact that the field amplitude is altered (which is not that intuitive). It actually depends on the geometry of the retrodirective reflector or in other terms the compression of the reflector.

2. 1. D. Simulation Settings for TO Compressed Reflector

To demonstrate the proposed transformation, full wave 2D EM simulations are conducted through COMSOL Multiphysics simulator. Two different compressed reflectors are considered with $a = 2b = 15\lambda_0$ and $a = 4b = 15\lambda_0$, where λ_0 is the free space wavelength at the operating frequency $f = 8GHz$. For the sake of analyzing the results, a Gaussian beam is used at normal incidence in all simulations with a beam width $w = 4\lambda_0$ and positioned at $X = -7.5\lambda_0$ from the center of the reflector and at a distance $D = 20\lambda_0$. These settings are

shown in fig. 2. 4. Here, near field maps of the electric fields show if the TO compressed reflectors maintain the retrodirectivity of a classical reflector. Perfectly matched layers (PML), placed around the configuration domain, insure that no reflections from this domain's boundaries interfere with the reflector's performance.

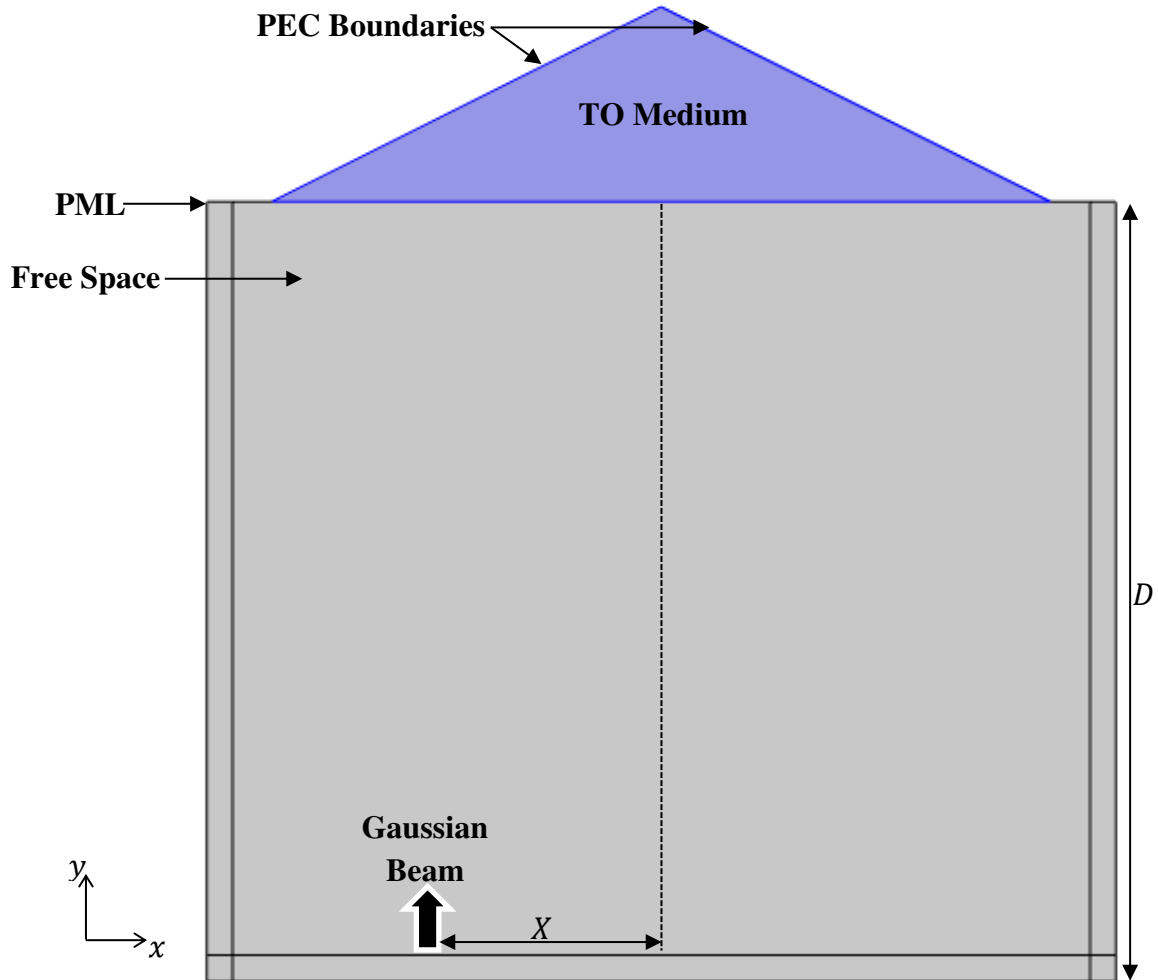


Figure. 2. 4. Simulation Configuration for the Compressed Reflector using TO for $a = 2b$.

2. 1. E. Simulation Results of theoretical TO compressed reflectors

The amplitudes of the total electric field are compared in fig. 2. 5. The black arrows represent the direction of propagation of the TM polarized EM-field.

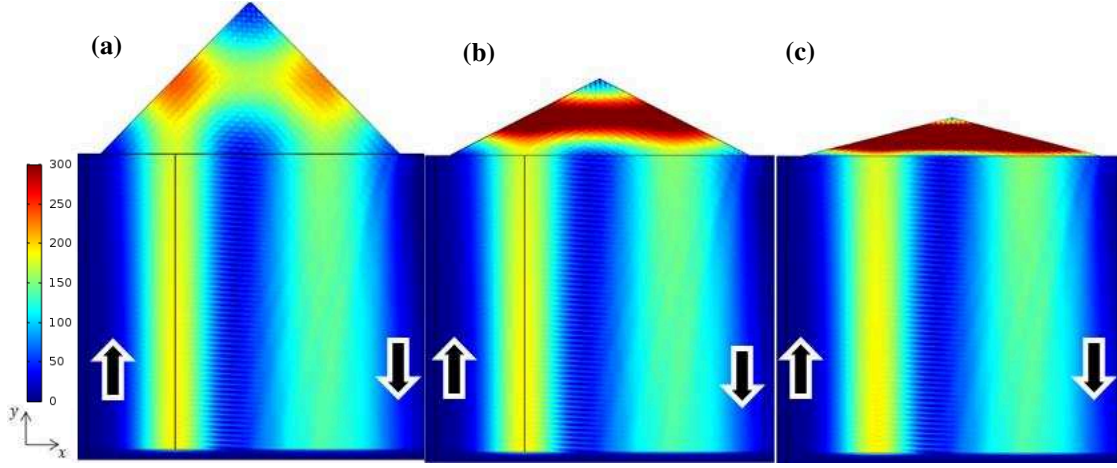


Figure. 2. 5. Total complex Electric field amplitudes (V/m) at normal incidence for Classical Reflector (a), Compressed Reflector using TO for $a = 2b$ ($\epsilon'_x = \mu'_x = 2, \epsilon'_y = \mu'_y = 0.5, \epsilon'_z = \mu'_z = 2$) (b), for $a = 4b$ ($\epsilon'_x = \mu'_x = 4, \epsilon'_y = \mu'_y = 0.25, \epsilon'_z = \mu'_z = 4$) (c).

As seen from fig. 2. 5., the retro-directivity performance of the classical reflector is conserved for any compression factor when using theoretical TO domains with their accordingly material distributions.

It is important to note that the field amplitudes between incidence and reflection, for all configurations simulated in fig. 2. 5., are gradually varying. This is solely related to the expansion of the Gaussian beam's width along its propagation.

2. 2. Practical TO compressed reflector Designs

2. 2. A. 1st material simplification procedure

While the performance of the TO compressed reflectors obtained in sub-section (2. 1. E) are identical to that of the classical reflector, the TO media is still theoretical and unrealizable. This is mainly due to the presence of relative permittivity and permeability tensor components within the same confined space of the designed material as indicated in eq. (2-5).

As a way to simplify the obtained material tensors, in order to reduce the complexity of the design, a specific material suitable for only one incident wave polarization can be chosen. For linearly polarized field, specific components from the material tensors can be applicable for the design. For instance, transverse magnetic (TM) incident waves, only the ϵ'_x , ϵ'_y and μ'_z components are related to the incoming and reflected fields and thus other components are eliminated or can be of any arbitrary value.

2. 2. B. 2nd material simplification procedure

We now aim at further simplifying the obtained distribution from sub-section 2. 2. A and obtain a non-magnetic material for the sake of simplicity in execution later on.

As proven in [54], the material parameters of a medium under a coordinate transformation can be altered using a different Material Interpretation. This is true only if the EM ray trace of

both interpretations is equivalent. In the reflector's scenario, this means preserving its retrodirectivity for any material interpretation.

Practically, the material interpretation adds one more degree of freedom to the designed material. Here, the parameters can be simplified such that the product of the following components $\varepsilon'_x \mu'_z$ and $\varepsilon'_y \mu'_z$ is unchanged. This ultimately permits us to eliminate either the relative permittivity tensor $[\varepsilon']$ components or the permeability tensor $[\mu']$. At this point, μ'_z is reduced to 1 since a non-magnetic material is needed for the design.

This leads to the following relative tensors:

$$[\varepsilon'] = \begin{bmatrix} \frac{a^2}{b^2} & 0 & 0 \\ 0 & 1 & 0 \\ 0 & 0 & \varepsilon'_z \end{bmatrix}, [\mu'] = \begin{bmatrix} \mu'_x & 0 & 0 \\ 0 & \mu'_y & 0 \\ 0 & 0 & 1 \end{bmatrix} \quad (2-24)$$

In eq. (2-24), ε'_z , μ'_x and μ'_y could be arbitrary value because of the 2D-space restriction and the material simplifications conducted.

It is important to add here that if we assume that $\varepsilon'_z = \varepsilon'_x = \frac{a^2}{b^2}$, then this non-magnetic anisotropic material can be considered uniaxial. Consequently, this parameter distribution can be approximated using birefringent materials (in other terms double refractive).

However, it is known that the reduction to non-magnetic parameters (especially here $[\mu'] = 1$) comes at the expense of introducing impedance mismatch at the interface of the reflector.

In the adopted configuration, the normally incident wave passes from the impedance of free space η_0 to $\eta_y = \frac{b}{a} \eta_0$ of the anisotropic medium from (2-17) through the reflector's interface. Here, a reflection coefficient at the interface $\Gamma_{int} = \frac{\eta_y - \eta_0}{\eta_y + \eta_0} \neq 0$ is obtained. This means that using (2-24) as a medium filling the reflector yields reflection losses. These losses actually depend on the $[\varepsilon']$ tensor components which are in turn related to the dimensions of the reflector. Higher compression $\frac{a}{b}$ means higher ε'_x component and more losses along the interface at normal incidence.

2. 2. C. Simulation results of the practical TO compressed reflector design

In this section, the same settings of section (2. 1. D) were used. The difference resides within the TO material distribution, using that of (2-24).

2. 2. C. i. Comparative Results for different compressed reflectors:

Two different reflector configurations are simulated (one with $a = 2b = 15\lambda_0$ and one with $a = 4b = 15\lambda_0$) as shown in fig. 2. 6.

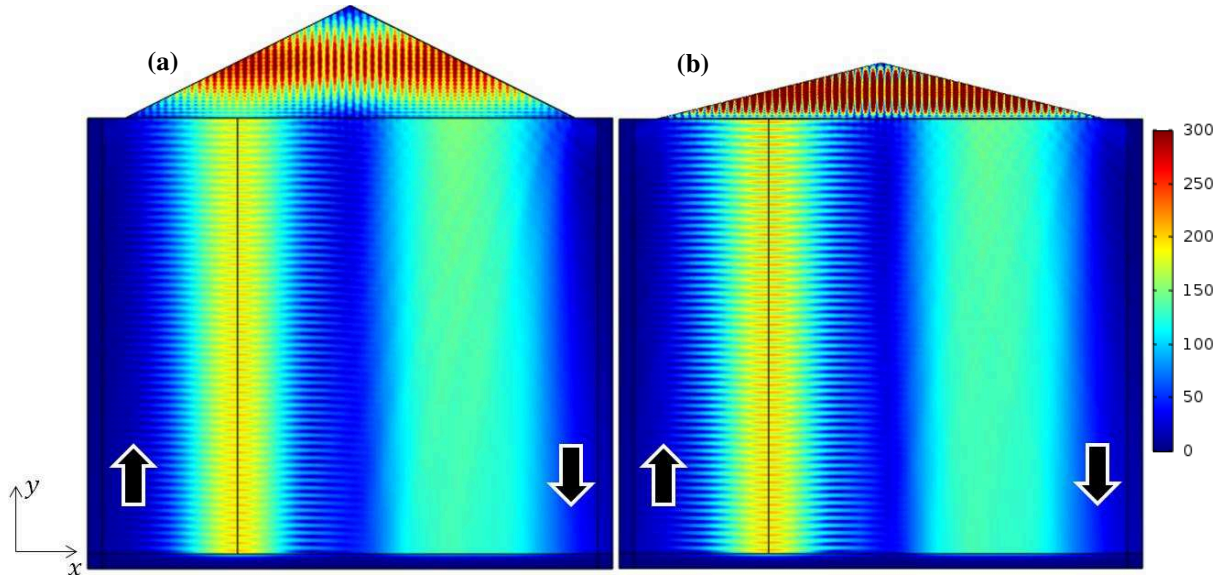


Figure. 2. 6. Total complex E-field amplitudes (V/m) with Reduced μ' of the TO domain for $a = 2b$ ($\epsilon'_x = \epsilon'_z = 4, \epsilon'_y = 1$) (a) and $a = 4b$ ($\epsilon'_x = \epsilon'_z = 16, \epsilon'_y = 1$) (b).

Fig. 2. 6. shows the same overall retro-directive performance for the compressed reflectors using non-magnetic uniaxial anisotropic material.

Both configurations, in fig. 2. 6., show stationary waves (non-uniform oscillating amplitude values) over the interface within the complex E-field amplitudes. This is due to the impedance mismatch between free space and the non-magnetic TO media. Stationary waves confirm mismatch reflection losses over the interface which can be roughly calculated as follows:

$$\Gamma = 20 \log \left(\frac{|E_{max}| - |E_{min}|}{|E_{max}| + |E_{min}|} \right) \quad (2-25)$$

Where $|E_{max}|$ and $|E_{min}|$ are the maxima and minima values of the complex E-field amplitudes which were obtained from COMSOL simulations.

Table 2. 1. Presents the obtained reflection losses at the interface of both simulated configurations.

Table 2. 1. Comparison of Reflection Losses for different Retrodirective Reflectors.

TYPE of the Reflector	Reflection Coefficient Γ (dB)	
	Ideal TO material using (2-4)	Non – Magnetic Approximation using (2-25)
Compressed Reflector ($a = 2b$)	-30.7dB	-21.4dB
Compressed Reflector ($a = 4b$)	-30.7dB	-19.41dB

Table 2. 1. shows that reducing the material parameters to non-magnetic using the material interpretation from section (2. 2. B) introduce additional reflections. Furthermore, these results confirm that the losses increase while passing from the $a = 2b$ compression scenario to $a = 4b$ since higher values for the material parameters are needed.

Although reflections for both configurations exist, they are considered acceptable at this stage. From here on out, the $a = 2b$ configuration is selected for the upcoming sections since it benefits from lower tensor values all the while keeping a double compression rate when compared to the classical reflector.

2. 2. C. ii. Comparative Results for different tensor components:

It should be noted that another degree of freedom exists while choosing the permittivity tensor components and while keeping the same profile of the reflector ($a = 2b$). So the anisotropic factor ρ is introduced in (2-26):

$$\rho = \frac{\epsilon'_x}{\epsilon'_y} \quad (2-26)$$

Keeping $\rho = \frac{\epsilon'_x}{\epsilon'_y} = \frac{a^2}{b^2} = 4$ any two values of ϵ'_x and ϵ'_y can be used for implementation of the compressed reflector. Some examples are shown in fig. 2. 7.

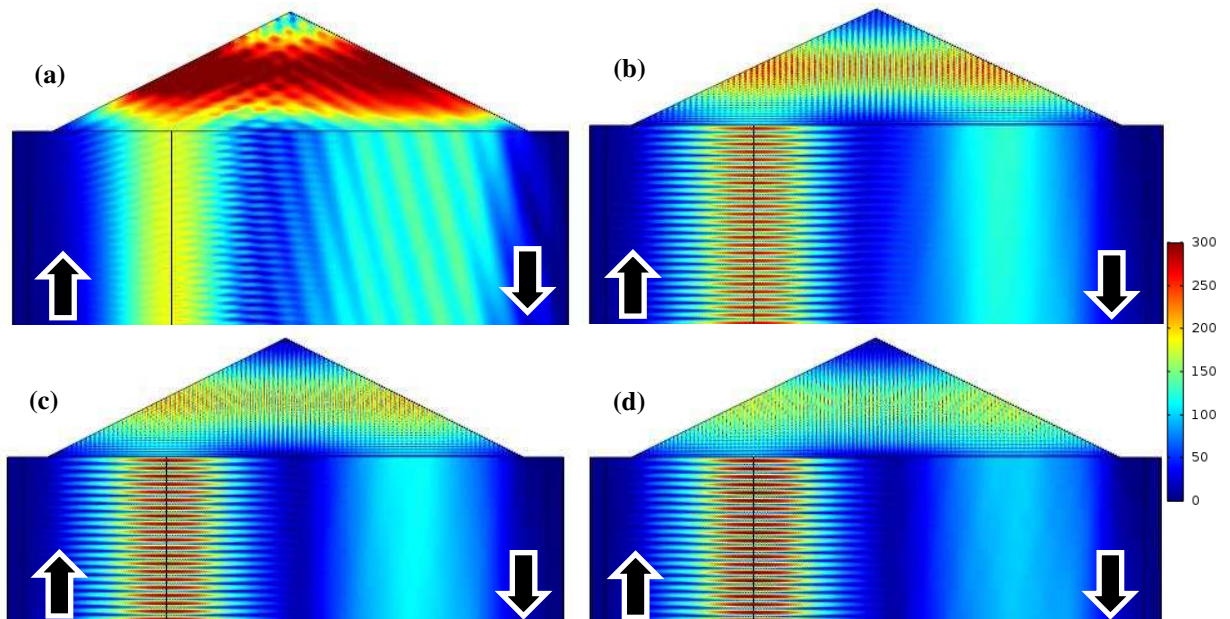


Figure. 2. 7. Total complex E-field amplitudes (V/m) with $a=2b$ dimensions using (2-24) for $\epsilon'_x = \epsilon'_z = 1$; $\epsilon'_y = 0.25$ (a) $\epsilon'_x = \epsilon'_z = 8$; $\epsilon'_y = 2$ (b), $\epsilon'_x = \epsilon'_z = 12$; $\epsilon'_y = 3$ (c) and $\epsilon'_x = \epsilon'_z = 16$; $\epsilon'_y = 4$ (d).

While different tensor components yield an identical overall retro-directive behavior for the compressed reflector, the compromise resides with higher reflection losses as the ϵ'_x component used increases as shown in table 2. 2.

On the other hand, trying to lower ϵ'_x is beneficial in terms of reflection losses to some extent but yields an $\epsilon'_y < 1$ which might add to the complexity of the material design when passing to realization.

Table 2. 2. Comparison of Reflection Losses for different tensor components.

Reflection Coefficient Γ (dB)	
Compressed Reflector ($a = 2b$) using (2-25) with $\rho = 4$	
$\epsilon'_x = \epsilon'_z = 1$ $\epsilon'_y = 0.25$	-23.5dB
$\epsilon'_x = \epsilon'_z = 4$ $\epsilon'_y = 1$	-21.4dB
$\epsilon'_x = \epsilon'_z = 8$ $\epsilon'_y = 2$	-7.5dB
$\epsilon'_x = \epsilon'_z = 12$ $\epsilon'_y = 3$	-5.8dB
$\epsilon'_x = \epsilon'_z = 16$ $\epsilon'_y = 4$	-3.7dB

2. 2. C. iii. Impedance Matching Layer:

An impedance matching layer technique [55] can be a solution for reflectors where high mismatch reflection losses are obtained. We choose to introduce here a matching layer for configurations where losses are higher than $\Gamma > -10\text{dB}$ from table 2. 2.

It consists of a dielectric layer positioned at the aperture of the reflector with a thickness $t = \frac{\lambda_g}{4}$ as shown in fig. 2. 8.

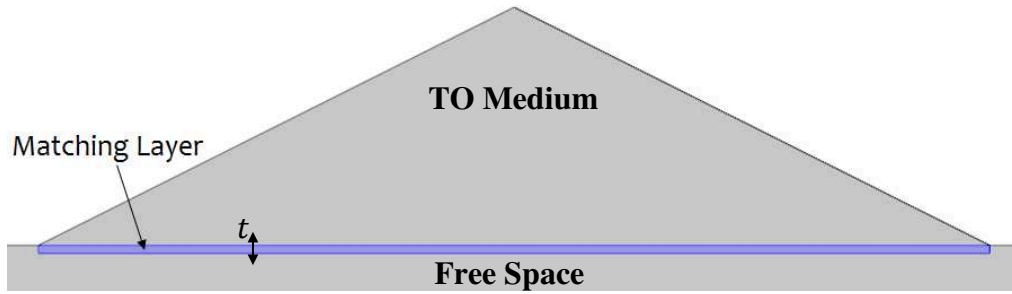


Figure. 2. 8. Illustration of a TO compressed reflector with an impedance matching layer.

It is well known that such a layer can be beneficial for a given EM device at a specific incidence only (at normal incidence only in our scenario). Furthermore, to match the domains between the compressed reflector and the surrounding free space, we use the following relative permittivity for the matching layer which is relevant to the x component only as follows:

$$\epsilon_a = \sqrt{\epsilon'_x} \quad (2-27)$$

Fig 2. 9. shows the nearfield results for the different reflector configurations using an impedance matching layer respectively at each of their apertures.

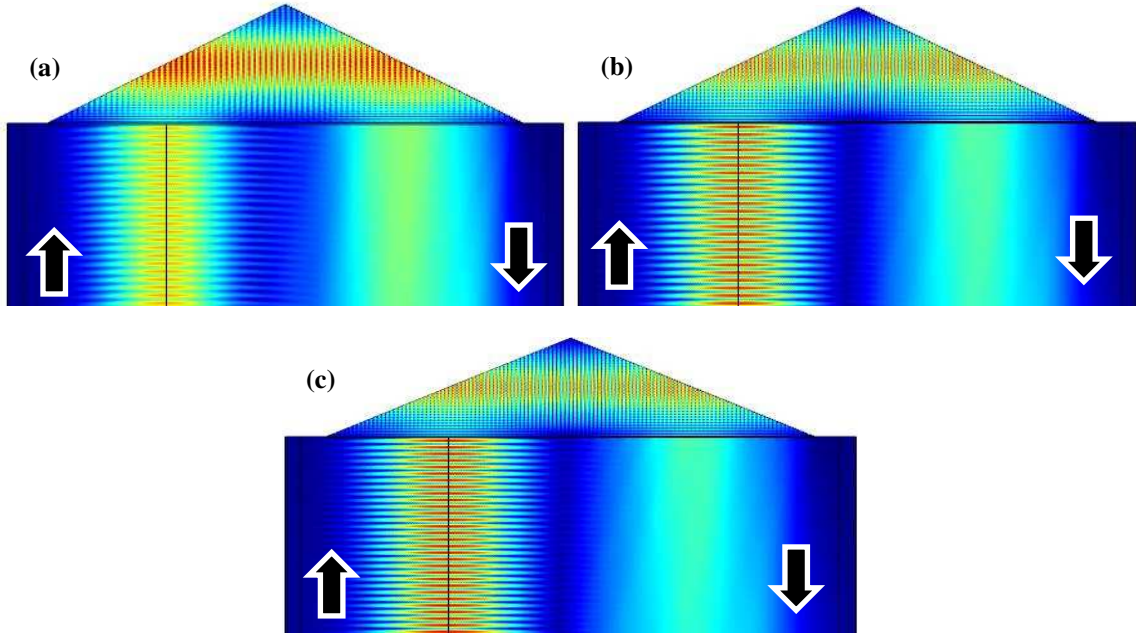


Figure 2. 9. Total complex E-field amplitudes (V/m) with $a=2b$ dimensions using (2-24) for $\epsilon'_x = \epsilon'_z = 8$; $\epsilon'_y = 2$; $\epsilon_a = 2.82$ (a), $\epsilon'_x = \epsilon'_z = 12$; $\epsilon'_y = 3$; $\epsilon_a = 3.46$ (b) and $\epsilon'_x = \epsilon'_z = 16$; $\epsilon'_y = 4$; $\epsilon_a = 4$ (c).

Fig 2. 9. shows clear improvement in lowering the levels of stationary waves for all configurations. Next, table 2. 3. details the improvement in reflection losses when compared to results obtained in table 2. 2.

Table 2. 3. Comparison of Reflection Losses for compressed reflectors with matching layers.

Reflection Coefficient Γ (dB)	
Compressed Reflector ($a = 2b$) using (2-24) with $\rho = 4$ and a matching layer using (2-27)	
$\epsilon'_x = \epsilon'_z = 8$ $\epsilon'_y = 2$	-17.5dB
$\epsilon'_x = \epsilon'_z = 12$ $\epsilon'_y = 3$	-10.5dB
$\epsilon'_x = \epsilon'_z = 16$ $\epsilon'_y = 4$	-10dB

While the impedance matching layer attenuates the loss levels for the configurations in table 2. 3., none of their results obtained surpass the $a = 2b$ reflector design for $\epsilon'_x = \epsilon'_z = 4$, $\epsilon'_y = 1$ from table 2. 1. (without any impedance matching). It is evident that this configuration presents a compromise between performance and loss levels. So this design is most suitable to be considered for further implementation.

2. 3. Implementation of the Anisotropic Material

2. 3. A. Double-layered System Design

A flexible way to realize the birefringent dielectrics is called Effective Medium Theory (EMT) [56, 57]. The EMT methodology suggests synthesizing the birefringence with a dielectric mixture. This medium can be constituted using different mixture topologies, from which we select the double layered system [56]. This choice is mainly justified by its relative simplicity, provided that its performance is equivalent to that of more complex dielectric configurations.

This system is constituted of 2 alternating isotropic dielectrics. In this representation, the layers are orthogonal to the y -axis, and the effective permittivity of the two layers is determined by the following set of equations [57]:

$$\begin{cases} \varepsilon'_z = \varepsilon'_x = \frac{\varepsilon_1 + d\varepsilon_2}{1 + d} \\ \varepsilon'_y = \frac{(1 + d)\varepsilon_1\varepsilon_2}{d\varepsilon_1 + \varepsilon_2} \end{cases} \quad (2-28)$$

where ε_1 and ε_2 represent the relative permittivity of dielectric 1 and 2, respectively and $d = \frac{d_1}{d_2}$ is the thickness ratio of the layers (with d_1 and d_2 very small compared to λ_0). A representation of the dielectric implementation is shown in fig. 2. 10.

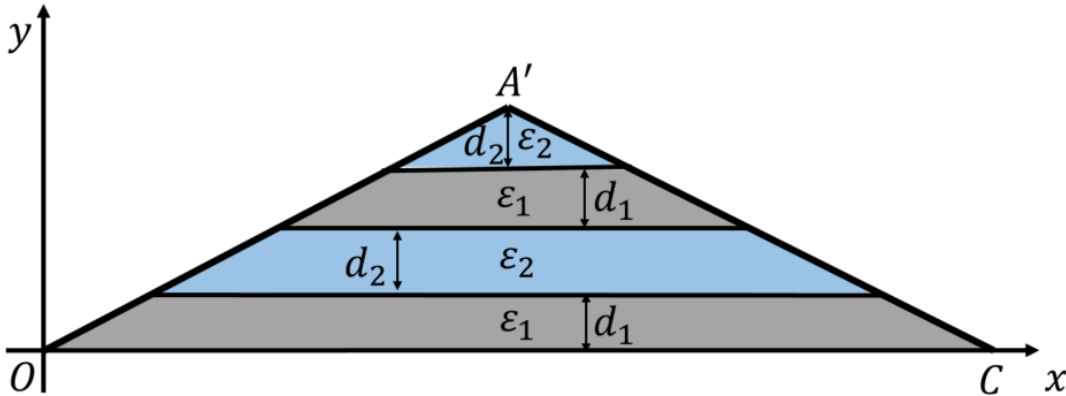


Figure. 2. 10. Representation of the dielectric layers distribution using EMT.

Careful considerations should take place in choosing the different values of the dielectric layers shown in fig. 2. 10. Using (2-28), the values of ε_1 and ε_2 can be obtained in function of their thickness ratio d , for different dimensions of the designed retrodirective reflector (a and b) and also for different material distributions ($\varepsilon'_x, \varepsilon'_y$). For instance, for $d = 1$ which means the two layers have the same thickness and for dimensions of $a = 2b$, it leads to $\varepsilon_1 = 7.464$ and $\varepsilon_2 = 0.5359$.

Fig 2. 11. shows different permittivity values ε_1 and ε_2 for the $a = 2b$ reflector in function of their thickness ratio d , for different material distributions ($\varepsilon'_x, \varepsilon'_y$) while keeping the same anisotropic factor $\rho = 4$ from eq. (2-26).

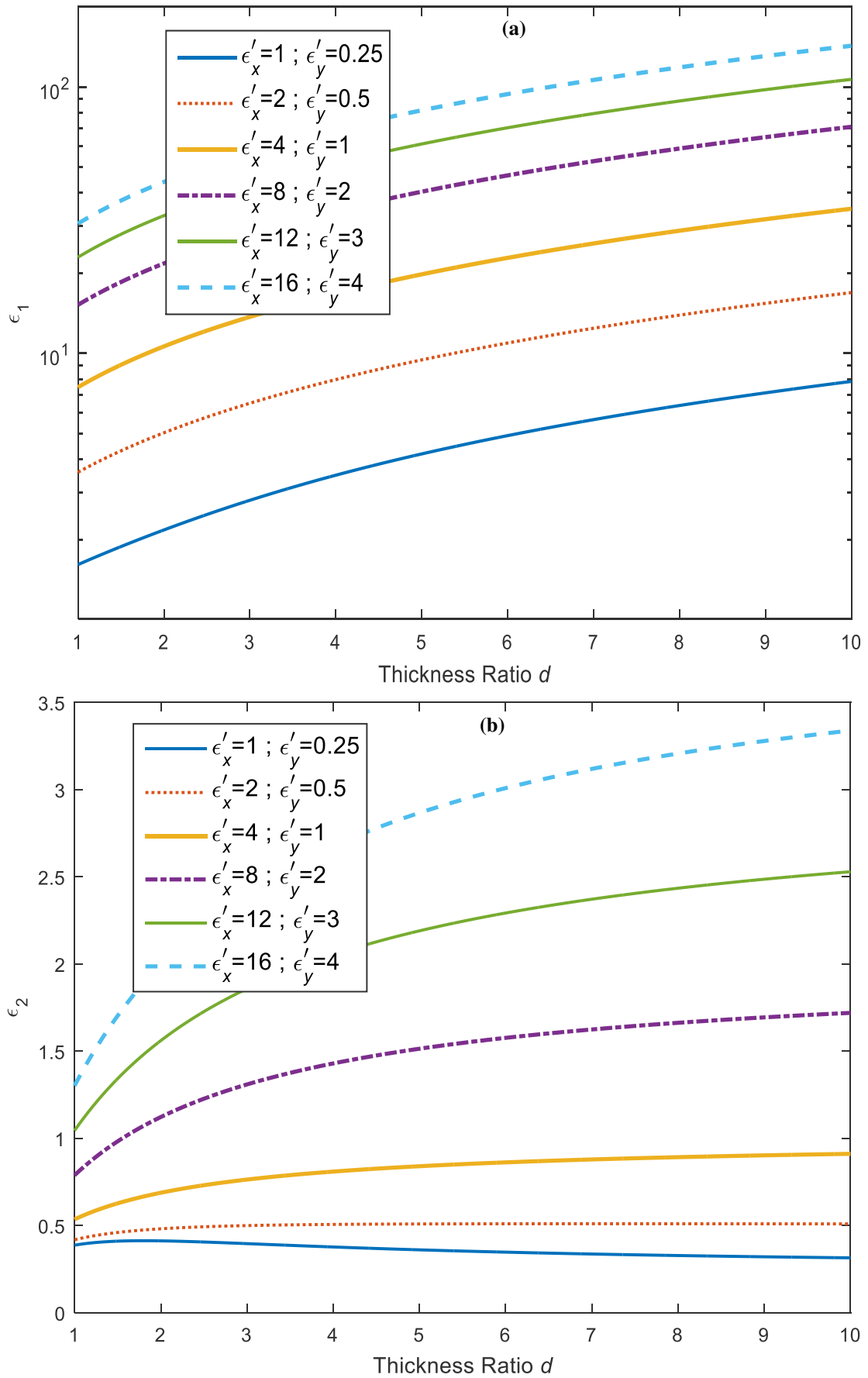


Figure 2.11. ϵ_1 (a) ϵ_2 (b) relative permittivity values in terms of thickness ratio d for different effective distributions ϵ'_x and ϵ'_y used within the compressed reflector ($a = 2b$).

To choose the most convenient layer permittivities and thicknesses, from fig. 2. 11., many methods can be applied. The first, consists of prioritizing the thickness of the layers over the permittivities of the dielectrics, with which $d \approx 1$ is chosen. Using this reasoning, the case $\varepsilon'_x = 4$ and $\varepsilon'_y = 1$ yields actually to an ε_2 much smaller than 1 so this may only be realized using specific exotic materials which eventually results in a very complex design.

Another approximation can also be considered. The permittivity value ε_2 approaches the value of 1 as the thickness ratio d increases. At $d = 10$, for the case $\varepsilon'_x = 4$ and $\varepsilon'_y = 1$, we can approximate ε_2 to 1 (instead of 0.9115) which is close to the free space value. Using these approximations to elevate the value of ε_2 actually ease the design's complexity even more.

Another case $\varepsilon'_x = 12$ and $\varepsilon'_y = 3$ can be considered as a better choice since it yields an ε_2 closest to 1 which renders the double layered system more realizable.

But, yet again both these cases may introduce high reflection losses over the interface since ε_1 value also increases greatly.

So in the next sections, we will choose $\varepsilon_1 = 7.464$ and $\varepsilon_2 = 0.5359$ for proof of concept.

2. 3. B. Validation of the Double layered system using EMT

In literature as in [56, 57], it is mentioned that for the double layered material to be close in value to its effective tensor $(\varepsilon'_x, \varepsilon'_y)$, the thicknesses d_1 and d_2 of the alternating layers should be very small compared to the wavelength of the propagating wave.

The goal of this study is to see the maximum layer thickness that can be used for the double layered system in order to effectively validate the case $\varepsilon'_x = 4$ and $\varepsilon'_y = 1$.

2. 3. B. i. Validation of the x -permittivity tensor component:

We start with validating the x tensor component $\varepsilon'_x = 4$ by comparing the double layered system (having $\varepsilon_1 = 7.464$ and $\varepsilon_2 = 0.5359$) overall reflection coefficient with that of a homogeneous isotropic dielectric layer. Fig. 2. 12. illustrates the two compared structures.

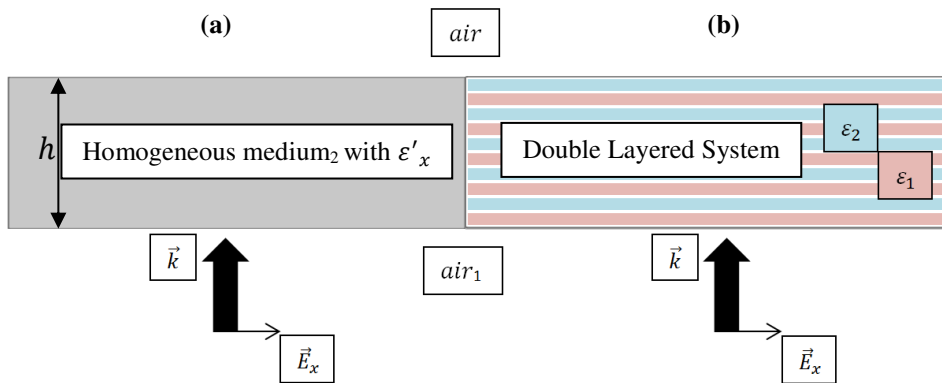


Figure. 2. 12. Comparative analytical study between homogeneous layer with $\varepsilon_x = 4$ (a) and double layered system with alternating $\varepsilon_1 = 7.464$ & $\varepsilon_2 = 0.5359$ (b).

The reflection coefficient of the homogeneous layer (englobed in air) in fig. 2. 12. (a) is given by the following equation:

$$\Gamma_{homogeneous} = \Gamma_{12} \left[\frac{1 - e^{-i2kh}}{1 - \Gamma_{12}^2 e^{-i2kh}} \right] \quad (2-29)$$

where Γ_{12} is the reflection coefficient at the interface between air and the dielectric medium, h is the layer's thickness and k is the wavenumber in the given medium.

On the other hand, the overall reflection coefficient Γ_o for the double layered system in fig. 2. 12. (b) can be calculated analytically as that of a multilayer structure as in [58]. It takes into account multiple reflections at all interfaces between consecutive layers. Here, the calculation is done using MATLAB. The layer's total thickness h is of course the same as the one of the homogeneous layer in Fig. 2. 12 (a). The calculation is repeated for different number of layers for the double-layered system.

The error rate between the overall reflection coefficient of the double layered system and that of the homogeneous dielectric medium is computed using eq. (2-30).

$$\text{Error rate(\%)} = \frac{\Gamma_o - \Gamma_{homogeneous}}{\Gamma_{homogeneous}} \times 100 \quad (2-30)$$

Fig. 2. 13. plots this error rate versus the number of layers per medium wavelength ($\lambda_{gx} = \frac{\lambda_0}{2}$ for $\epsilon'_x = 4$) for different values of h .

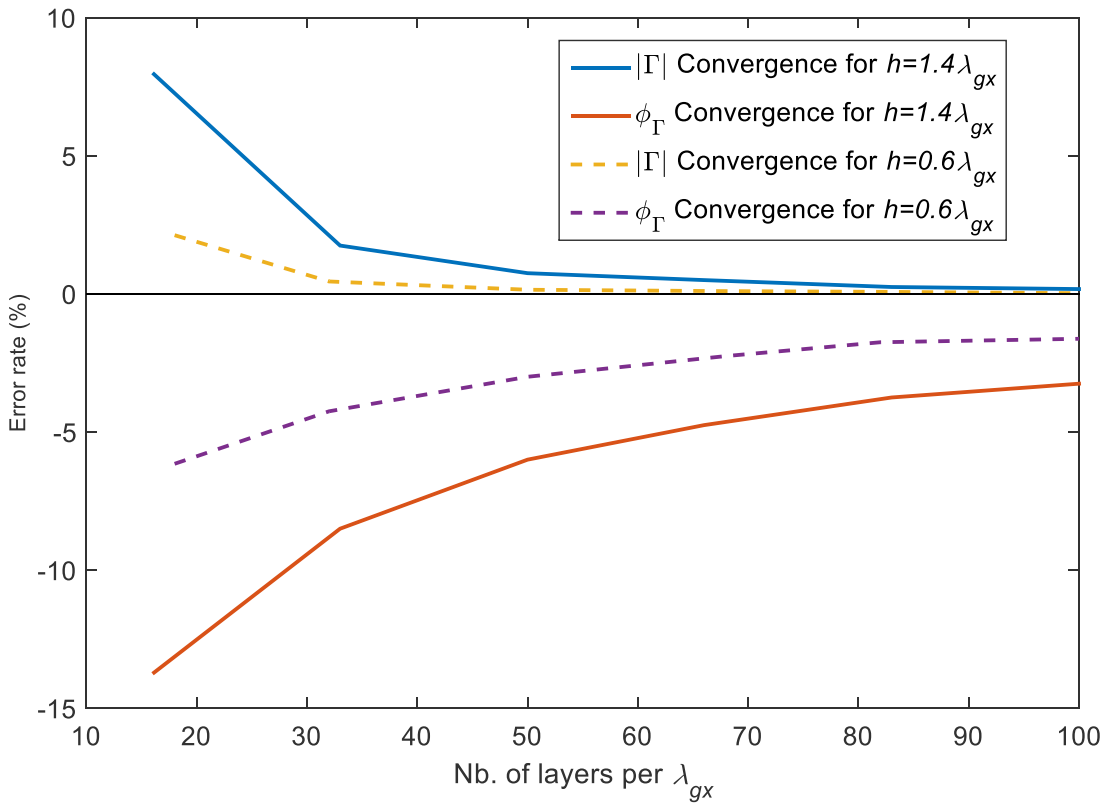


Figure. 2. 13. Error Rates (%) of the magnitude and phase components for the reflection coefficient in terms of the number of layers per guided wavelength.

Fig. 2. 13. shows, first, that all reflection coefficient factors (magnitude and phase) of the approximated double layered system converge to that of the homogeneous dielectric medium as the number of layers per wavelength increases. Second, the magnitude and phase do not converge with the same speed. For instance, at 100 layers/ λ_{gx} and for $h = 1.4\lambda_{gx}$, the error

rate for the phase component ϕ_Γ is at 1.6% while being at 0.1% for $|\Gamma|$. Third, as the total thickness h used for the layer increases the equivalent approximated double-layered system tends to converge faster to the intended permittivity value. This might be relevant to the fact that for the double layered system to be estimated properly, a bigger total thickness is needed with a bigger number of layers.

As an example, at $h = 0.6\lambda_{gx}$, and for an error rate lower than 5% for both the magnitude and phase of the reflection coefficient, 70 layers per medium wavelength are needed. It is important to note that this convergence study is only conducted with a homogeneous layer of $\epsilon'_x = 4$. If another material is used (with a different permittivity value) another convergence study might be needed.

2. 3. B. ii. Validation of the y permittivity tensor component:

The second part of the study is to insure the derived convergence rule in sub-section 2. 3. B. i. also applies to the longitudinal direction. More precisely, it must guarantee the equivalent permittivity $\epsilon'_y = 1$. For this particular direction, the only way available to assess the double layered system is using COMSOL simulations. In this direction of propagation ($+x$), the calculated ϵ'_y permittivity can be derived from the calculated wavelength of the wave propagating along x .

In these simulations, a double layered dielectric slab with a total thickness $h = 2.5\lambda_0$ is used. This system has the same alternating layers with $\epsilon_1 = 7.464$ and $\epsilon_2 = 0.5359$ from fig. 2. 13. A Gaussian beam with a beam width $w = 2.5\lambda_0$ and positioned at the center of the double layered system is used as shown by the big arrow in fig. 2. 14. Free space is used above and below the multi-layered medium with PML surrounding the whole domain. As previously, different simulations are conducted varying the number of layers that fills the same total thickness h .

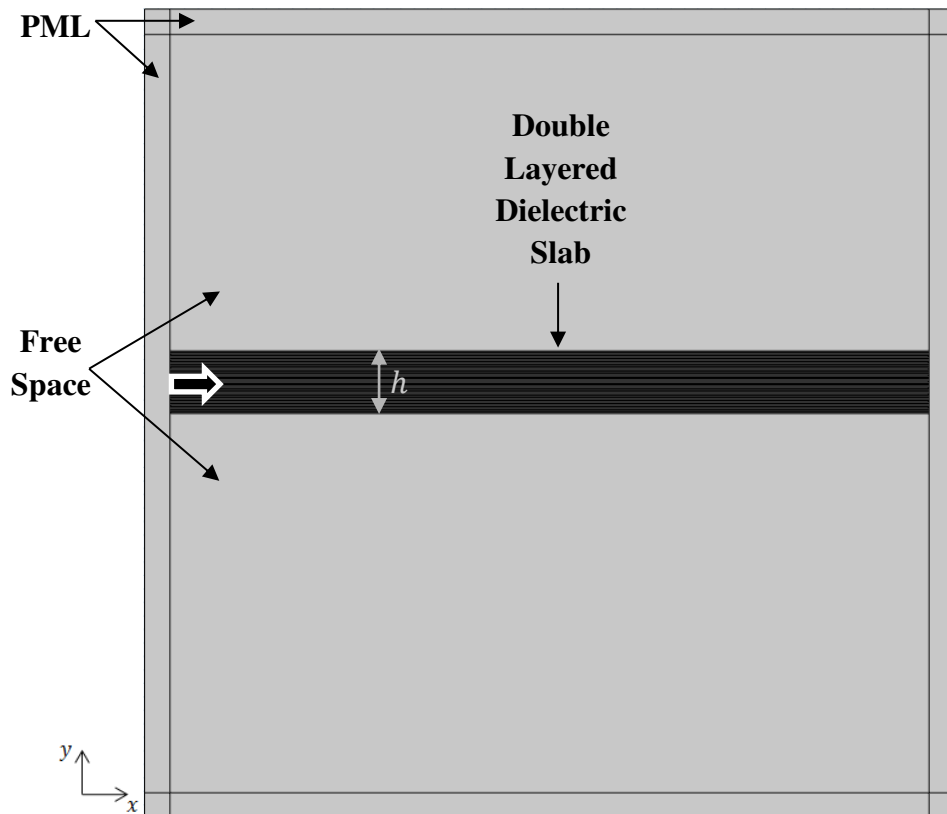


Figure. 2. 14. Illustration of the simulated configuration for the validation of the y permittivity tensor component.

Figure 2. 15. Shows the electric field distributions for a double layered system with different number of layers used within the same total thickness h .

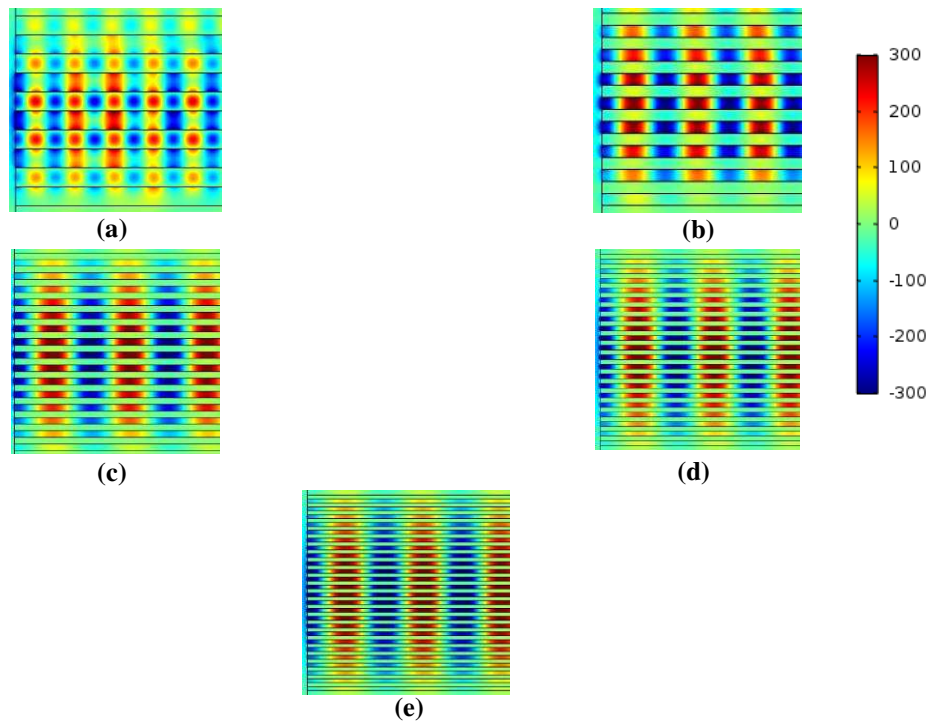


Figure. 2. 15. Close up at Electric Field Distributions in Time Domain (V/m) within a double layered system with E-field vectors perpendicular to the layers for $2\text{layers}/\lambda_{gx}$ (a) $4\text{ layers}/\lambda_{gx}$ (b) $6\text{ layers}/\lambda_{gx}$ (c) $8\text{ layers}/\lambda_{gx}$ (d) $10\text{ layers}/\lambda_{gx}$ (e).

The wavelengths $\lambda_{calculated}$ can be deduced from the Electric field distributions from fig. 2. 15. $\lambda_{calculated}$ is obtained by measuring the distance between two Electric field maxima at the center of the double layered dielectric slab , for the different simulated systems. It is then compared to the free space wavelength at the operating frequency $f = 8GHz$ using the following:

$$\epsilon_{calculated} = \left(\frac{\lambda_0}{\lambda_{calculated}} \right)^2 \quad (2-31)$$

Fig. 2. 16. Shows the resulting calculated permittivity convergence to the intended value of $\epsilon'_y = 1$ using eq. (2-31).

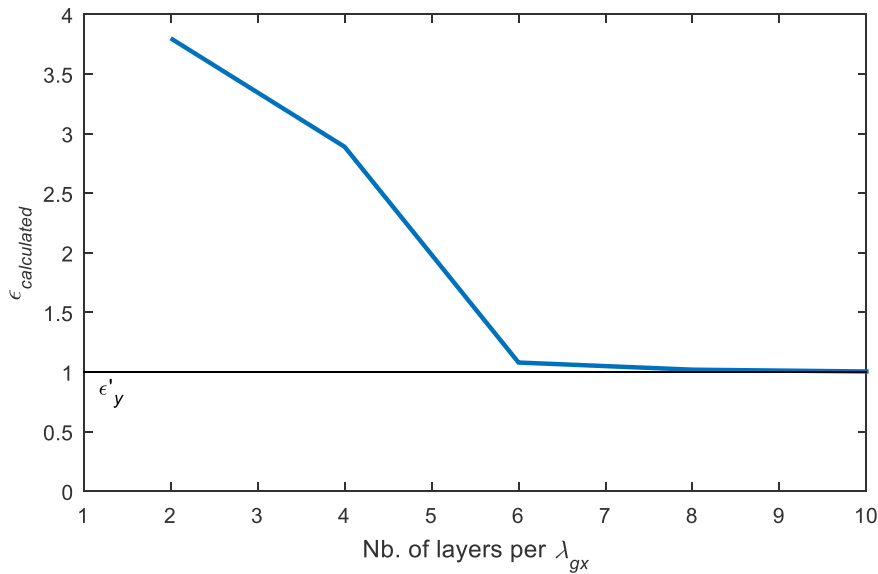


Figure. 2. 16. Convergence of the y-component of the permittivity obtained from the double layered system versus the number of layers.

From figure 2. 16., it is clear that 10 layers per wavelength are enough to approximate the y component of the anisotropic dielectric ($\epsilon'_y = 1$). Actually, when comparing this result with the one obtained before for $\epsilon'_x = 4$ in sub-section 2. 3. B. i., it is well obvious that the convergence for ϵ'_y is reached much faster. Using these convergence studies, an actual implementation of the double-layered system, for the corner reflector, can now be conducted using simulations.

2. 3. C. Simulation Results of the TO Compressed reflector using Double Layered system

Passing to applying the double layered system using EMT over the retrodirective reflector, the dimensions used are the following: for $d = 1$, $a = 2b = 10\lambda_0$.

According to the convergence study conducted in section (2. 3. B.), the density of layers should be 70 layers per medium wavelength λ_g for an error rate less than 5%.

Unfortunately, this would make COMSOL simulations impossible due to computation burdens. So, we are obliged to use smaller densities in simulations (for 10, 25 and 50 layers per λ_{gx}). The obtained results are shown in fig. 2. 17.

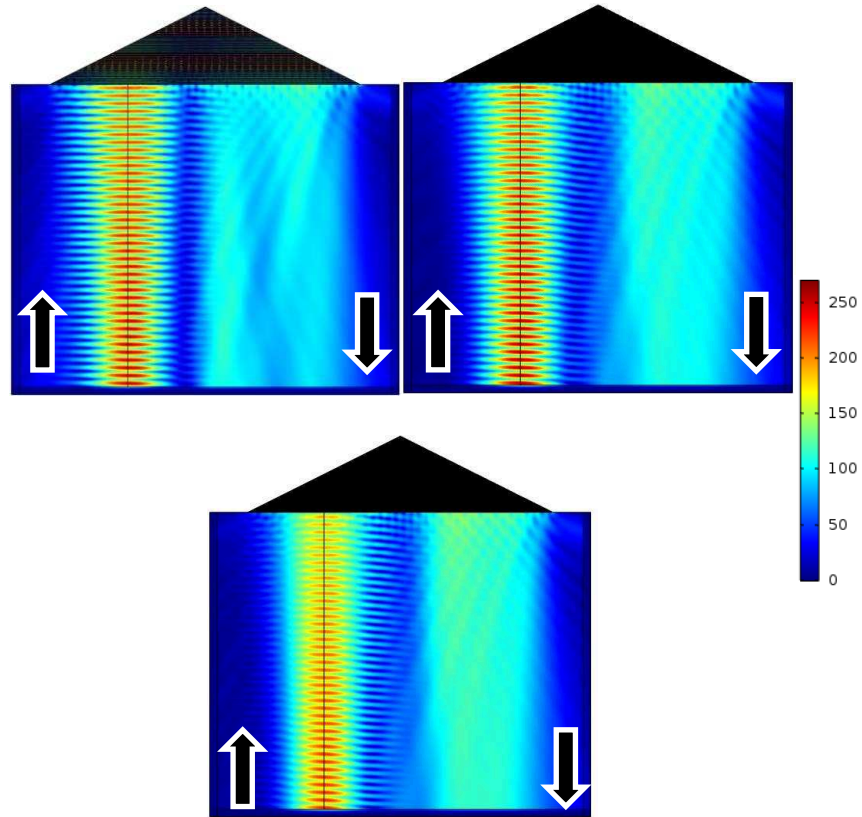


Figure. 2. 17. Total complex E-field amplitudes (V/m) for double-layered system with $\epsilon_1 = 7.464$ and $\epsilon_2 = 0.5359$ for (a) 10 layers/ λ_{gx} (total of 100 layers parallel to the x-axis) (b) 25 layers/ λ_{gx} (c) 50 layers/ λ_{gx} .

Although the convergence criterion is not totally met, the retrodirective behavior can be globally observed. Field amplitudes show that higher reflections at the reflector's interface are present when using a lower number of layers within the reflector. This can actually be associated with the convergence rule (fig. 2. 13) that showed higher error rates are obtained when a lower number of layers is used.

To better assess this point, table 2. 4. shows the reflection losses associated with each system simulated in fig 2. 17.

Table 2. 4. Comparison of Reflection Losses for different layer densities.

Compressed Reflector ($a = 2b$) Using Double Layered System with $\epsilon_1 = 7.464$ and $\epsilon_2 = 0.5359$	
Nb of layers/λ_{gx}	Reflection Coefficient Γ (dB)
10	-9.08
25	-10.62
50	-17.43

As shown from table 2. 4., reflection losses at the interface decrease in terms of the number of layers per λ_{gx} . The reflections for 50 layers per λ_{gx} is slightly decreased compared to that of the theoretical homogeneous medium (-17.43dB instead of -21.4dB from table 2. 1). This is also in relation with the fact that the convergence rule conducted in sub-section 2. 3. B. i. is not totally met.

2. 4. Conclusion

A new implementation of TO was proposed to design a dihedral reflector with low profile. It requires an anisotropic but homogeneous material to fill the reflector. The compressed reflector using TO shows that no physical laws of reflections are breached in the process along with modification of the field amplitudes upon reflection. Simulations with COMSOL Multiphysics confirm that the expected retrodirective behavior is perfectly achieved for normal incidence. Moreover, in the case of TM polarization, a non-magnetic material can be used at the expense of a slight reflection loss.

A practical implementation has been discussed comprising of a double-layered system. Convergence studies have demonstrated that the layer thickness, when exceeding $\lambda_g/70$, accurately approximates the anisotropic material and COMSOL simulations have shown promising results even for $\lambda_g/50$. While the double layered system accurately reproduces the classical reflector's performance along with an important compression of its dimensions, it clearly adds big limitations to the complexity of the design.

Different, already existing, material discretization methodologies can be exploited for such a technique. There may be more feasible materials for its implementation.

In the next chapter, we will investigate a possible solution to make the practical implementation simpler. The idea is to relax the constraints on the required TO medium. To do so, we propose to achieve the compression not only by engineering the medium itself but also the surface of the reflecting panels. More precisely, Surface Impedance Modulation (SIM) are implemented over the panels of the reflector in combination with TO in between.

Chapter 3 – Combining Transformation Optics and Surface Impedance Modulation for Retrodirective Reflectors

In the previous chapter, a more practical implementation of TO compression, compared to prior works, has been demonstrated for the dihedral reflector. Even though considered transformations lead to a homogeneous uniaxial anisotropic medium, it is still difficult to fabricate, particularly due to the high anisotropic factor it involves.

This chapter proposes a compression technique for the retrodirective reflector based on a combination of the TO approach and a phase gradient implemented with Surface Impedance Modulation (SIM).

Different compression techniques using SIM were proposed in [43, 44]. These studies are based on using two SIM panels assembled in a symmetrical (but not perpendicular) dihedral in free space. In those topologies, a convenient phase gradient is applied over the panels. Such a phase gradient can be implemented by modulating the surface impedance of the reflector's panels (SIM). It enables controlling the direction of the reflected wave within free space. So a given phase gradient applied over the reflector's panels may insure that the wave is redirected towards the source after a double-bounce reflection. However, on the down side, this mechanism is quite sensitive to the incident angle [45, 46] and the performance rapidly deteriorates as it increases. Furthermore, it is well known that introducing a phase gradient yields abnormal reflections over the surface [27]. In this chapter, we show there is some interest to use this phase gradient in combination with a TO compressed reflector.

The main goal of the proposed combination is to mitigate the TO limitations that were encountered in the previous chapter by relaxing the required anisotropic factor of the medium. On the other hand, the use of TO can also be advantageous to decrease the sensitivity of the SIM reflector. Typically, it would provide a unified way to control the reflected wave from an object by acting on both its surface and volume.

In the first section of this chapter, the phase gradient over an inclined panel is analytically calculated within an anisotropic medium. A parametric study that leads to compromise between TO and SIM parameters is conducted. In the second part, a potential implementation of SIM over a TO compressed reflector is presented and discussed as an intermediary physical model for simulations. In the third part, simulations for different intermediary situations are conducted along with different compressed reflector configurations. Last, in the fourth part, concluding remarks discuss the effects of the compression technique along with the impact of using the generalized phase gradient approach to the implementation of such an application.

This chapter relies on Full wave simulations over ANSYS® HFSS® to verify the theoretical relations.

3. 1. Theoretical Relations

A more general formalism of the SIM reflection within a TO medium has to be developed if we want to combine both methodologies to mitigate the disadvantages of one with the advantages of the other. The first step is to determine a common relation between the phase gradient needed over the reflector's panels and the tensor components of the filling medium.

3. 1. A. Analytical Calculation of the Phase Gradient within Anisotropic Media for one inclined Panel

3. 1. A. i. Configuration Parameters

The starting configuration, that represents one panel of the reflector within anisotropic media, is depicted in fig. 3. 1.

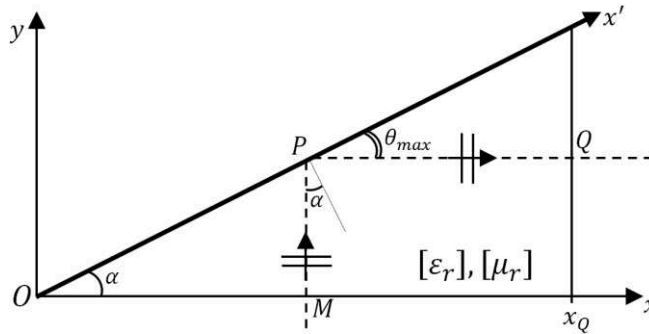


Figure 3. 1. General configuration with one inclined panel in an anisotropic medium.

A x -polarized (TM) incident plane wave propagates along $+y$ and hits the reflective panel that lies along the Ox' axis. The inclination angle of the panel with respect to the horizontal x -axis is noted as α and is directly related to the compression factor of the reflector (with $\alpha = 45^\circ$ for the classical dihedral reflector). Geometrically, the incidence angle over the reflective panel is equivalent to α with θ_{max} being the reflection angle with respect to the panel's axis.

The whole domain is considered filled with a homogeneous anisotropic medium with the following relative material parameters:

$$[\epsilon_r] = \begin{bmatrix} \epsilon_x & 0 & 0 \\ 0 & \epsilon_y & 0 \\ 0 & 0 & \epsilon_z \end{bmatrix} \text{ and } [\mu_r] = \begin{bmatrix} \mu_x & 0 & 0 \\ 0 & \mu_y & 0 \\ 0 & 0 & \mu_z \end{bmatrix} \quad (3-1)$$

The respective wavenumbers and impedances are given, depending on the tensor components of the anisotropic medium, as follows:

$$k_x = k_0 \sqrt{\epsilon_y \mu_z} \text{ and } \eta_x = \eta_0 / \sqrt{\mu_z / \epsilon_y} \quad (3-2)$$

for a plane wave linearly polarized along y and propagating along x and

$$k_y = k_0 \sqrt{\epsilon_x \mu_z} \text{ and } \eta_y = \eta_0 / \sqrt{\mu_z / \epsilon_x} \quad (3-3)$$

for a plane wave linearly polarized along x and propagating along y .

3. 1. A. ii. Generalized Phase Gradient Derivation

We now derive the required phase gradient over the panel in order to reflect the incident plane wave in the $+x$ direction (for $\theta_{max} = \alpha$), since this direction is required to conserve the retrodirectivity performance of the reflector later on.

Let's consider the phase of the incident wave at any point $M(x, 0)$ located on the Ox axis is zero $\phi_M = 0$. At point $P(x, x \tan \alpha)$ over the panel, the phase becomes:

$$\phi_P(x) = -k_y x \tan \alpha \quad (3-4)$$

Now assuming the reflection on the panel generates an additional phase $\phi_\Gamma(x')$ and enforcing propagation along $+x$ for the reflected wave, the phase at point Q is:

$$\phi_Q(x) = -k_y x \tan \alpha - k_x(x_Q - x) + \phi_\Gamma(x') \quad (3-5)$$

where $x' = x/\cos \alpha$ and x_Q is an arbitrary x -coordinate for Q . In order to obtain a reflected wave propagating as a plane wave, this phase must not be dependent on x . Consequently, the additional phase over the panel is assumed as:

$$\phi_\Gamma(x') = k_y x' \sin \alpha - k_x x' \cos \alpha + \phi_0 \quad (3-6)$$

where ϕ_0 is an arbitrary phase constant.

It is important to note that (3-6) defines a linear phase deviation: as in [6], it suggests a constant phase gradient is required on the reflecting surface to control the direction of the reflected wave. Using (3-2) and (3-3), it can be shown the phase gradient we obtain here is related to the tensor components of the filling medium and the inclination angle as follows:

$$\frac{d\phi_\Gamma(x')}{dx'} = k_0 \sqrt{\mu_z} (\sqrt{\varepsilon_x} \sin \alpha - \sqrt{\varepsilon_y} \cos \alpha) \quad (3-7)$$

3. 1. A. iii. Particular Cases of the Generalized Phase Gradient:

Two different particular cases can be deduced from this expression in (3-7) for the required phase gradient:

- If $\sqrt{\varepsilon_x/\varepsilon_y} = \cot \alpha$, it is found that:

$$\frac{d\phi_\Gamma(x')}{dx'} = 0 \quad (3-8)$$

In this case, no phase gradient is needed on the panel and a simple metallic plate is thus sufficient. All the phase compensation at the point Q is provided by the sole anisotropic medium. This corresponds to the situation where compression is obtained by TO only, as demonstrated in chapter 2.

- If $k_y = k_x = k_0$ which means the considered medium is free space, (3-7) reduces to:

$$\frac{d\phi_{\Gamma}(x')}{dx'} = k_0(\sin\alpha - \cos\alpha) \quad (3-9)$$

In this case, only the phase gradient in (3-9) over the panel is used to compensate for the phase differences at Q . This corresponds to the situation where compression is obtained by SIM only, as in [6].

3. 1. B. Parametric optimization between Anisotropic Factor and Phase Gradient

Particular cases, discussed in the previous section, correspond to extreme situations where only one approach (either TO or SIM) is used to compress the reflector. But actually, (3-7) demonstrates the possibility to combine both and suggests that a compromise can be achieved. This trade-off has to be made between the anisotropic factor $\rho = \frac{\varepsilon_x}{\varepsilon_y} = \frac{\mu_x}{\mu_y}$ of the medium, used in chapter 2 as a degree of freedom, and the phase gradient $(d\phi_{\Gamma}(x')/dx')$ over the panels.

In the following, we consider a similar case for the TO medium to what was discussed in the previous chapter. Such medium is anisotropic and homogeneous with uniaxial relative constitutive parameters and we note:

$$[\varepsilon_r] = [\mu_r] = \begin{bmatrix} c & 0 & 0 \\ 0 & \frac{c}{\rho} & 0 \\ 0 & 0 & c \end{bmatrix} \quad (3-10)$$

with c being the TO distribution constant.

Fig. 3. 2. displays the required phase gradient from (3-7) versus the anisotropic factor with $c = 2$. It has been obtained by inserting the tensor components from (3-10) into (3-7) for different values of the inclination angle α . The latter corresponds to different compression or expansion rates of the reflector's dimensions (cf. fig. 2. 2.).

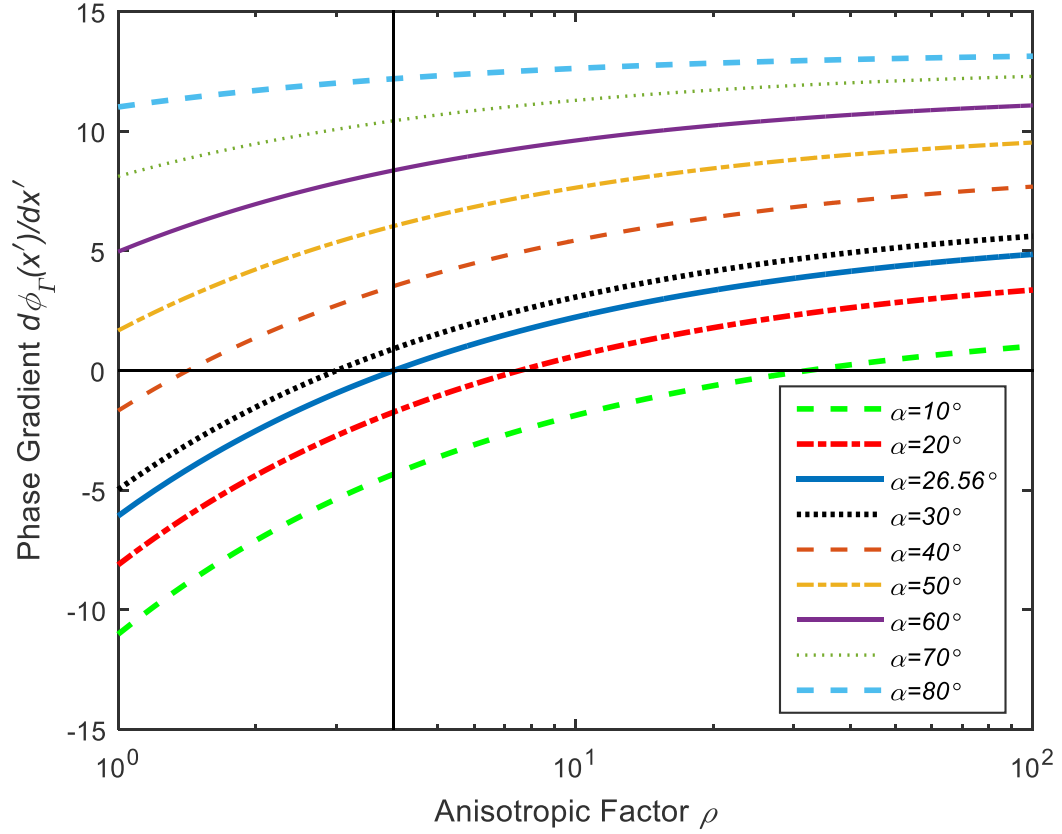


Figure 3. 2. Phase gradient versus the anisotropic factor for compressed reflector with different inclination angles α .

It clearly shows that for each compression rate, the obtained phase gradient varies with the anisotropic factor. On the other hand, no phase gradient is needed ($d\phi_{\Gamma}(x')/dx' = 0$) if the anisotropic factor is set to an appropriate value that compensates the transformation of the reflector. As an example, the case where $\alpha=26.56^{\circ}$ and $\rho = 4$ (blue uniform line in Fig. 3. 2) is one of the cases discussed in the previous chapter. Note that small α corresponds to higher compressions of the corner reflector and logically leads to more stringent constraints on both the phase gradient and anisotropic factor.

Finally, it must be highlighted that the case where the phase gradient is positive ($d\phi_{\Gamma}(x')/dx' > 0$) are useless. It corresponds to situations where the compression brought by the anisotropic factor is too large (for cases where $\alpha < 45^{\circ}$) and has to be compensated by a decompression reaction on the panels. It may even correspond to situations where the dimensions of the reflectors used are intentionally greater than that of the classical one (for cases where $\alpha > 45^{\circ}$) and then again a positive phase gradient can be used for compensation.

At this stage, we remind that we intend to relax the anisotropic factor of the medium for a compressed reflector with $\alpha=26.56^{\circ}$. So the region of importance for our case, from fig. 3. 2., is for $d\phi_{\Gamma}(x')/dx' < 0$ and $\rho < 4$.

3.2. Implementing Surface Impedance Modulation (SIM)

In the previous section, we demonstrated that a phase gradient is needed over the panels of a compressed reflector for the impinging wave to be reflected in the desired direction.

It is important to note that SIM can be practically implemented using a discretization technique over the panels. We present, in this section, a compressed reflector with discretized SIM model over its panels along with a TO medium from eq. (3-10) filling its domain. The general configuration is depicted in fig. 3. 3.

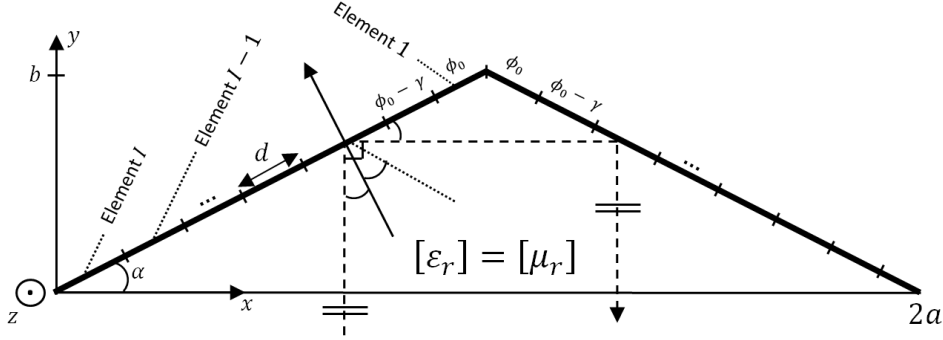


Figure 3. 3. General configuration of a compressed reflector with a combination of discretized SIM over the panels and TO domain filling the reflector's domain.

In the numerical implementation, each panel is divided into I elements with dimension d and a phase shift is applied on element i as:

$$\phi_{\Gamma_i} = \phi_0 - (i - 1)\gamma \quad (3-11)$$

with γ being the phase increment between consecutive elements:

$$\gamma = \frac{d\phi_{\Gamma}(x')}{dx'} d \quad (3-12)$$

For the sake of simplicity and with no loss of generality, the phase shift on each element is set by tuning its surface impedance Z_{si} to the appropriate value. Assuming TM polarization (E-field along x -axis), the reflection coefficient on element i is:

$$\Gamma_i = \frac{\frac{Z_{si}}{Z_{TM}} - 1}{\frac{Z_{si}}{Z_{TM}} + 1} \quad (3-13)$$

where $Z_{TM} = \eta_0 \cos \alpha$, and α stands for the incident angle on the panel (equal to the inclination angle desired in this configuration).

It is important to mention also that SIM distribution used over both panels of the reflector is symmetrical with respect to the central plane parallel to the y -axis as shown in figure 3. 3. This is mainly due to the complementary incident angles over the panels. For example, for a 30° incident angle on the left panel, the incidence over the right one is 60° .

Now, enforcing each element's surface impedance as purely reactive ($Z_{si} = jX_{si}$) so that all the power is reflected from the panel ($|\Gamma| = 1$), it comes as:

$$X_{si} = \frac{Z_{TM}}{\tan\left(\frac{\phi_{\Gamma i}}{2}\right)} \quad (3-14)$$

Finally, by combining (3-11) and (3-14), the required surface impedance on each element for its given phase gradient can be obtained.

3.3. Numerical Results

In this section, SIM are achieved by modulating the surface impedance of a reflecting sheet. As a first step, the problem of modelling a sheet with prescribed surface impedance in a full-wave solver is addressed. The goal is to properly implement SIM over a panel at any incidence and reflection. Last, simulation results are given for a compressed retrodirective reflector designed by combining a TO filling medium and SIM over the reflector's panels.

3.3.A. Validation of a Prescribed Surface Impedance

The purpose here is to verify the reflection properties of prescribed surface impedance over a planar sheet. A normally incident plane wave, within free space, impinges on the planar sheet. Three different configurations are simulated using HFSS. As discussed in section 3.2., the surface impedance of interest is considered to be purely reactive with $Z_s = jX_s$. The planar sheet's reactance is also chosen to vary between $-5000\Omega \leq X_s \leq +5000\Omega$.

The results awaited that should be validated with the simulated configurations are the following magnitude $|\Gamma|$ and phase ϕ_Γ of the reflection coefficient enforced over the sheet:

$$|\Gamma| = 1 \quad (3-15)$$

$$\text{and } \phi_\Gamma = 2 \tan^{-1}\left(\frac{\eta_0}{X_s}\right) \quad (3-16)$$

Equation (3-16) being the reciprocal relation of (3-14).

In the first configuration, the planar sheet is placed in the middle of a TEM waveguide as illustrated in fig. 3.4. The de-embedding is clearly chosen at the plane of the prescribed impedance sheet.

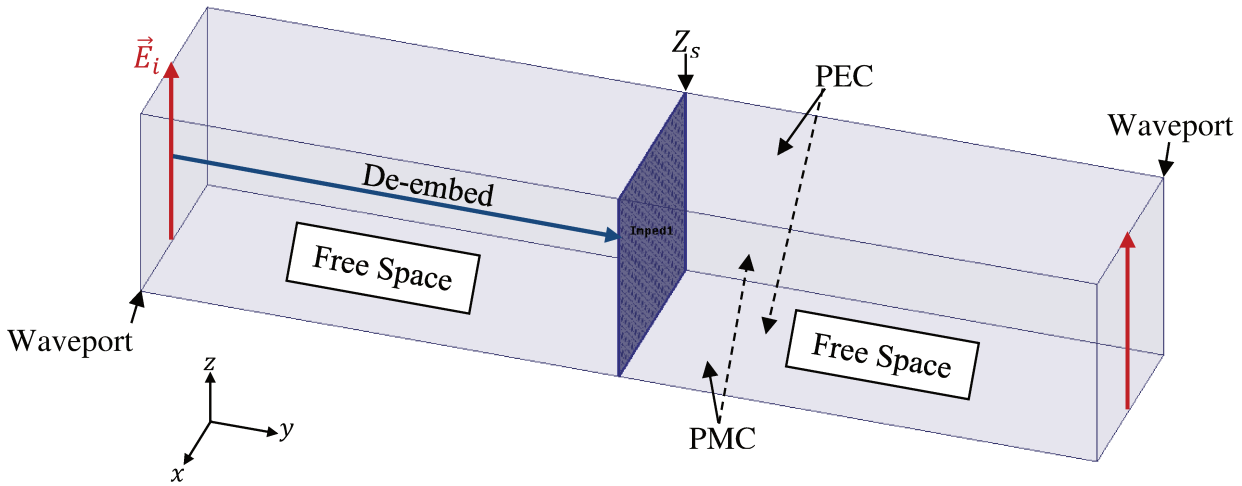


Figure 3. 4. HFSS simulation of a prescribed surface impedance (Z_s) sheet positioned at the middle of a TEM waveguide.

Fig. 3. 5. compares the magnitude and phase of the simulated configuration with the awaited results for a pure reactive impedance sheet.

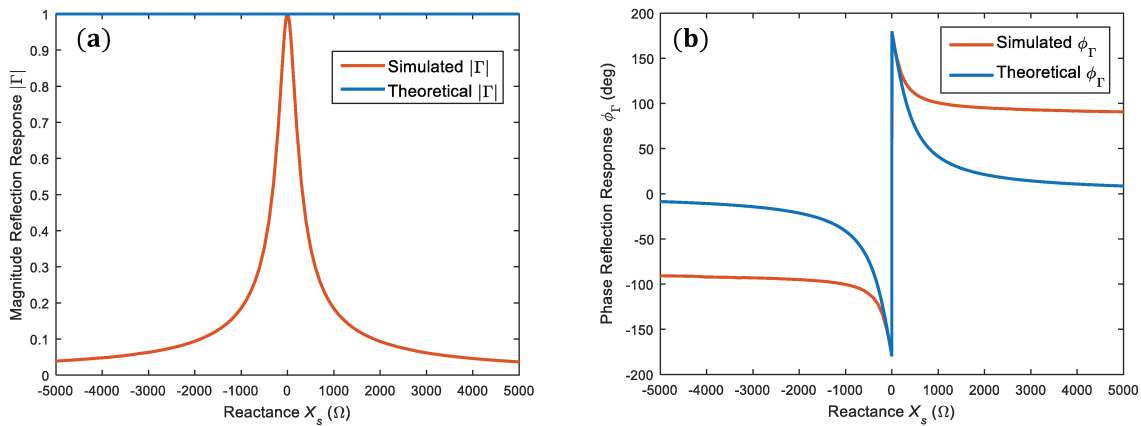


Figure 3. 5. Magnitude (a) and phase (b) of the reflection coefficient as function of the reactance X_s .

Fig. 3. 5. shows that the reflection response obtained from such configuration is not equivalent to the awaited response from eqs. (3-12) and (3-13). In consequence, it is proven that this type of configuration does not yield valid results for $Z_s = jX_s$ and thus cannot be used for our purposes.

The general idea is to back the surface impedance condition with a PEC in order to obtain the awaited reflection response. So we pass on to the two other possible configurations. The planar sheet can be placed either at the boundary of a TEM waveguide or at the interface of a volumetric PEC medium as shown in fig. 3. 6.

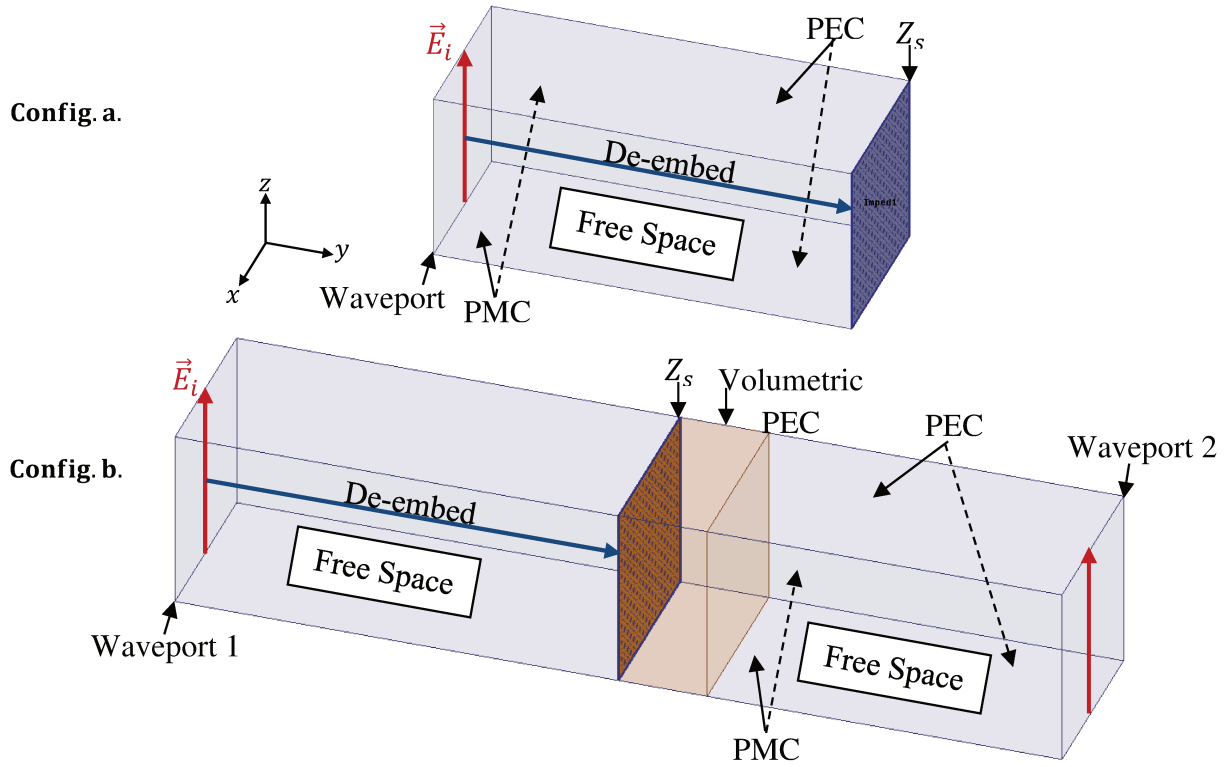


Figure 3. 6. HFSS configuration of prescribed Z_s at the boundary of a TEM waveguide (config. a.) and at the interface of a volumetric PEC positioned within the TEM waveguide (config. b.).

Fig. 3. 6. compares the magnitude and phase of both simulated configs. (a and b) with their theoretical counterpart for the pure reactive impedance sheet.

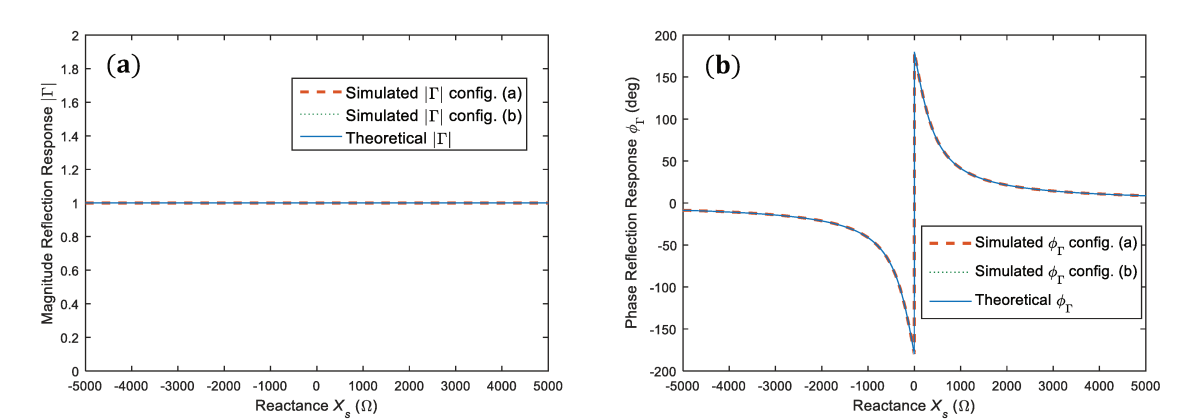


Figure 3. 7. Magnitude (a) and phase (b) components of the reflection coefficient for the different simulated configs in function of X_s .

It is clear that fig. 3. 7. show both configurations are equivalent to the awaited theoretical reflection coefficient (defined by eqs. (3-15) and (3-16)). This means that, in order to accurately simulate reactive surface impedance sheets with HFSS, these planes must be placed either at the boundary of the domain or at the surface of a PEC volume.

3. 3. B. Verification of SIM array simulations with HFSS

In this section, the performance of an array of SIM elements within free space is discussed. Such an array is constituted of rectangular elements that implement the impedance

distribution respecting the phase requirements (already determined in section 3. 2. B) for different configurations. Each configuration has predetermined incidence angle α and reflection angle θ_{max} as defined in fig. 3. 8.

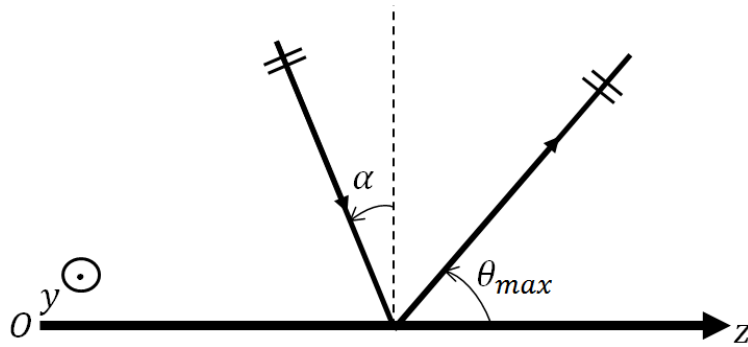


Figure 3. 8. Illustration of the chosen conventions for one SIM panel.

Since we need to validate a SIM panel's performance for any incidence and reflection in free space, the phase gradient, to be used, is reformulated accordingly to fig. 3. 8. as follows:

$$\frac{d\phi_{\Gamma}(z)}{dz} = k_0(\cos\theta_{max} - \sin\alpha) \quad (3-17)$$

In order to successfully simulate the elements (as demonstrated in 3. 3. A.), planar sheets with prescribed impedances are positioned at the bottom of the simulation domain with perfectly matched layers (PML) surrounding the free space domain (highlighted in light blue) as shown in fig 3. 9. For better visualization of the simulated domain a xz plane visibility cut has been performed.

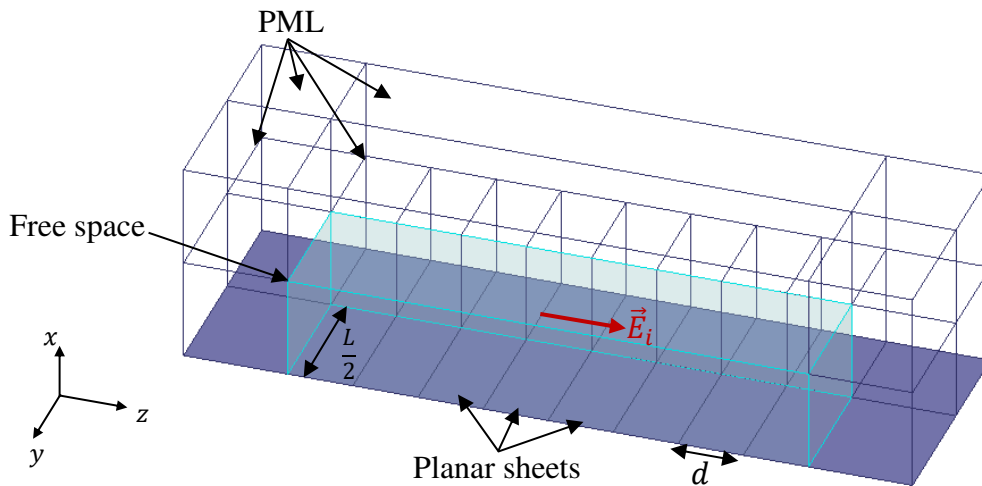


Figure 3. 9. Simulated configuration (xz plane visibility cut) for a normally incident plane wave over an array of planar sheets with prescribed impedances.

Choosing $I = 8$ elements with a normally incident plane wave at $f = 8\text{GHz}$ ($\alpha = 0^\circ$), $d = \frac{\lambda_0}{4}$, $L = \lambda_0$ and choosing $\theta_{max} = 80^\circ, 70^\circ$ and 60° , the prescribed surface impedances using eqs. (3-14) and (3-17) are given in fig. 3. 10.

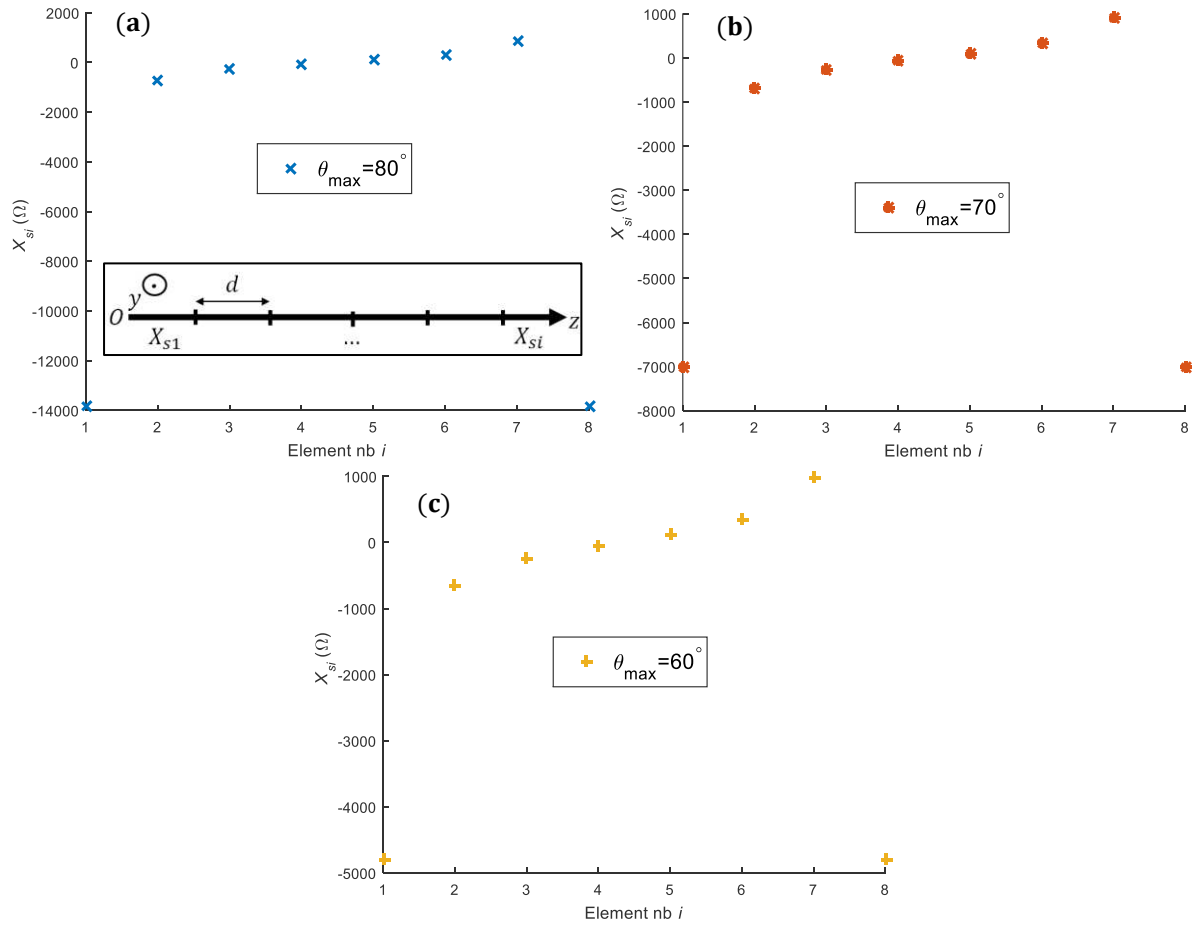


Figure 3. 10. Prescribed surface impedances used on each planar sheet of the simulated SIM panel for different normal incidence configurations with $\alpha = 0^\circ$ and $\theta_{max} = 80^\circ$ (a), $\theta_{max} = 70^\circ$ (b) and $\theta_{max} = 60^\circ$ (c).

Normalized far field E-plane cuts (along xz plane) are displayed in fig. 3. 11. They show the direction of the main lobe that can be validated with the intended reflection angle θ_{max} . For further verification the far field results are compared with their normalized array factor cuts for theoretical linear arrays. Eq. (3-11) was used to compute phase shifts between the adjacent elements of the theoretical arrays. The other same simulation parameters are also used for the theoretical arrays for equivalence ($d = \frac{\lambda_0}{4}$ and $I = 8$ elements).

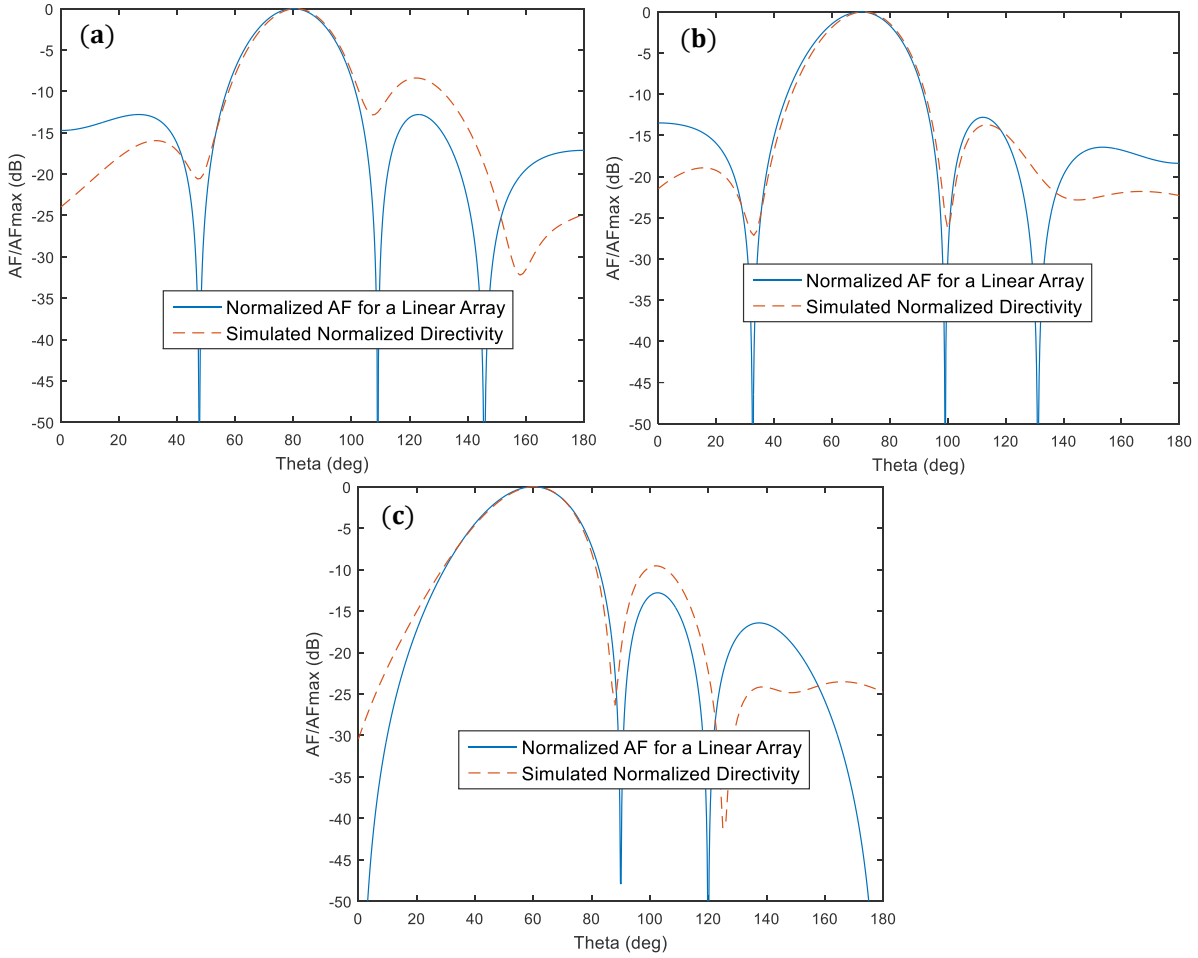


Figure 3. 11. Comparison between the normalized array factor of a phased linear array and the simulated normalized directivity of the SIM panel with prescribed impedance for $\theta_{max} = 80^\circ$ (a), $\theta_{max} = 70^\circ$ (b) and $\theta_{max} = 60^\circ$ (c).

It is demonstrated through fig. 3. 11. (a, b and c), that the main lobe is accurately obtained at the desired directions θ_{max} for the simulated configurations. Negligible differences persist between the simulated configurations and the array factors of their equivalent linear arrays. These differences are more apparent in the side lobe levels (in unwanted directions) due to many other contributing factors. One of the reasons might be in relation with the fact that the theoretical configuration doesn't take into account diffractions between elements. Second, each element used in the array factor approach is punctual while in the SIM model, it is rectangular planar sheet with a given surface and constant impedance.

Passing on to oblique incidence with configurations at $\alpha = 10^\circ, 20^\circ$ and 26.56° and $\theta_{max} = 70^\circ, 50^\circ$ and 26.56° , the corresponding prescribed surface reactances for the planar sheet arrays are plotted in fig. 3. 12.

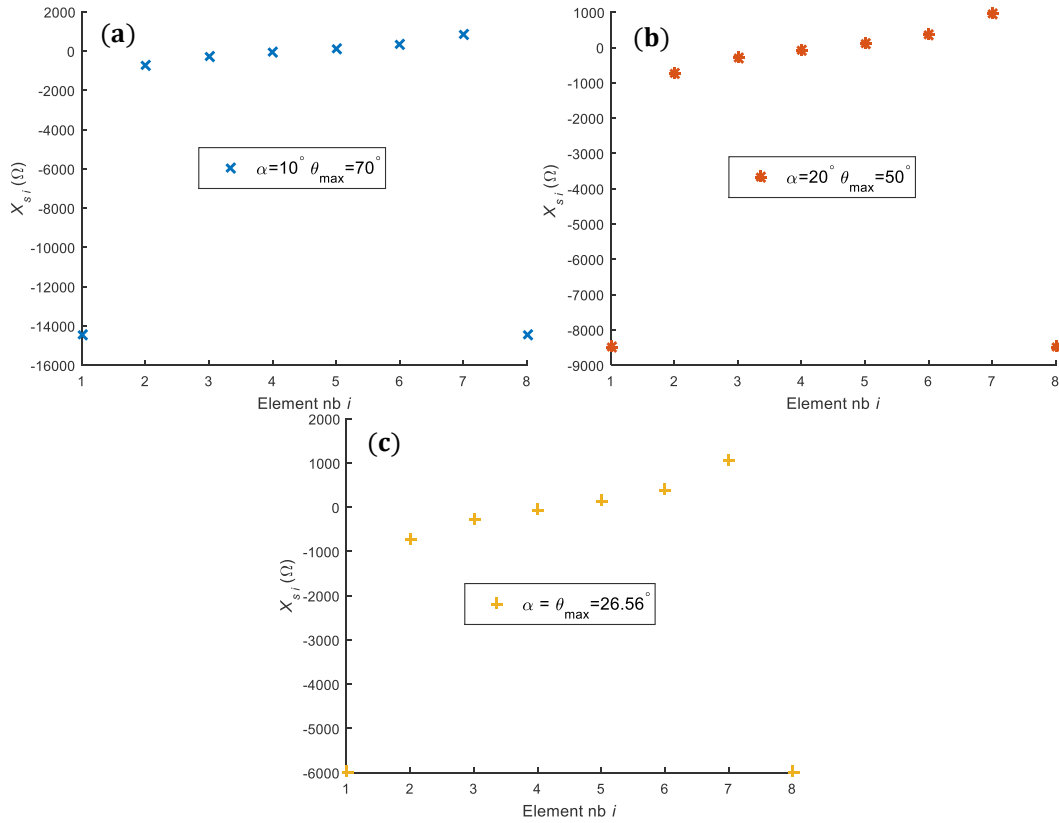


Figure 3.12. Prescribed surface impedances for each planar sheet at oblique incidence configurations for $\alpha = 10^\circ$ and $\theta_{max} = 70^\circ$ (a), $\alpha = 20^\circ$ and $\theta_{max} = 50^\circ$ (b) and $\alpha = \theta_{max} = 26.56^\circ$ (c).

The comparative results with array factors of phased arrays are presented in fig. 3.13.

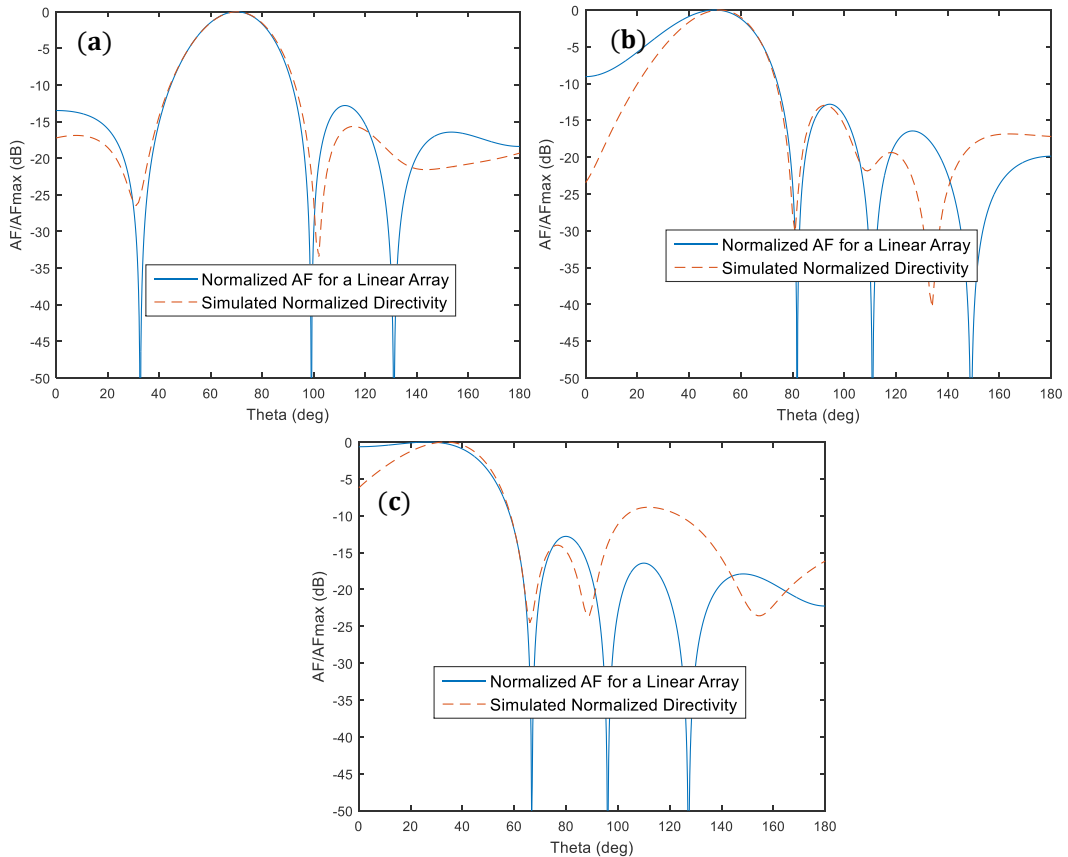


Figure 3.13. Comparison between normalized array factor of an array with the simulated directivity of planar sheets for $\alpha = 10^\circ$ and $\theta_{max} = 70^\circ$ (a), $\alpha = 20^\circ$ and $\theta_{max} = 50^\circ$ (b) and $\alpha = \theta_{max} = 26.56^\circ$ (c).

Fig. 3. 13. (a, b and c) shows also that main lobe directions are well consistent with the desired reflections at θ_{max} . We remind here that the configuration of interest for the compressed reflector scenario, later on, is for $\alpha = \theta_{max} = 26.56^\circ$ presented in fig. 3. 13. (c).

3. 3. C. Simulation Settings for a Compressed Reflector using a combination of TO and SIM

We pass directly to the validation of the total compressed reflector using a combination of TO and SIM. We consider the following parameters (fig. 3. 14.): $f = 8GHz$ with $\alpha = 26.56^\circ$, $a = 10\lambda_0$, $b = 5\lambda_0$ and height $h = 10\lambda_0$ along the z-axis. Each panel is divided into $I = 44$ SIM elements with $d = \lambda_0/4$ and $L = h$. SIM elements are backed by a volumetric PEC medium (highlighted in orange in fig. 3. 14.) for proper characterization (as determined in section 3. 3. A.). The anisotropic medium from eq. (3-10) fills the inside of the reflector domain (highlighted in green). The x-tensor component of the anisotropic medium is in line with the aperture of the reflector configuration. These parameters were carefully chosen so that the discretized phase gradient provides a precise enough approximation of (3-7) while maintaining realistic computational resources for the simulations within HFSS.

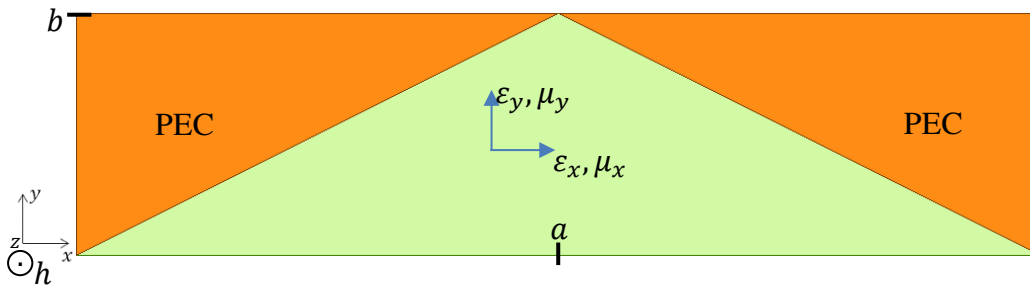


Figure 3. 14. Theoretical anisotropic medium (highlighted in green) filling the Compressed Reflector's domain (Volumetric PEC highlighted in orange).

As detailed in Table 3. 1., different arrangements are simulated using combinations of the anisotropic factor ρ and phase increment γ between adjacent SIM elements (as discussed in sections 3. 1. B. and 3. 2.)

Table 3. 1. Parameters used for simulated Configurations.

Reflector Configurations	Config. 1	Config. 2	Config. 3	Config. 4
Dimensions a & b	$a = 2b$			
Distribution Constant c	2			
Anisotropic Factor ρ	1	2	3	4
Phase Increment γ (deg)	-40.26°	-33.36°	-12.47°	0°

From table 3. 1., configuration 1 corresponds to the extreme situation where the compression is only due to the modulation of the surface impedance on the panels (free space with no filling medium) while configuration 4 is the opposite with only TO (no modulated surface impedances on the panels). Configurations 2 and 3 are intermediary cases combining both methodologies.

3.3.D. Simulation Results for the TO/SIM Compressed Reflectors

Simulation results for the configurations, defined in table 3. 1., are presented in this section. An incident Gaussian beam, with TM polarization (E-field along x axis), is applied on the left panel with a beam of width $3\lambda_0$. This gives the ability to track the path of the reflected fields from both panels with nearfield mapping (time domain). The obtained maps are normalized to one unified scale and presented in Fig. 3. 15. On these maps, the incident field in free space is not depicted. In particular, fig. 3. 15. (a) represents only the reflected field from the panels (config. 1) since this configuration is entirely in free space. On the other hand, fig. 3. 15. (b, c and d) show the incident Gaussian beam within the anisotropic medium superposed with the reflected fields from the left panel.

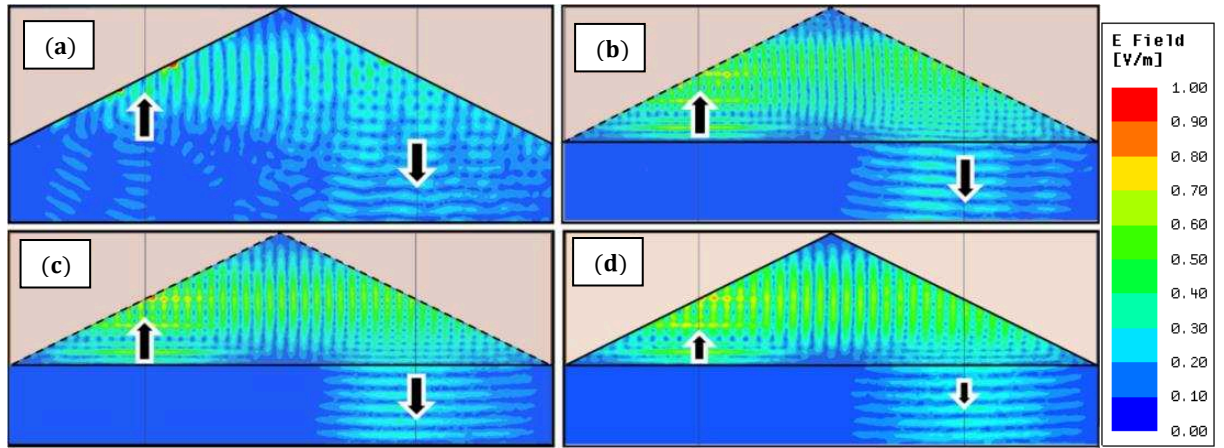


Figure 3. 15. Nearfield maps (time domain) for compact retro-directive reflector using (a) config. 1, (b) config. 2, (c) config. 3, (d) config. (4).

Globally, all configurations display a retrodirective behavior with a reflected Gaussian beam coming from the right panel and propagating downwards as seen from fig. 3. 15.

However, the retrodirective behavior is obviously better when the importance of TO with regards to SIM is increased. This is translated with highest parasitic lobe levels obtained for configuration 1 in fig. 3. 16. (showing normalized far field results). Those parasitic lobes might be linked to errors introduced by the realization of SIM over the reflector's panels (detailed discussion in chapter 4).

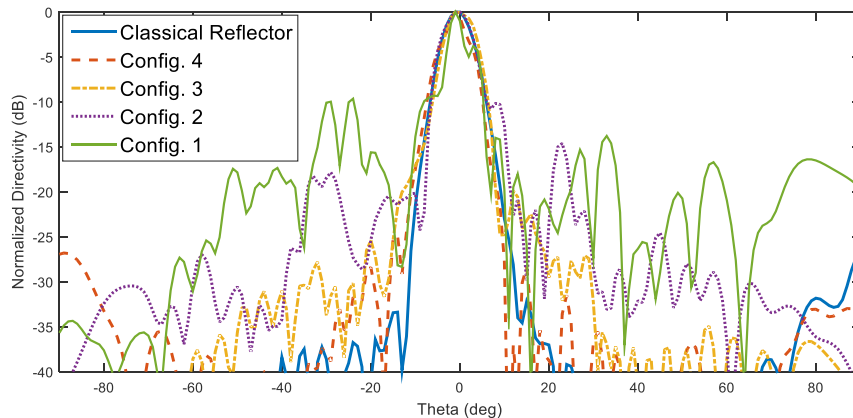


Figure 3. 16. Normalized Directivity (E-plane xy cut) for different configurations using a normally incident Gaussian beam.

While the results of figs. 3. 15 and 3. 16. insure that the conceived compressed configurations redirect the normally incident field from their panels into the desired retro direction, they do not take into account a real case scenario where the field is incident over both panels at the same time. They also do not give any information on the effect of the incidence angle over the retrodirective behavior. In the next section, we present radar cross section results that are able to cover these interrogations.

3. 3. E. Radar Cross Section for the Compressed Reflectors

This section provides more quantitative results with respect to incidence over the reflector's surface. Radar Cross Section simulations are used for the different configurations from section 3. 3. D. Fig. 3. 17. presents monostatic RCS for each of the reflector configurations. This means that the incident and reflected angles are identical (with $\theta = 0^\circ$ for normal incidence at the reflector's aperture). For comparison, the RCS of a classical corner reflector (cf. fig. 1. 4.) and that of a metallic sheet (with equivalent effective areas) are also given in the simulations results in fig. 3. 17. and analytically in table 3. 2. It is important to note that RCS is simulated while varying the incidence angle $-45^\circ \leq \theta \leq 45^\circ$ with a step of $+1^\circ$ between two consecutive RCS values obtained in fig. 3. 17.

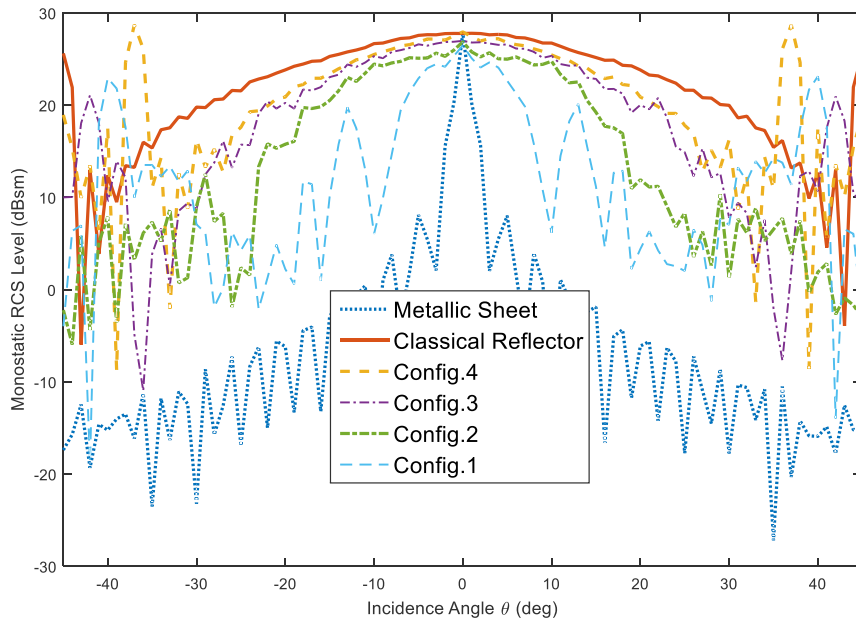


Figure 3. 17. Monostatic RCS response for different reflectors versus incidence angle θ .

As can be seen from fig. 3. 17., all compressed reflectors (config. 1 to 4) have a better beam width than the metallic sheet, which demonstrates the achieved retrodirective behavior is not limited to normal incidence.

It is important to mention in fig. 3. 17., for the classical reflector for example, at $\theta = \pm 45^\circ$ RCS level increases once again. This is also true for other configs as well but at different angles. This is mainly due to the fact that, at these angles, the field is normally incident over only one panel from the reflector. It is noteworthy also to indicate that the presence of the anisotropic medium filling the compressed reflectors alters the path of the fields which can be the cause for which those high levels are at different angles θ when compared to the classical reflector. The fluctuations in the RCS levels for all configurations, in fig. 3. 17., are mainly

due to the meshing process used in simulations (since the dimensions of the simulated structures are much larger than the operating wavelength and the meshing is chosen coarse to limit the computational cost).

Table 3. 2. provides the RCS levels at $\theta = 0^\circ$ along with the half-power beam width (HPBW) for the configs used in Fig. 3. 17.

Table 3. 2. Main performance for the different reflectors.

RCS Simulations	Metallic Sheet	Classical Reflector	Config. 1	Config. 2	Config. 3	Config. 4
Analytical RCS Level at $\theta = 0^\circ$ (dBsm)	28.5		-			
Simulated RCS Level at $\theta = 0^\circ$ (dBsm)	28.2	28.2	25.2	27.2	28.02	28.1
HPBW (deg)	2.72°	38°	14°	28°	30°	34°

First, the simulated RCS level for a metallic and a Classical reflector are approximately equivalent to that of the maximum analytical level for the same aperture at normal incidence ($\theta = 0^\circ$).

The maximum RCS level for all configs is a bit lower and none of them reaches the performance of the classical corner reflector. Configuration 4 (TO only) is the closest to the reference and the config. 1 (SIM only) is the most distant (with the lowest level and tightest beam width). This proves the consistency of the fact that the compression approach relying on SIM is quite sensitive to the incident angle [45, 46]. On the other hand, one should keep in mind that all configs reached an overall depth reduced by a factor of 2 ($a = 2b$).

On the other end, these results show that a small amount of SIM can significantly relax the anisotropic factor without affecting the performance too much. Typically, the performance of config. 3 is almost the same as that of config. 4 but with a 1.5 reduction factor in the anisotropy.

3.4. Conclusion

A new approach to compress retrodirective reflectors has been presented. It combines TO with SIM, providing a unified tool for controlling the reflected wave from an object by acting on both its surface and its volume material properties.

A generalized phase gradient has been derived theoretically for the reflecting panels, accounting for the presence of a filling anisotropic media. The capability to perform a trade-off between anisotropic factor and phase gradient when designing a reflector has thus been demonstrated. This offers a new degree of freedom to relax the constraints on required anisotropic media.

A surface impedance configuration has been verified within HFSS simulations as a first step to evaluate SIM. Then, a new TO/SIM physical model has been proposed conducted and validated with simulations for different configurations. These simulations have confirmed the expected retrodirective behavior is achieved for all tested configurations. They have also shown the introduction of a small dose of SIM is beneficial to reduce the anisotropic factor required by a pure TO configuration. Finally, the introduction of an anisotropic media can elevate greatly the performance of a pure SIM configuration but at the cost of a more complex reflector (involving some volumetric modulation of its constitutive medium).

As pointed out, in the next chapter, we discuss the source of parasitic reflections in unwanted directions that were obtained using SIM panels. New ways to control the levels of these reflections are addressed along with limitations that might affect the SIM panel's performance.

Chapter 4 - Mitigation of Parasitic Reflections over Surface Impedance Modulated Panels

A common challenge, for antenna designers, is the conception of surface impedance modulated (SIM) panels providing the desired radiation characteristics. SIM panels are used for many electromagnetic and antenna applications like metasurfaces [59], reflectarrays [60] and leaky wave antennas [61, 62]. Even when properly designed, unexpected artifacts in the radiation pattern appear, including radiation in undesired directions [63, 64]. These parasitic radiations greatly affect the performance of such panels.

The main reason for the existence of these parasitic lobes is radiated Floquet harmonics. When the surface impedance modulation is periodic, higher order modes are excited along with the fundamental mode. These excited modes directly reduce to waves propagating towards specific directions. It was proven in [63, 64] that it is impossible for a metasurface, as an example, to reflect a single plane wave of the same polarization as that of the incident plane wave. The only exceptions are actually the cases of specular or retro-reflections which respect the conventional reflection law.

The main goals of this chapter are to analyze and control the reflected waves from a SIM panel. Firstly, the directions of each reflected waves are studied for different configurations. Note that this provides a new insight in the origin of the parasitic lobes encountered in the previous chapter (section 3.3). Secondly, different implementations of SIM are compared and their influence on parasitic reflections is assessed. Finally, ways to control these parasitic reflections are explored.

In the first section, the theoretical directions for reflected fields from SIM panels are analyzed. Different configurations (involving both normal and oblique incidence) are considered. Simulations with HFSS for the different configurations are compared with their theoretical counterparts. In the second part, printed elements that implement SIM over a panel are presented and discussed as practical models for simulations. In the third part, the variation of different parameters over practical panels is conducted and their effects on the parasitic lobe levels are discussed. In the fourth part, the relation between the reflected phase sensitivity of a unit cell with its resonance ratio is established. The effects over the harmonics lobe levels are then compared for different unit cell types. Last in the fifth section, concluding remarks discuss the source of the parasitic reflections from SIM panels (in surface impedance and practical forms). Two new limitations are introduced for practical SIM panels in order to mitigate harmonic lobe levels for a given configuration.

This chapter relies solely on Full wave simulations with ANSYS® HFSS® to validate the theoretical part.

4. 1. Reflection Analysis of SIM Panels

The goal of this section is to shed the light over the source of parasitic reflections from SIM panels. In the first sub-section, the theoretical directions of these reflections are calculated for any desired incident and reflected configurations. In the second sub-section, the theoretical analysis is verified using three different configurations. SIM panels in this sub-section utilize another version of the impedance distribution developed within the previous chapter in sections 3. 1. and 3. 2. This version takes into consideration any incidence and reflection angles as in section 3. 3.

4. 1. A. Extended phase gradient and Theoretical Plane Wave Directions

In chapter 3, since we were using SIM panels for the application of a retrodirective reflector, it was convenient to relate, in the developed formulation, the incident and reflected fields. In section 3. 3. B., we verified the proper implementation of a SIM array (based on a discretization technique). Here, we aim at a more global understanding of the reflections from a SIM panel. To this extent, it is necessary to reintroduce the Phase Gradient needed over the panel for any incidence and reflection angles. We start by introducing the trajectories of incident and desired reflected plane waves from a discretized SIM panel in free space. The general configuration is illustrated in fig. 4. 1.

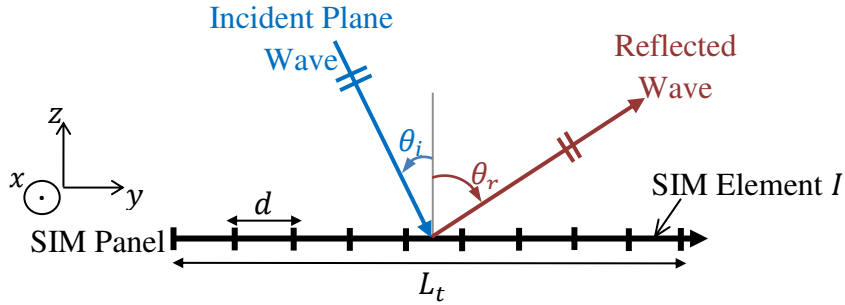


Figure 4. 1. General configuration used for the reflective SIM Panel.

In fig. 4. 1, the conventions here for the incident θ_i and reflection angle θ_r are more adapted to reflective Metasurfaces (different from the ones used in chapter 3 for the sake of generality). The total length of the SIM panel is presented as L_t and the length of each element is d . Different scenarios can be considered here. First, if the panel is constituted only of a PEC sheet, when illuminated by a plane wave, a single plane wave is reflected with a reflection angle $\theta_r = \theta_i$. This corresponds to the conventional reflection law [65].

In a configuration where the interest is to reflect a plane wave in a desired direction with $\theta_r \neq \theta_i$, the panel is then constituted of a SIM.

In this scenario the phase gradient used is defined as follows:

$$\frac{d\phi_{\Gamma}(y)}{dy} = k_0[\sin(\theta_r) - \sin(\theta_i)] \quad (4-1)$$

Simulations, in chapter 3, divided each panel into I elements with length d and an incremental phase shift was applied on element i as:

$$\phi_{\Gamma_i} = \phi_{\Gamma_1} - (i - 1)\gamma \quad (4-2)$$

with γ being the phase increment between consecutive elements:

$$\gamma = \frac{d\phi_{\Gamma}(y)}{dy} d \quad (4-3)$$

Surface impedances for SIM unit cells were introduced via their local reactance X_{si} and this stays true here:

$$X_{si} = \frac{Z_{TM}}{\tan\left(\frac{\phi_{\Gamma_i}}{2}\right)} \quad (4-4)$$

It is well known that the impinging wave impedance at TM polarization is dependent on its incident angle with $Z_{TM} = \eta_0 \cos \theta_i$.

A continuous SIM involves a periodic loading of the reflective panel. Let's introduce here the spatial period T_y which is the length of the SIM portion that fulfills a 2π phase cycle for the phase of the reflected wave. This period is known as the surface super lattice in Metasurfaces domain as in [66]. It actually depends on the desired incidence and reflection field angles. It can be computed as follows:

$$T_y = \frac{2\pi}{k_0 |\sin(\theta_r) - \sin(\theta_i)|} \quad (4-5)$$

If the SIM panel has a total length $L_t > T_y$ (which is usually the case since several periods are required along the panel). Due to this periodicity, a combination of Floquet harmonics plane waves will be reflected, each towards a specific direction θ_n . In order to determine the exact direction for each plane wave we define the wave numbers of each reflected plane wave with respect to the panel's axis as shown in fig 4. 2.

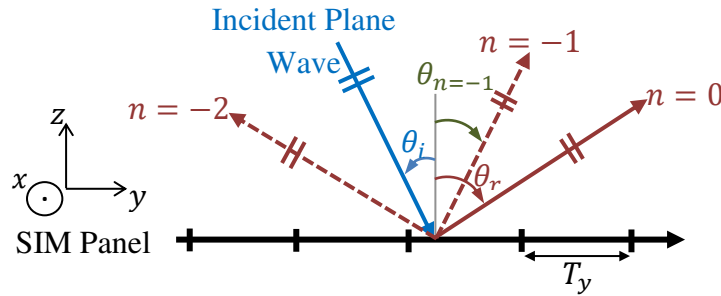


Figure 4. 2. Trajectories of plane waves reflected from a periodic SIM Panel.

The y component of the wave vector for the n^{th} order harmonic ($n \in \mathbb{Z}$) is:

$$k_y^n = k_y^0 + \frac{2\pi n}{T_y} \quad (4-6)$$

with

$$k_y^0 = k_0 \sin(\theta_r) \quad (4-7)$$

and where k_0 is the wave number in free space.

We get then from eq. (4-5) the following:

$$k_y^n = k_0[(n + 1) \sin(\theta_r) - n \sin(\theta_i)] \quad (4-8)$$

The reflection angle θ_n for the n^{th} order harmonic can then be calculated as follows:

$$\theta_n = \arcsin\left(\frac{k_y^n}{k_0}\right) \quad (4-9)$$

From eqs. (4-8) and (4-9), we can determine the theoretical directions of the plane waves reflected due to Floquet harmonics from a periodic SIM panel. The total number of these reflected waves depends on the incidence angle θ_i and the desired reflection angle θ_r .

To better understand this phenomenon, we take the example of a normally incident plane wave with $\theta_i = 0^\circ$ and a desired reflection angle $\theta_r = 60^\circ$. In such a configuration, the $n = 0$ a plane wave is reflected at $\theta_0 = \theta_r = 60^\circ$ which is the desired direction of reflection. For $n = -1$ and $n = -2$, two other plane waves are propagated at $\theta_{-1} = 0^\circ$ (which is known as the specular reflection) and $\theta_{-2} = -60^\circ$. On the other hand, choosing any other value for n , at this specific configuration, yields θ_n as complex valued angles. These angles do not reflect any plane waves within the radiation continuum. They are considered as evanescent modes. The goal of the next section will be to verify the obtained theoretical directions of radiated Floquet harmonics through different simulated classical (with pure reactive elements) SIM panels.

For discretized panels, the same problem occurs. However, periodicity is only met exactly if T_y is a multiple of d (element's length). This condition will be satisfied in the next sections to better analyze the effect of periodicity.

4. 1. B. Verification of Floquet Harmonics using SIM Panels

The aim of this section is to confirm the excitation of higher order Floquet harmonics in the form of parasitic lobes (plane waves in undesired directions) with the help of HFSS simulations. First, a semi-infinite full wave simulation scenario is used. For a more general view, different configurations (involving different incident and/or reflected angles) along with their respective impedance distributions are compared with their analytical counterpart.

4. 1. B. i. Semi-Infinite SIM Panel Simulation Settings

We present here the different settings used for HFSS simulations.

Three different simulations are conducted, each having a TM polarized (H-field along x -axis) incident plane wave at $f = 8GHz$ as shown in fig. 4. 3. Perfect Magnetic Conductor (PMC) sheets are used at both sides of the panel (parallel to the yz plane). These PMC planes insure that the panel is infinite along the x -axis.

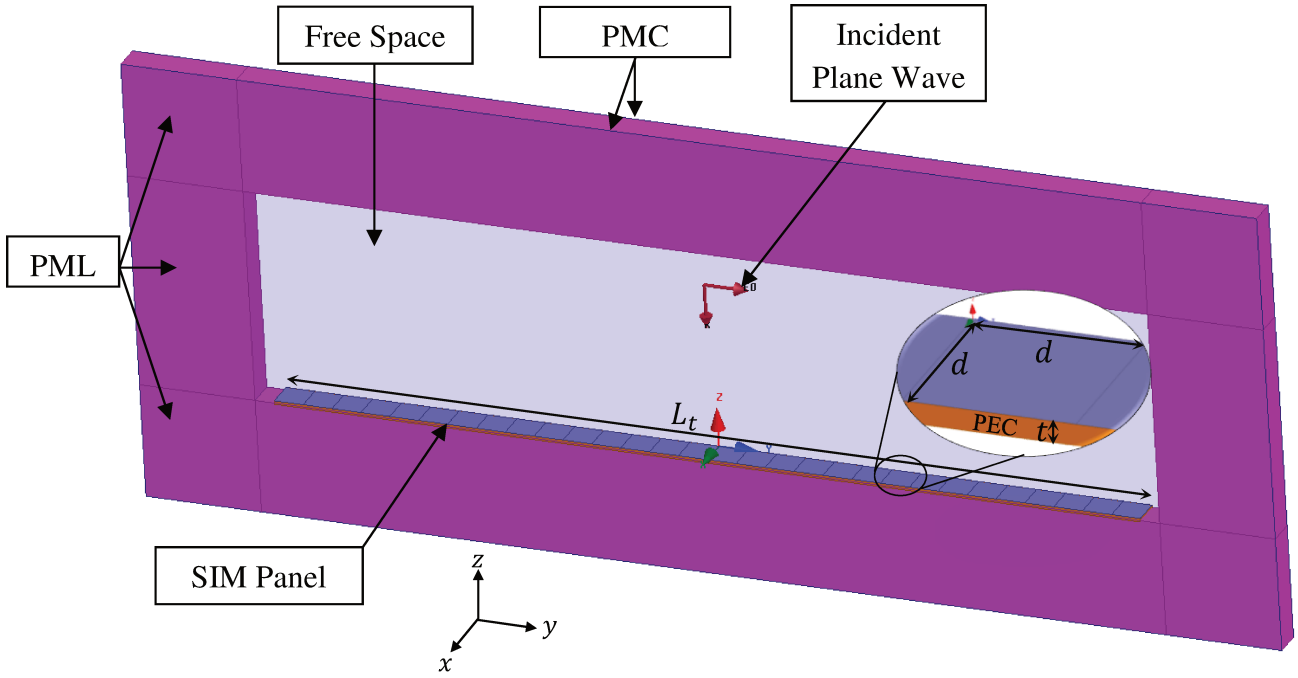


Figure 4. 3. Simulated configuration for an incident plane wave over a semi-infinite SIM panel.

Each panel is divided into I unit cells of dimension d in the y direction. All the configurations are chosen so that they respect $d < \frac{\lambda_0}{2}$ and a total length $L_t \approx 10\lambda_0$ along the y -axis. The parameters used for simulations of the three different configurations are shown in table 4. 1.

Table. 4. 1. Parameters used for the simulated semi-infinite Configurations.

Panel Configurations	Spatial Period T_y	Panel's Total Length L_t	Nb. Of Unit Cells I	Unit Cell's dimension d
Config. 1 $\{\theta_i = 0^\circ; \theta_r = 30^\circ\}$	$2\lambda_0$	$10\lambda_0$	30	$\frac{\lambda_0}{3}$
Config. 2 $\{\theta_i = 0^\circ; \theta_r = 60^\circ\}$	$1.152\lambda_0$	$10.368\lambda_0$	36	$0.288\lambda_0$
Config. 3 $\{\theta_i = 60^\circ; \theta_r = 15.42^\circ\}$	$\frac{5}{3}\lambda_0$	$10\lambda_0$	30	$\frac{\lambda_0}{3}$

From table 4. 1., it is important to draw attention that the number of unit cells per spatial period T_y (equal to $\frac{T_y}{d}$) is an integer for all configurations. This specific choice assists in pointing out the periodicity of the surface reactance distribution (as will be shown in the next sub-section).

Last, a volumetric PEC medium with a thickness $t = 0.0426\lambda_0 = 1.6mm$ is used under the panel's elements in order to insure their awaited "behavior" in simulations as proven in chapter 3 (section 3. 3. A).

4. 1. B. ii. Periodic distributions for reflecting SIM panels:

In fig. 4. 4, surface reactance distributions are plotted using eq. (4-4) for the different panel configurations introduced in table 4. 1.

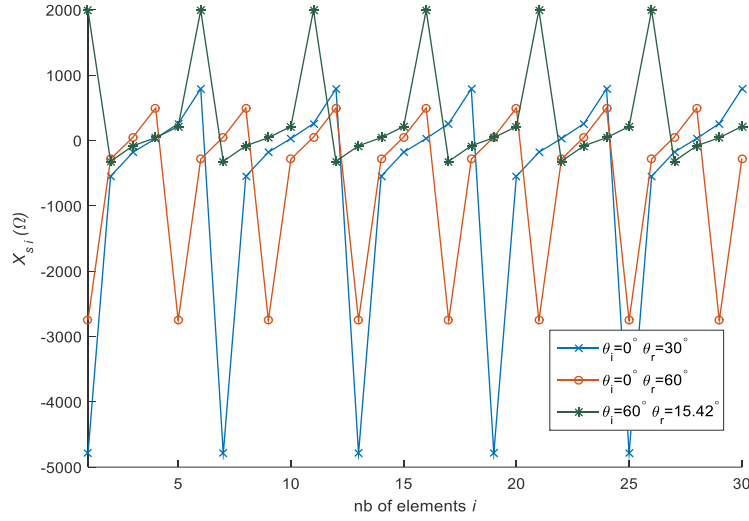


Figure 4. 4. Periodic Surface Reactance Distributions for different reflecting SIM panels.

Fig. 4. 4. shows the periodicity of the surface reactance distributions for all configurations. The observed periods are well consistent with those obtained in theory using eq. (4-9) and in table 4. 1. Having such periodic distributions gets in line with the fact (discussed earlier in section 4. 1. A.) that more than one plane wave will be radiated from the panel in different directions. Distributions from fig. 4. 4. are used in the simulations of the SIM panels accordingly.

4. 1. B. iii. SIM Panels Simulation Results

Radiated far field results are shown in this sub-section for the different panel configurations. The surface reactance distributions used for each of the panels are those introduced in fig. 4. 4. The obtained far field lobes directions are compared with their theoretical directions obtained from eq. (4-9).

In the case of fig. 4. 5., at normal incidence ($\theta_i = 0^\circ$), three excited Floquet harmonic modes propagate. Consequently, three plane waves are reflected in different directions and observed in the far field results as three lobes. The fundamental mode $\theta_0 = \theta_r = 30^\circ$ is that of the desired reflection. The specular reflection at $\theta_{-1} = 0^\circ$ can be called the retro-reflection and, at $\theta_{-2} = -30^\circ$, an image reflection of the desired one is present in far field results. Similarly, in fig. 4. 6., the fundamental mode at $\theta_0 = \theta_r = 60^\circ$ is obtained along with the retro-reflection at $\theta_{-1} = 0^\circ$ and the image reflection at $\theta_{-2} = -60^\circ$.

At oblique incidence, different harmonic modes are excited. In fig. 4. 7., for example, the fundamental mode at $\theta_0 = \theta_r = 15.42^\circ$ is obtained along with the retro-reflection at $\theta_{-1} = 60^\circ$ and two other harmonic modes at $\theta_1 = -15.42^\circ$ and $\theta_2 = 69.12^\circ$. The number of modes actually depends on the incidence and reflection angles. The only modes that persist for any

incidence and any reflection are the fundamental mode along with θ_{-1} , which yield the desired and the specular reflected waves.

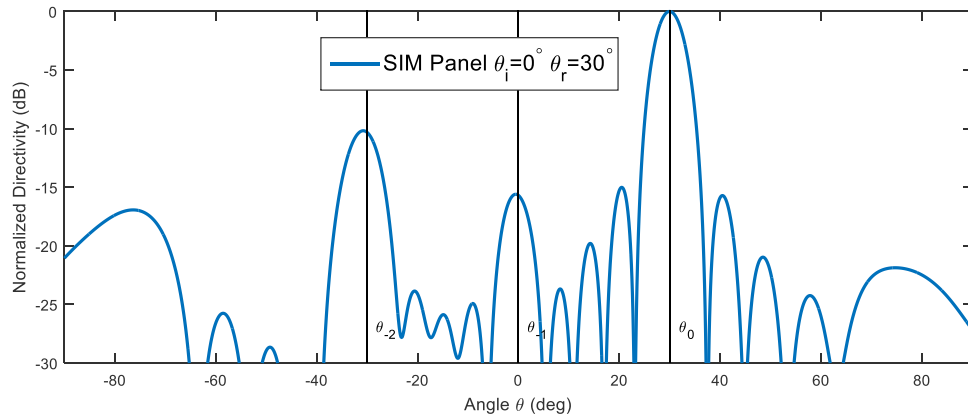


Figure 4. 5. Normalized Radiated field cut (along yz plane) from a normally incident plane wave over config. 1 (table 4. 1.).

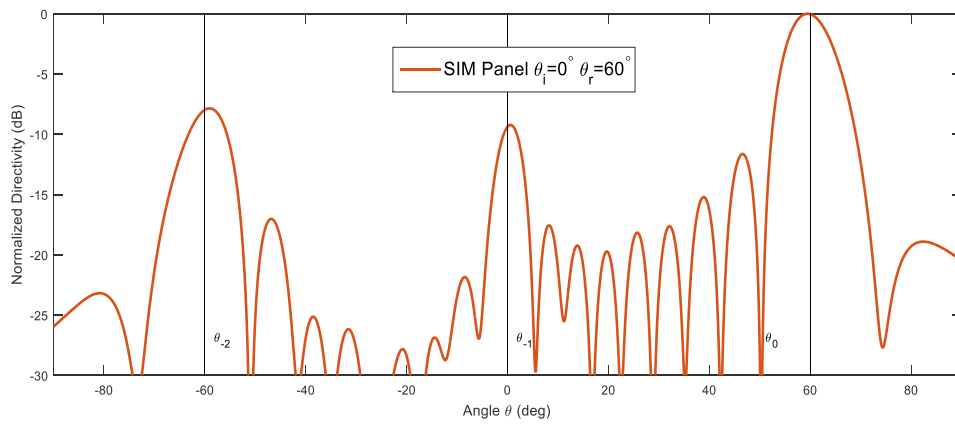


Figure 4. 6. Normalized Radiated field cut (along yz plane) from a normally incident plane wave over config. 2.

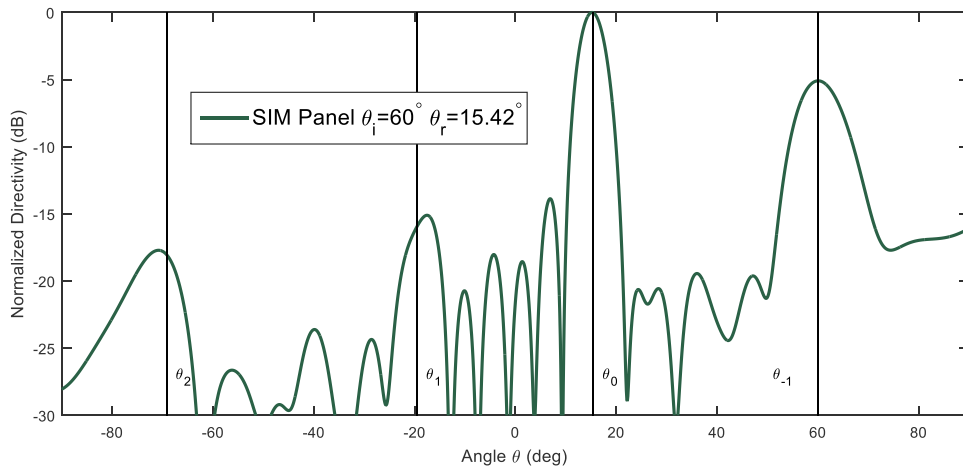


Figure 4. 7. Normalized Radiated field cut (along yz plane) from an oblique incident plane wave over config. 3.

Black vertical lines in figs. 4. 5, 4. 6, and 4. 7. represent the theoretical directions calculated from eq. (4-9). It is clear from those figures that the desired reflections are achieved (for $\theta_0 = \theta_r$). They also show that the harmonic lobe directions are all in line with their theoretical counterpart for any panel configuration.

On the other hand, it is apparent that parasitic lobe levels change according to the respective configuration. More details on the lobe levels are discussed in the coming sections for practical SIM panels. A study to mitigate those levels will also be presented.

4.2. Practical Implementation for SIM Panels

In this section, panels that realize SIM using practical printed elements are introduced. Different types of printed elements are used following the reasoning of an antenna designer. Such a reasoning prioritizes having the panel reflect the fields in the desired direction with parasitic lobes at levels lower than that of conventional side lobes (-13.5 dB).

We choose to practically implement the config. 2 $\{\theta_i = 0^\circ; \theta_r = 60^\circ\}$, since it showed high levels ($>-13.5\text{dB}$) for all its parasitic harmonic lobes at normal incidence.

4.2.A. Use of Practical Unit Cells for SIM panels

Different types of unit cells can be used in order to practically implement SIM panels.

A popular solution in the antenna domain is the methodology used for printed reflect-arrays. It consists of printed metallic elements over a grounded dielectric substrate as illustrated in fig. 4. 8. Each unit cell must achieve a specific value of the surface impedance distributions discussed in sub-section 4. 1. B. ii.

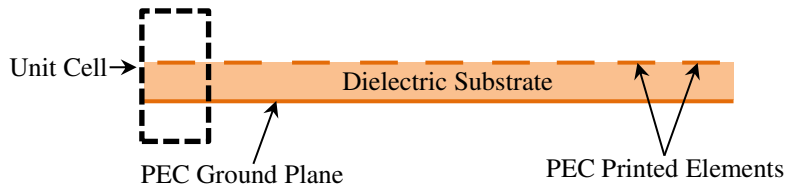


Figure 4. 8. Illustration of a Practical SIM Panel.

In other words, it must produce the appropriate reflection phase response ϕ_{Γ_i} .

The most classical and simple type, an antenna designer would start with, is printed dipoles. In the coming sections, we're going to start by assessing the performance of a SIM panel using printed dipoles.

4.2.B. Reflection Phase Response for the Unit Cell

It is well known, that the reflection response of a panel depends directly on the response of each of its unit cells [68, 69]. In this section, we simulate the response of printed dipoles in infinite periodic simulations with HFSS (also known as Floquet's approach).

In such simulations, one unit cell containing a printed dipole element with a geometrical control parameter is simulated. The reflection phase response of the printed dipole versus its control parameter should, in theory, cover a 360° phase range. Then, different dipoles with different phase responses can be chosen to synthesize the required SIM.

Now, we define the parameters used in order to establish the phase range for the dipole. As shown in figure 4. 9., The dielectric substrate used is the “Cuclad 5880” with a relative permittivity $\epsilon_r = 2.17$ and height $h = 0.0426\lambda_0 = 1.6mm$. The substrate is grounded using a PEC sheet on its back face. The squared unit cell’s dimension is $d = 0.288\lambda_0 = 10.8mm$. It is chosen to be coherent with the given 4 elements per T_y defined for the specific config. 2 (from table 4. 1.) with an incident plane wave polarized along y at $f = 8GHz$. A rectangular PEC dipole with fixed width W and variable length L (being its geometrical control parameter) is used on the top layer of the substrate.

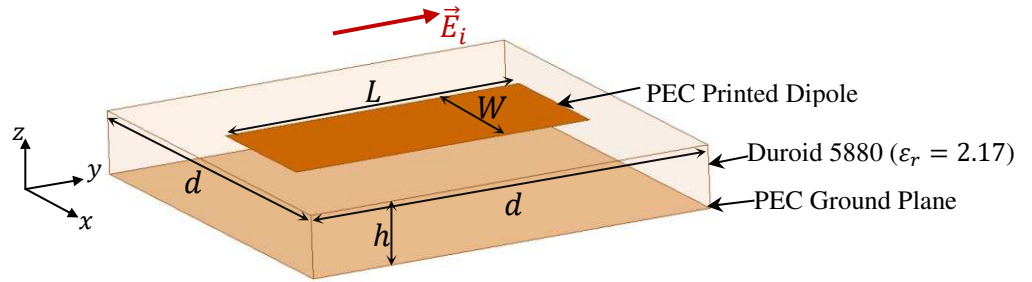


Figure 4. 9. Illustration of the simulated unit cell (3D view) with a dipole element. Incident E-field along +y.

The reflection phase response is plotted versus the dipole’s length L for different widths W in fig. 4. 10. The reflection phase response covers a certain phase range as the dipole’s length L changes while having a fixed width W .

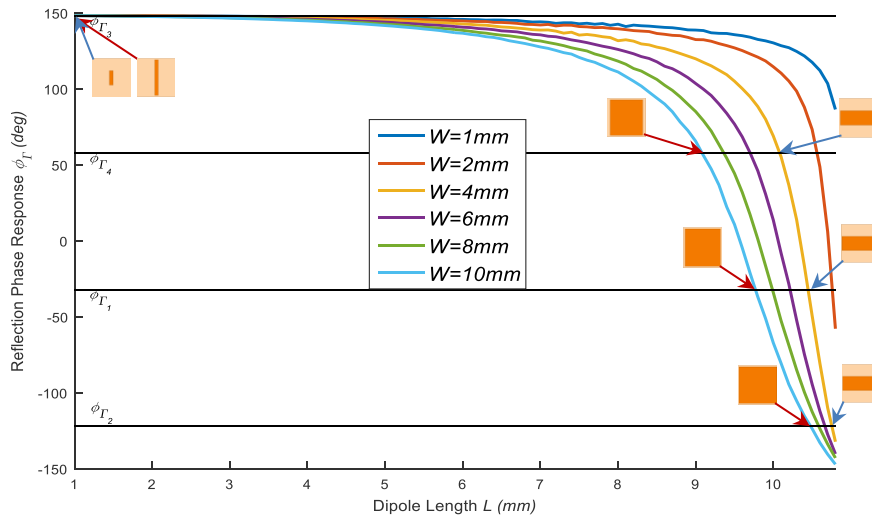


Figure 4. 10. Reflection Phase Response for a unit cell versus the dipole’s length in Floquet’s simulation.

In fig. 4. 10., not all dipole widths yield the required phase range for the intended configuration. From eq. 4. 8., we have $\gamma = 90^\circ$ and 4 unit cells per T_y so a phase range $\phi_r = 270^\circ$ is needed for this configuration.

For $W = 1mm$ we have $\phi_r = [86.5^\circ; 148^\circ]$ and for $W = 10mm$ we have $\phi_r = [-147^\circ; 148^\circ]$. We can deduce here that as the dipole’s width gets bigger, the phase

range increases and the phase response gets smoother. Usually, a smoother phase response leads to a smaller phase range, which is not the case here. In fact, as seen in fig. 4. 10., the given unit cell dimension d does not allow narrower width elements to totally reach their resonant state, which explains why their phase range is reduced. For the unit cells to be implemented within our panel configuration (config. 2), only cases with $W \geq 4mm$ provide the required 270° phase range.

To pass on to the implementation of the unit cells within the total panel, the phase of the first element is chosen randomly $\phi_{r_1} = -32^\circ$. It results in the 4 following phase states : $\phi_{r_1} = -32^\circ$, $\phi_{r_2} = -122^\circ$, $\phi_{r_3} = 148^\circ$ and $\phi_{r_4} = 58^\circ$. Then, the associated lengths are chosen from phase responses as shown in fig. 4. 10. by the horizontal black lines representing the required phase states. Complete spatial periods for four different dipole widths W are shown in fig 4. 11.

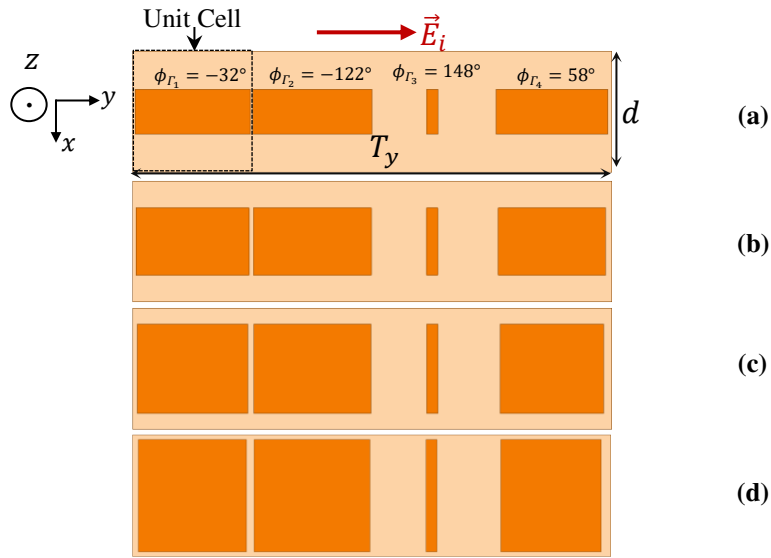


Figure 4. 11. Complete Spatial periods T_y (Top View) for four different Dipole widths $W = 4mm$ (a) $W = 6mm$ (b) $W = 8mm$ (c) $W = 10mm$ (d).

4. 2. C. Simulated Radiated Fields for Semi-Infinite Panels

Radiated far field cuts for semi-infinite panels are shown in this part. The cells distributions used for each of the panels are those introduced in fig. 4. 11. All panels have a total length $L_t = 9T_y = 10.368\lambda_0$ along the y axis as shown in fig. 4. 12.

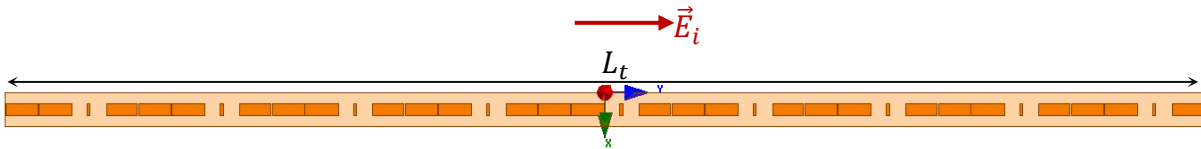


Figure 4. 12. Simulated semi-infinite panel using printed dipoles as unit cell elements.

The obtained far field lobes directions are compared with their theoretical directions from eq. (4-9).

It is shown in fig. 4.13, that the desired reflection is achieved (for $\theta_0 = \theta_r = 60^\circ$) along with the parasitic lobes, which are in line with the theoretical predictions.

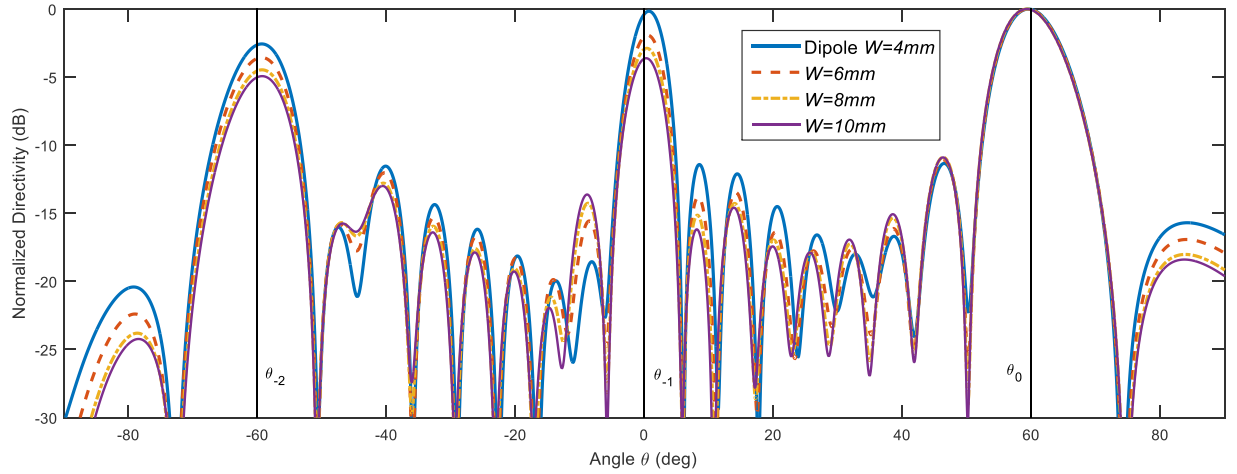


Figure 4.13. Normalized Radiated field cut (along yz plane) from a normally incident plane wave over the corresponding practical panel with 4 unit cells per T_y and $L_t = 9T_y$. Black vertical lines represent the directions calculated from eq. (4-9) with $\theta_0 = \theta_r = 60^\circ$; $\theta_{-1} = 0^\circ$ and $\theta_{-2} = -60^\circ$.

Nevertheless, it is obvious that parasitic lobe levels at θ_{-1} and θ_{-2} decrease while increasing the width W of the elements. In [48], it is suggested that applying dipole elements with increasing width W is able to mitigate the specular reflection for offset fed reflectarrays. We can deduce that these results are in line with the works conducted in [48]. However, the used configuration in [48] is a bit different, which can explain why all our observations do not apply to this publication. The main difference lies in the fact that our study assumes an incident plane wave while in [48] a source (pyramidal horn) is used with a spherical wave front. The consequence is that the conceived reflectarray panel was not truly periodic, which probably explains the fact that only the specular reflection is observed while the parasitic lobe at θ_{-2} is negligible. In [48], the authors attributed the decrease in the specular reflection levels to the amount of ground plane exposed to the incident radiation (since bigger widths for the dipole elements yield less exposed ground plane). In the coming section, we will present a scenario that contradicts this explanation.

Even though these levels decrease to a certain extent (-5dB), an antenna designer will still find them too high when compared to the main lobe level (at θ_0). Unfortunately, we pushed the dipole element to its extents ($W=10\text{mm}$ closest to the unit cell's length d). Still, Parasitic levels need to be lower than -13.5dB in order for the design to be considered reflecting in its desired direction with negligible parasitic lobes. So, a designer would think of ways to overcome these limitations. In the next section, different minimization techniques for the parasitic lobe levels are introduced following a classical antenna designer reasoning.

4.3. Mitigation of Parasitic Lobe Levels

In this section, techniques for minimizing the harmonic lobe levels are addressed. Different degrees of freedom are explored, each having a different effect on the reflection characteristics from the practical SIM panel (config. 2 from table 4. 1). First, the effect of changing the unit cell dimensions is discussed. The influence of choosing a specific phase offset (absolute phase of the first element) is also addressed. Last, the effect of a miniaturization technique for the printed elements is studied.

4.3.A. Effect of changing the unit cell dimensions

Following the limitations introduced earlier (in 4. 2. C.), we move to 3 unit cells per T_y while following the same steps used in section 4. 2. We now have a unit cell's length $d = 0.383\lambda_0 = 14.43mm$ (keeping the $d < \frac{\lambda_0}{2}$ limitation) and the needed incremental phase $\gamma = 120^\circ$. Parameters for the simulated configuration and the constituting grounded substrate of the panel remain the same as in 4. 2. B. ($L_t = 9T_y$, $h = 1.6mm$ and $\epsilon_r = 2.17$).

We start by simulating the reflection phase response for the new unit cell with fixed dipole width W and variable length L as shown in fig. 4. 14. In this case, the width W can be pushed to higher values than those used in section 4. 2. (up to $W = 14mm$ instead of $W = 10mm$).

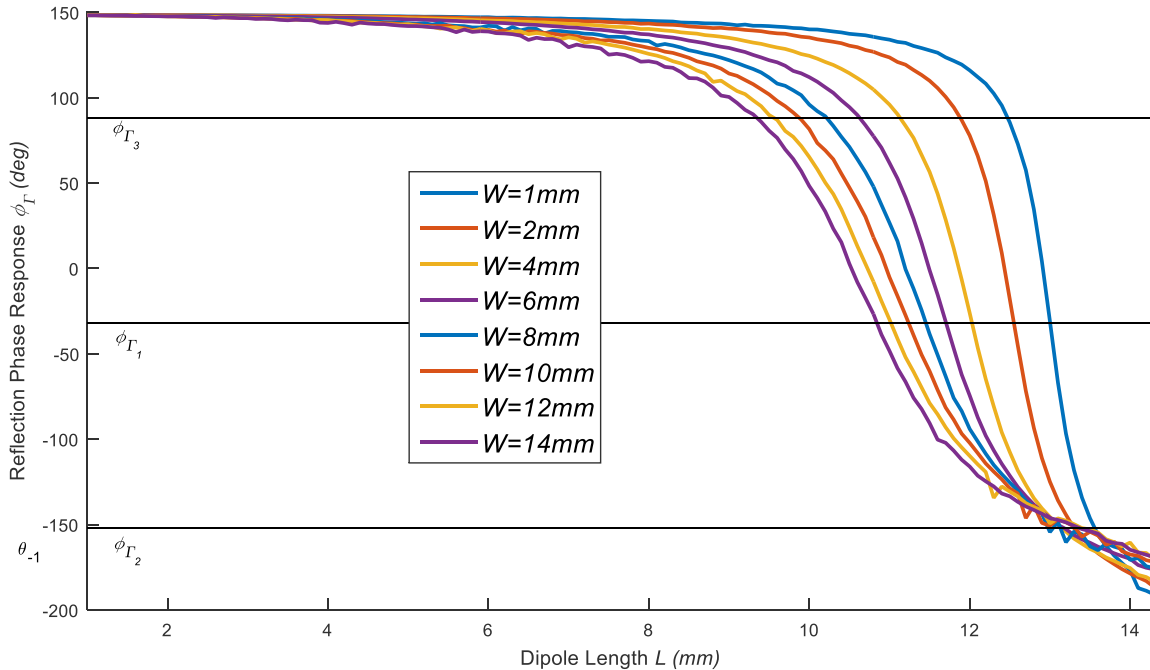


Figure 4. 14. Reflection Phase Response for a unit cell versus the dipole's length in Floquet's simulation.

First, it is evident from fig. 4. 14. that the phase ranges obtained are all sufficient to implement a panel for the case of config. 2 $\{\theta_i = 0^\circ; \theta_r = 60^\circ\}$. As the width W increases, the phase response of the unit cell becomes smoother but the achieved phase range is a bit reduced, which is now logical. For $W = 1mm$ we have $\phi_\Gamma = [-191^\circ; 148^\circ]$ and for $W = 10mm$ we have $\phi_\Gamma = [-169^\circ; 148^\circ]$.

Next, constituting unit cells for the panel are chosen with a phase offset $\phi_{T_1} = -32^\circ$. Note that the phase offset ϕ_{T_1} is the same as the one used in the previous section. However, the influence of changing such value will be studied later on. The panels are then simulated for fixed dipole widths W .

Fig. 4. 15. presents radiated field results for panels with different dipole widths W for the same studied scenario as in section 4. 2. C.

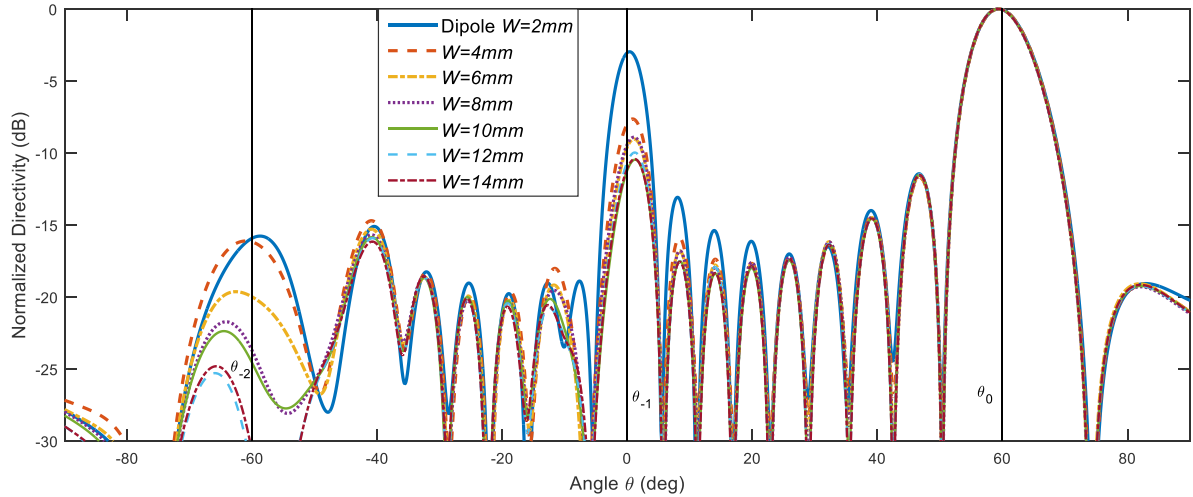


Figure 4. 15. Normalized Radiated field cut (along yz plane) using a panel containing 3 unit cells per T_y and $L_t = 9T_y$.

It is shown from fig. 4. 15. that all results yield a main lobe in the desired direction. It is noticeable that the Harmonics Lobe Levels (HLL) decrease with the increase of the dipole width W . When the dipole's width $W \geq 6mm$ HLL at θ_{-2} are around -20dB and can be considered insignificant. The lowest levels are obtained for $W = 14mm$ are HLL=-11dB at θ_{-1} and HLL=-25dB at θ_{-2} .

Globally, it seems results in fig. 4. 15. are better than those obtained previously (in fig. 4. 13.). This suggest a lower number of unit cells per T_y should be preferred.

To make the comparison completely fair, we extracted, in fig. 4. 16., two configurations with the same dipole width ($W = 10mm$), one with 4 unit cells per T_y and the other with only 3.

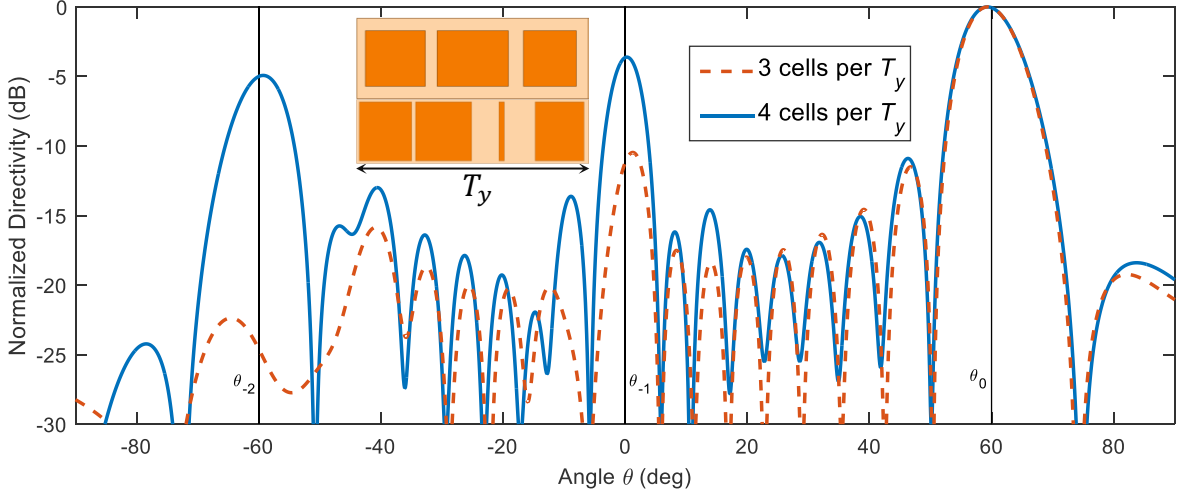


Figure 4. 16. Normalized Radiated field cut (along yz plane) using panels with dipole widths $W=10\text{mm}$ for 3 and 4 unit cells per T_y (their top view included).

HLL levels obtained for 3 unit cells per T_y are much lower (HLL= -11.2dB at θ_{-1} and HLL= -24.6dB at θ_{-2}) than those of 4 unit cells (HLL= -3.6dB at θ_{-1} and HLL= -5dB at θ_{-2}). In this case, having 3 unit cells per T_y does not correspond to smaller exposed ground plane area than 4 cells. Yet, it yields much lower HLL. Consequently it is evident that this comparative result contradicts what is perceived in [48].

From closer examination of figs 4. 15. and 4. 16., we suspect that the decrease in HLL levels can be mostly related to the smoother reflection phase response obtained for increasing dipole widths. This assumption will be studied in details in section 4. 4.

For the moment, we go on investigating other parameters that might have some impact on parasitic reflections.

4. 3. B. Effect of changing the offset phase on the panel's performance

Another parameter that may affect a panel's reflection performance is the offset phase (starting phase ϕ_{r_1}).

Taking the reflection phase response of dipole elements with width $W = 2\text{mm}$ with 3 unit cells per T_y , as an example, a shift in the phase distribution of the unit cells is introduced. The end results of panels with different dipole widths will be shown later on.

Here, we change the offset for the configurations studied in fig. 4. 15. We choose two different phase offsets $\phi_r = 28^\circ$ and $\phi'_r = \phi_r + 25^\circ$. Fig. 4. 17. illustrates the modification of the successive phases for the example $W = 2\text{mm}$. Of course, the consequence is that the used dipoles have a different geometry depending on the applied offset.

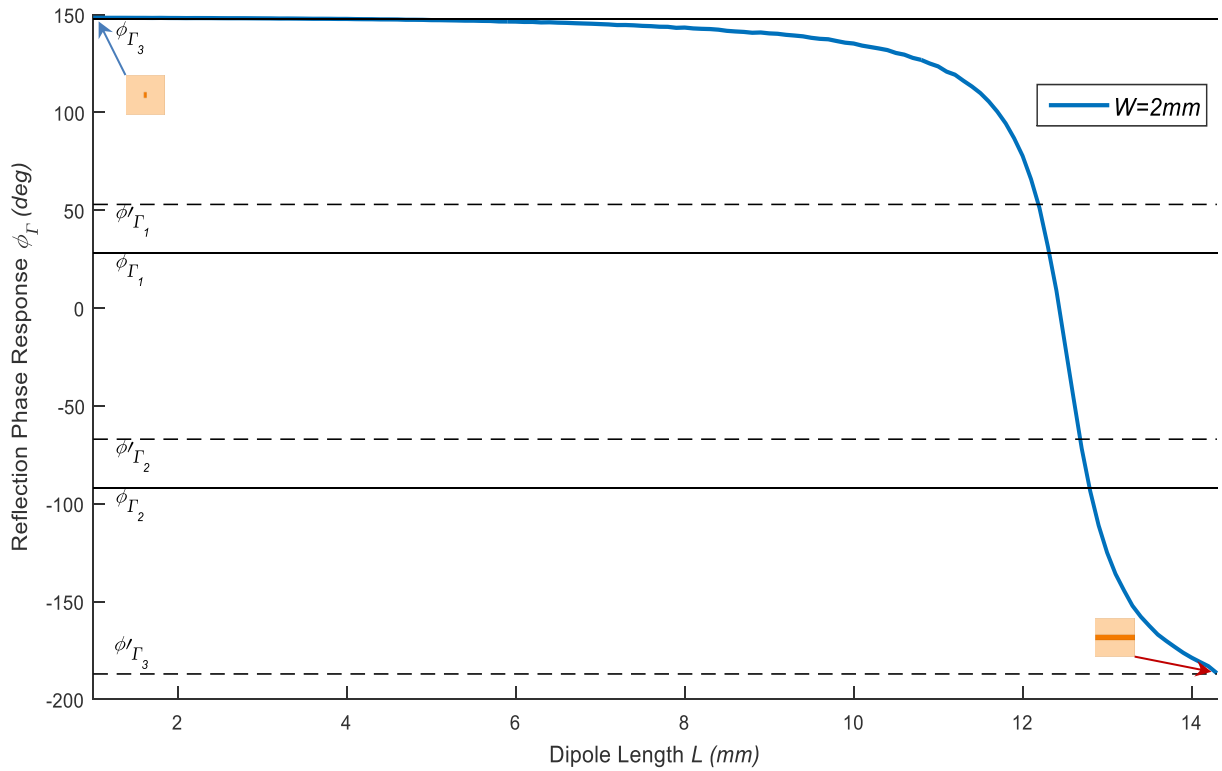


Figure 4. 17. Choosing two different offset from the reflection phase response of a unit cell with a dipole element.

Fig. 4. 18. depicts the corresponding dipoles for $\phi_{r_1} = 28^\circ$ (a) and $\phi'_{r_1} = 53^\circ$ (b). It is shown that the modification in geometry is especially significant for the third element.

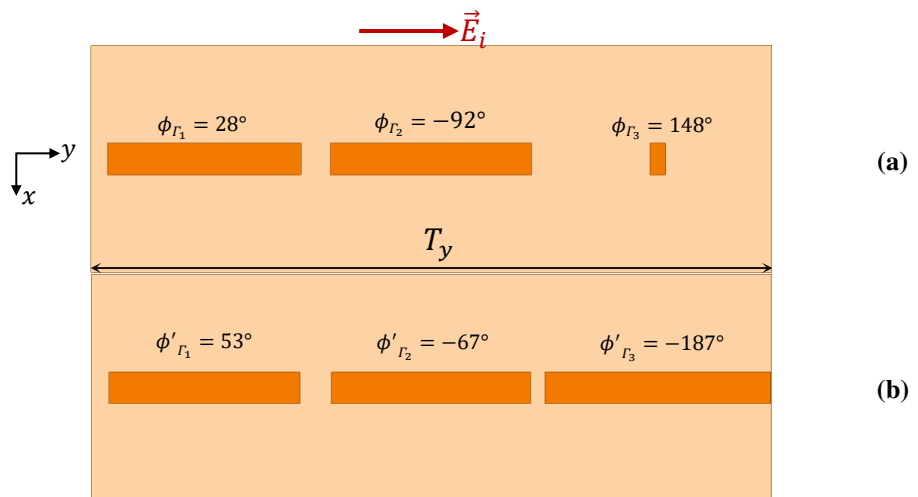


Figure 4. 18. Geometrical variation for complete periods T_y (Top View) of a panel configuration with dipoles widths at $W = 2\text{mm}$ and phase offsets $\phi_{r_1} = 28^\circ$ (a) $\phi'_{r_1} = 53^\circ$ (b).

Fig. 4. 19. Presents radiated field results for panels with different dipole widths W and both phase offsets for the scenario presented in section 4. 2. C.

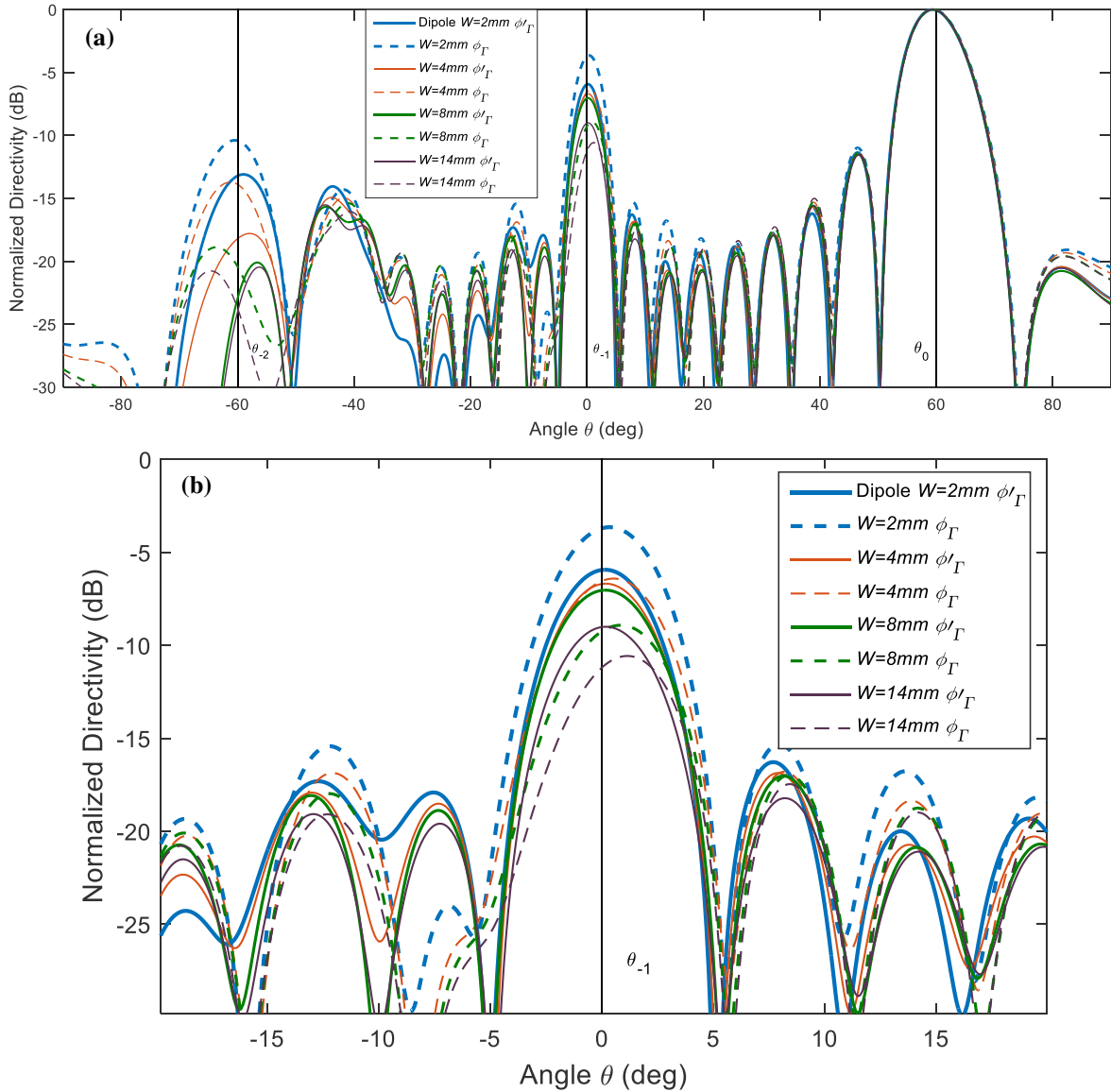


Figure 4.19. Normalized Radiated field cut (along yz plane) for different dipole widths at W and phase offsets (a) with a close up at the specular reflection θ_{-1} (b).

Fig. 4.19. shows that all results preserve a main lobe in the desired direction θ_0 .

It is evident that the HLL levels vary with the change in the phase offset for a given dipole element width W . At dipole widths $W \leq 4mm$ and $\phi_{\Gamma_1} = 28^\circ$ yield HLL levels higher than those of $\phi'_{\Gamma_1} = 53^\circ$. On the other hand, dipole widths $W \geq 6mm$ and $\phi_{\Gamma_1} = 28^\circ$ yield HLL levels lower than those of $\phi'_{\Gamma_1} = 53^\circ$.

The HLL is related, in this scenario, to the chosen starting phase offset ϕ_{Γ_1} . We can conclude, from this sub-section and from an antenna designer point of view, that for a given element configuration the phase offset should be optimized in order to obtain minimal HLL. For better coherence of the results in the upcoming sections and to be able to identify other anomalies that relate to high HLL levels, all practical panels take into consideration the same phase distribution along the unit cells with a phase offset $\phi'_{\Gamma_1} = 53^\circ$.

4. 3. C. Effect of Miniaturizing the element on the panel's performance

In the previous sub-sections, we have seen that HLL is closely related to the way the required phase law is implemented on the panel. We were able to mitigate HLL by changing geometrical parameters on the offset phase. For all studied configurations, the resonant behavior of the cell is reached when the dipole length approaches its maximum possible values (i.e. when L is close to d , the unit cell size). This can be seen clearly in fig. 4. 14. and 4. 10. where the rapid phase variations (resonance) are observed for higher dipole lengths (on the right of the plot). Here, a miniaturization technique for the dipole element is presented. The goal is to see whether it can be beneficial to shift the resonance so that it is reached for smaller dipole lengths (compared to the cell's size).

The miniaturization of the dipole is conducted by introducing extensions at its two extremities along x . Both extensions have a fixed length L_c and width W as shown in fig. 4. 20. This new type of element is named "H dipole".

There exist other forms of miniaturizing the printed element, for example using a slotted patch but that will not be detailed here. Comparative results will be shown in the next section.

In this case, it is well known that as the element is miniaturized within the unit cell, the reflection phase resonance of the unit cell can be achieved with a smaller length L .

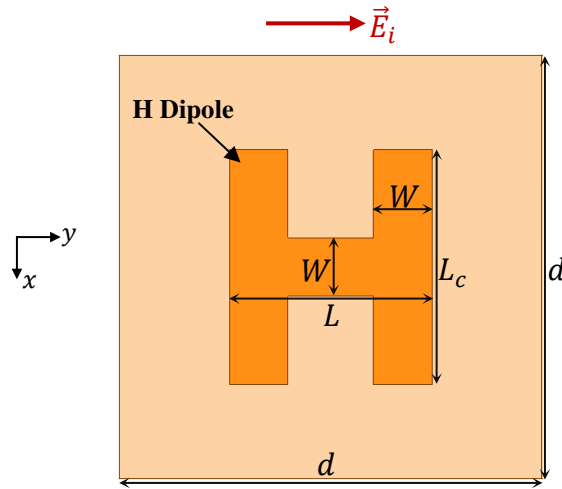


Figure 4. 20. Illustration of the simulated unit cell (Top View) with an H dipole element. Incident E-field along $+y$.

The reflection phase responses are simulated and the obtained results are depicted in fig. 4. 21. For each curve, the element's width is $W = 2mm$ and extensions length L_c are fixed while the element's length L varies. The phase response is simulated for different values of L_c (from $L_c = 2mm$ that represents an ordinary dipole to $L_c = 14mm$ close to the extremity of the unit cell's d). The unit cell dimensions remain the same as in sub section 4. 3. A ($d = 0.383\lambda_0 = 14.36mm$, 3 unit cells per period T_y). Parameters for the grounded substrate are also kept the same as in 4. 2. B. ($h = 1.6mm$ and $\epsilon_r = 2.17$).

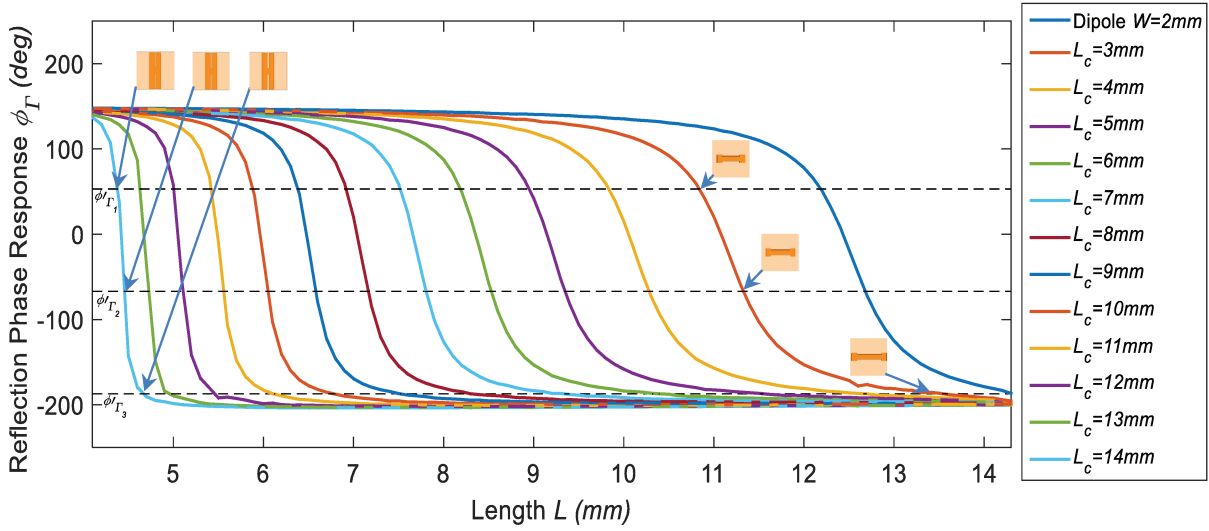


Figure 4. 21. Reflection phase response for a unit cell versus the miniaturized H dipole's length L for different fixed arms length L_c in Floquet's simulation.

It is obvious from fig. 4. 21. that the phase ranges obtained are all sufficient to implement a panel configuration for the case of config. 2 (from table 4. 1). As the extensions length L_c increases, the phase response of the unit cell becomes more abrupt and the resonant state of the unit cell is achieved at lower lengths L . The unit cells are chosen with a starting phase offset $\phi'_{\Gamma_1} = 53^\circ$ as shown in fig. 4. 21. with a phase increment $\gamma = 120^\circ$ between adjacent unit cells.

Fig. 4. 22. presents radiated field results for panels with different extensions L_c using the same studied scenario in section 4. 2. C. (total panel's length $L_t = 9T_y$).

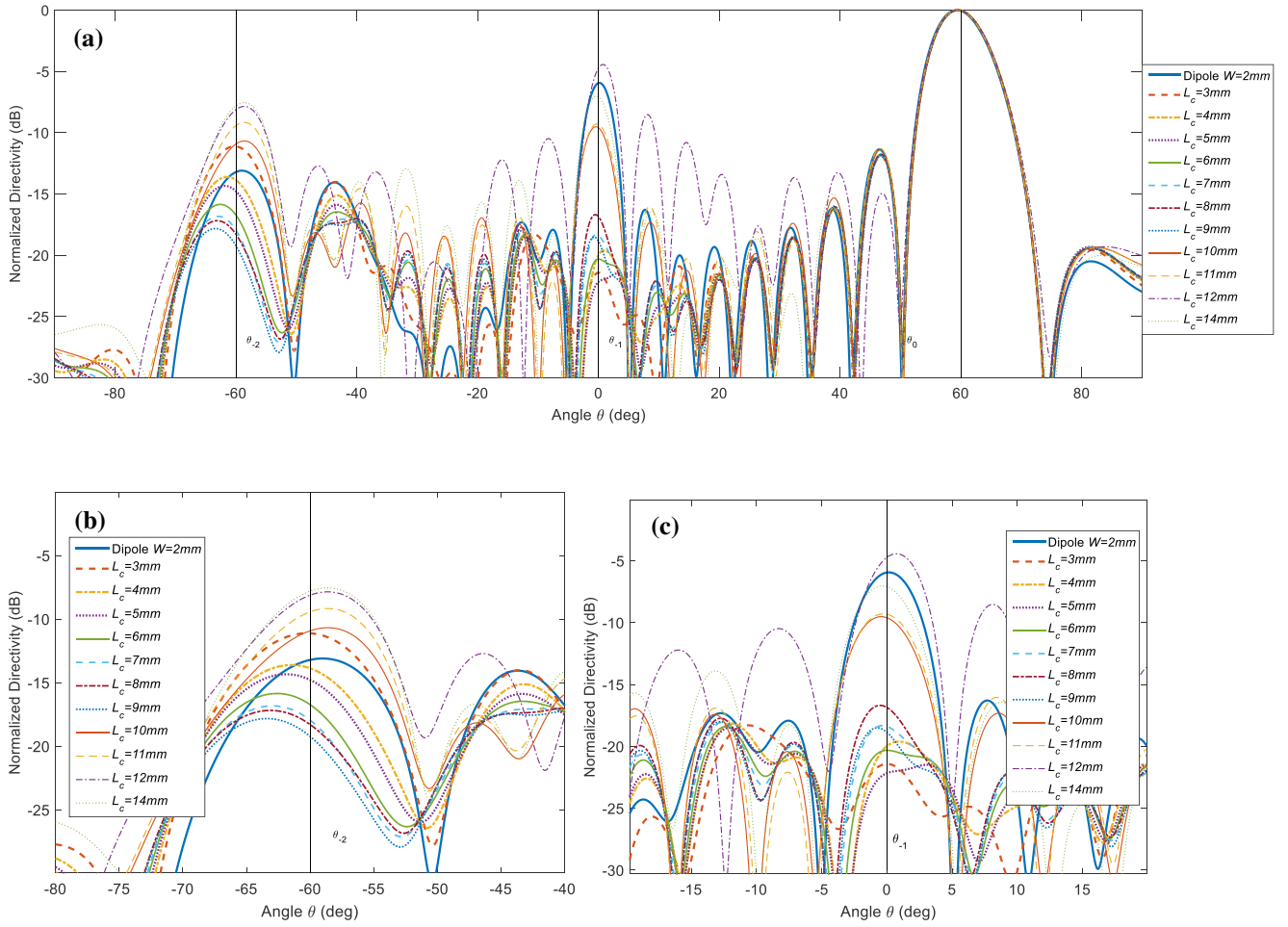


Figure 4. 22. Normalized Radiated field cut (along yz plane) using a panel containing 3 unit cells per T_y and $L_t = 9T_y$ (a) with a close up at the reflection θ_{-2} (b) and specular reflection θ_{-1} (c).

It is shown, from fig. 4. 22., that all results yield a main lobe in the desired direction at θ_0 . On the other hand, it is evident that introducing extensions with lengths L_c has a big impact over the harmonic lobe levels when compared with panels implemented with dipole elements. As soon as $L_c = 3mm$ is introduced to the elements, we obtain $HLL = -21dB$ at θ_{-1} and $HLL = -11.5dB$ at θ_{-2} . Then, higher L_c values yield lower HLL specifically at θ_{-2} . For $L_c = 9mm$ we obtain $HLL = -18dB$ at θ_{-2} .

Conversely, when $L_c \geq 10mm$ HLL levels start to elevate once again (for $L_c = 14mm$ we obtain $HLL = -7dB$ at θ_{-1} and θ_{-2}). This can be explained by the fact that for $L_c \geq 10mm$, the reflection phase response of unit cells becomes ultra-sensitive to their geometrical control parameter (their length L) as shown in fig. 4. 21. Having high sensitivity, such cells are more prone to high phase state errors over the panel even in numerical simulations. In fact, the meshing process, used in our simulations, is allowed to increase the mesh size up to $1mm$ in order to reduce the computation burden.

It is important to remind here that the panel's reflection performance is linked to the applied phase distribution (which in turn depends on the accuracy of cell description). So a small

deviation in geometry (due to mesh inaccuracy) may result in a significant phase error for cells with non-smooth phase response. Such a phase error will be periodically reproduced over the panel and in turn specifically affects HLL.

In conclusion, different parameters should be regulated in order to obtain low HLL (as discussed in each of the sub-sections). A more quantitative analysis that unifies those parameters will be addressed in the next section.

4. 4. Relation between Harmonic Lobe Levels, the Phase Sensitivity and Resonance of the unit cell

4. 4. A. Proposed metrics

As shown in the previous sections 4. 2 and 4. 3., it is hard to be able to predict the Harmonic lobe levels that result from a panel configuration with sub-wavelength unit cells. Those levels depend on many different factors, including the methodology of implementation for the panel configuration, the shape and the dimensions of the element and the positioning of the resonant state of the unit with respect to its dimensions.

So, to better synthetize the results obtained in the previous sections, two metrics are introduced. The aim is to propose metrics that permit to quantify all of the mentioned variations that affect the harmonic lobe levels. The final goal is to try to derive design rules so that minimal HLL can be obtained for a given configuration. Such design rules will be defined so that HLL are lower than the designer's given threshold ($< -13.5\text{dB}$).

First, the phase sensitivity S of the cell at resonance is introduced since it is supposedly related to HLL as discussed in section 4. 3. A. It can be calculated as the derivative of the phase response with regards to the control parameter:

$$S(L_0) = \frac{d\phi_\Gamma}{dL}(L_0) \quad (4-10)$$

where L_0 is the value of the element's control parameter at resonance (here the dipole's length L as an example).

It is well known that a unit cell's phase response is most highly sensitive at its resonance. So, S is computed for all configurations simulated in the previous sections (those presented in figs. 4. 10, 4. 14 and 4. 21).

Second, the ratio between the element's control parameter value at resonance and the unit cell's dimension is introduced (since it was related to HLL in section 4. 3. C.) as follows:

$$R = \frac{L_0}{d} \quad (4-11)$$

4. 4. B. Simulation Settings

Different element types are used in the process. For the sake of unifying of the results, we retake the simulations conducted earlier in this chapter (in section 4. 2. and sub-section 4. 3. A.) for the same phase offset $\phi'_{r_1} = 53^\circ$. For completeness, we also add those of sub-section 4. 3. C. and new simulation results obtained with other elements (without detailing their procedures since they follow the same steps used in previous sections):

- An H dipole with L being its control parameter, extensions length $L_c = 8mm$ and for different widths W are used for each simulated panel.
- Slotted square patch elements (which is considered as another form of miniaturizing the dipole element), as illustrated in fig. 4. 23., length L being its control parameter and different thicknesses t are used for each simulated panel.

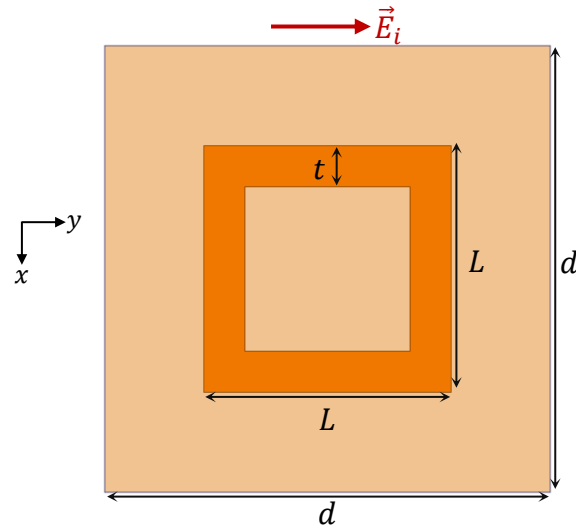


Figure 4. 23. Illustration of the simulated unit cell (Top View) using slotted square patch element. Incident E-field along $+y$.

4. 4. C. Simulation Results

The maximum level of the Harmonic lobes (from θ_{-1} and θ_{-2} since both are considered as parasitic lobes and affect the directivity of the panel in the desired direction) is determined in function of the metrics introduced in eqs. (4-10) and (4-11). Fig. 4. 24. plots the maximum HLL for different panels considering 3 unit cells per T_y and 4 units cells per T_y in fig. 4. 25.

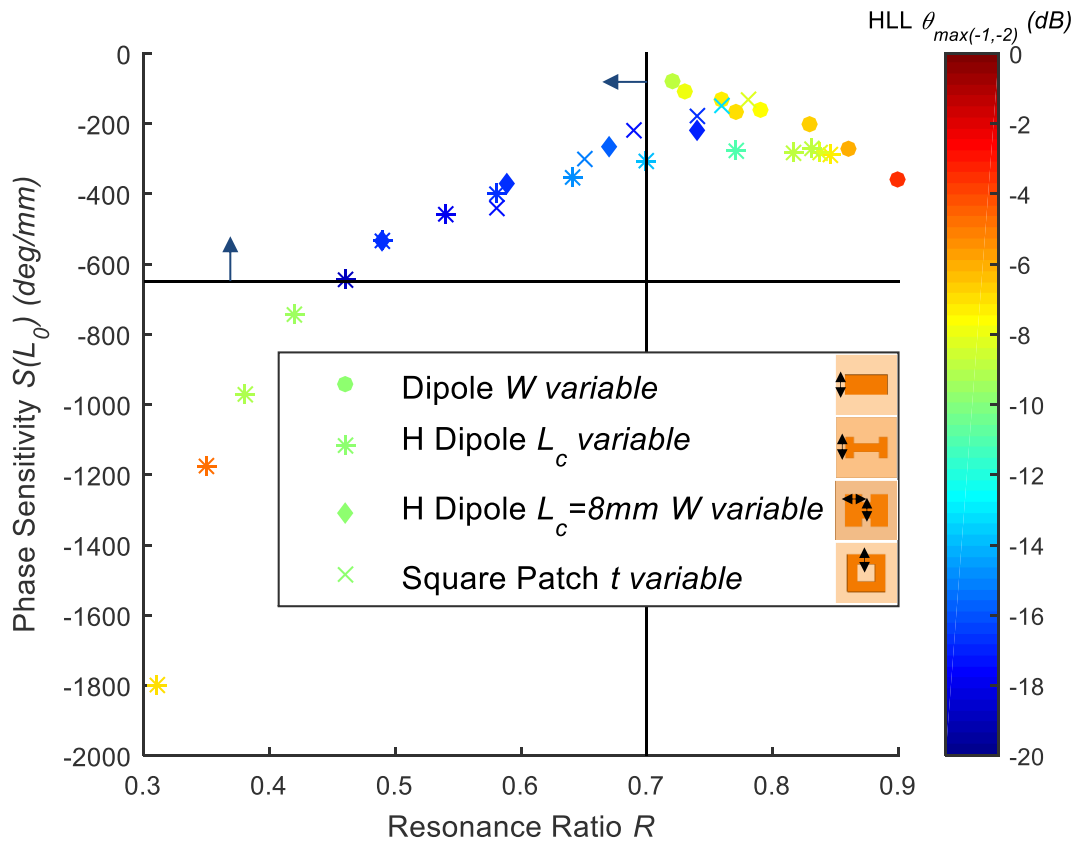


Figure 4. 24. Maximum Harmonic Lobe Levels (HLL) in terms of the unit cell's resonance ratio R and their phase sensitivity $S(L_0)$ for panels using 3 unit cells per T_y with $L_t = 9T_y$.

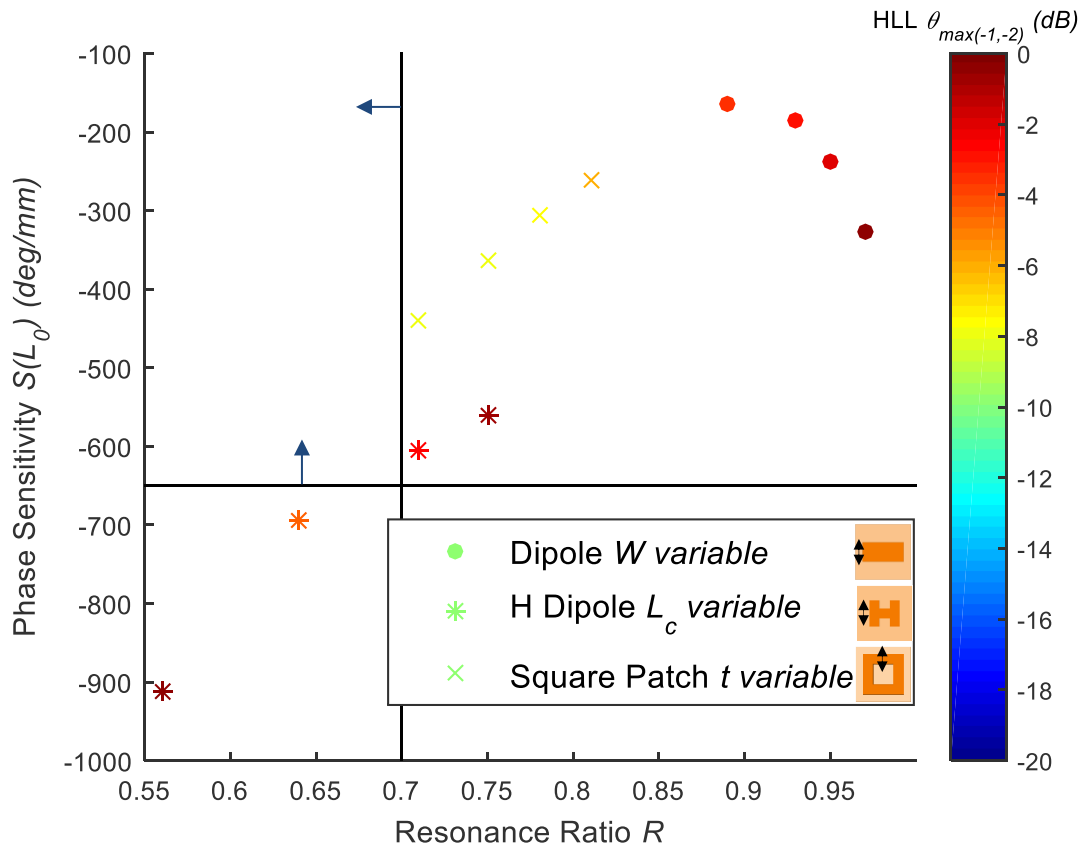


Figure 4. 25. Maximum Harmonic Lobe Levels (HLL) in terms of the unit cell's resonance ratio R and their phase sensitivity $S(L_0)$ for panels using 4 unit cells per T_y with $L_t = 9T_y$.

It is evident, from fig. 4. 24., that panels (including any element type) with harmonic levels lower than -13.5dB reside in one specific region. This region suggests both metrics have to comply with given thresholds simultaneously. Indeed, the ratio R has to be kept lower than 0.7, which means the resonance has to occur for element lengths not too close to the cell dimensions. In the meantime, $|S|$ has to be kept lower than $650^\circ/\text{mm}$, which means the phase response must be smooth enough. As a conclusion, it seems a good element is one with a smooth resonance occurring for a quite small length (compared to the cell size).

Going beyond those limitations causes the panel to host a periodic error and elevate once more the harmonic lobe levels. This error is due to either the high phase sensitivity of the unit cells or to the close spacing between the elements.

For specific element types, the slotted square patch or the H dipole for example, low side lobe levels are even obtained at $R = 0.74$. For generality of the limitations and to include all element types, we rule out those cases.

It is shown in fig. 4. 25., that none of the element types are able to attain the region delimited by $R \leq 0.7$ and $|S| \leq 650^\circ/\text{mm}$ when using 4 unit cells per T_y . Therefore, none of the configurations achieve HLL levels lower than -13.5dB . Furthermore, taking the slotted square patch panel as an example, we are not able to carry on with simulations that enter the prescribed region since its phase range becomes smaller than that needed for the phase distribution of the given configuration.

4.5. Conclusion

A reflection analysis for semi-infinite SIM panels is conducted in this chapter. Theoretical directions for Floquet's harmonics are determined. Additionally, these directions are verified with simulations using HFSS. Radiated far field parasitic lobes confirm the directions obtained in the theoretical analysis.

A practical implementation is introduced for the SIM panels. Simulations for semi-infinite practical panels also confirm the existence of radiated parasitic lobes along with the desired main lobe. They also confirm different degrees of freedom are available to control parasitic lobes.

Effects of changing the unit cell dimensions and thus the number of elements used along with the phase offset on the overall performance of the panel are discussed. The miniaturization technique of the unit cell's element showed promising results when related to the mitigation of the harmonic lobe levels. Though this technique is limited by the implementation technology (ultra-sensitive unit cells are to be avoided).

New metrics that give design rules to get minimal harmonic lobe levels are introduced. Mainly, these are related to the phase sensitivity of the unit cell along with the resonance ratio. Specific criteria should be met for those metrics in order to attain the desired performance of the panel and minimize the errors of the implemented reflection phase distribution (defined by $R \leq 0.7$ and $|S| \leq 650^\circ/mm$). These criteria are specific to the desired reflection configuration.

In the next chapter, we will introduce a generalized Surface impedance modulation that might be the solution to overcome these criteria. Generalized SIM introduces magnitude and reflection phase distributions over the panel in order to mitigate harmonic lobes levels.

Chapter 5 - Generalized Surface Impedance Modulation for Perfect Control of the reflected fields

It is evident, by now, that widespread research is being conducted on artificial impedance surfaces [69]. Many new paradigms and applications have been presented in this specific domain. One of them is to allow controlling the reflection from an illuminated surface, which demonstrated significant interests in many domains namely antenna and radar applications [70]. The principle is to get out of the conventional reflection law and it consists in managing only the local reflection phase over the surface of a panel. This classical approach relies solely on the modulation of pure imaginary surface impedances [72-75] and as demonstrated in chapter 4 of this manuscript.

The theory has been formalized as the generalized law of reflection [27]. It is mostly suitable for holographic antenna applications specifically reflectarrays [62] and leaky wave antennas [65]. However, it suffers from parasitic reflections in unwanted directions due to the periodic nature of the required impedance modulation that generates Floquet harmonics (also discussed in chapter 4). This was recently explored in [75] where the authors demonstrated that power conservation requires the use of a complex surface impedance to control both the magnitude and phase of the local reflection.

In this chapter, we propose another formulation also relying on power conservation. We introduce a new parameter which can be interpreted as the global reflection coefficient. This additional degree of freedom can be tuned to certain extents in order to optimize the performance of the SIM panel.

We also propose a practical scenario that implements the generalized formulation by tuning this global reflection coefficient. It uses elements printed on two layers to control the magnitude and phase of the local reflection over the panel. It is compared with a chosen configuration from chapter 4 that yielded high parasitic levels due to the impossibility to respect the phase sensitivity and resonance limitations.

This chapter is divided into 4 sections. In the first section, a new theoretical relation is derived so that the required reflection coefficient over a SIM panel reradiates in the desired direction. In section 5. 2., simulations are carried out to show the impact of the global reflection coefficient on harmonic lobe levels. A comparative study between different formulations is also conducted. Section 5. 3. presents a potential scenario that implements the generalized SIM over a panel using practical unit cells. A comparative study is also conducted for practical panels implementing different SIM methodologies. Last, section 5. 4. provides the verdicts and some perspectives to expand the findings of this chapter.

This chapter relies solely on Full wave simulations over ANSYS® HFSS® to validate the theoretical part.

5. 1. Theoretical analysis

In this section, we analyze the conditions that need to be imposed on a SIM reflective panel if we consider a scenario where an incident plane wave hits its surface and a reflected plane wave is desired in a prescribed direction. Conditions for power conservation along the process are discussed. A new parameter that controls the reflected power is presented. It must be emphasized that this theoretical formulation is more general than the one used in previous chapters. In those ones, we only considered the required condition for phase. Here, we used a more complete approach, in which we enforce both the incident and reflected fields are homogeneous plane waves.

5. 1. A. Variation of the surface impedance

The studied scenario, that represents a SIM panel in free space, is depicted in fig. 5. 1. A plane wave (TM polarized) propagating with an incident angle θ_i impinges on the panel lying along the Oy axis. A variable surface impedance $Z_s(y)$ is assumed along the panel.

The incident field is expressed as:

$$\vec{E}_i = E_0 e^{-jk_0 (y \sin \theta_i - z \cos \theta_i)} (\cos \theta_i \vec{a}_y + \sin \theta_i \vec{a}_z) \quad (5-1)$$

$$\vec{H}_i = \frac{E_0}{\eta_0} e^{-jk_0 (y \sin \theta_i - z \cos \theta_i)} \vec{a}_x \quad (5-2)$$

with η_0 and k_0 the free space impedance and wavenumber.

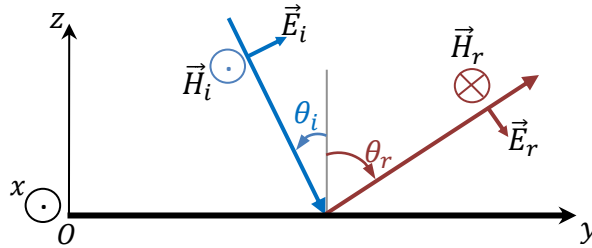


Figure 5. 1. General configuration of a SIM panel within free space.

We now derive the condition on Z_s so that the reflected field is imposed as a plane wave propagating in a specific desired direction with a reflection angle θ_r . We thus assume the reflected field complies with the following form:

$$\vec{E}_r = \Gamma_G E_0 e^{-jk_0 (y \sin \theta_r + z \cos \theta_r)} (\cos \theta_r \vec{a}_y - \sin \theta_r \vec{a}_z) \quad (5-3)$$

$$\vec{H}_r = -\frac{\Gamma_G E_0}{\eta_0} e^{-jk_0 (y \sin \theta_r + z \cos \theta_r)} \vec{a}_x \quad (5-4)$$

where $\Gamma_G = |\Gamma_G| e^{+j\phi}$ is a complex constant standing for the global reflection coefficient over the panel. The tangential components of the total fields over the panel ($z = 0$) are determined as follows:

$$E_y = E_0 [e^{-jk_0 (y \sin \theta_i)} \cos \theta_i + \Gamma_G e^{-jk_0 (y \sin \theta_r)} \cos \theta_r] \quad (5-5)$$

$$H_x = \frac{E_0}{\eta_0} [e^{-jk_0(y \sin \theta_i)} - \Gamma_G e^{-jk_0(y \sin \theta_r)}] \quad (5-6)$$

They have to comply with the impedance boundary condition:

$$E_y = -Z_s H_x \quad (5-7)$$

The required surface impedance $Z_s(y)$ over the panel can then be derived as:

$$\frac{Z_s(y)}{Z_{TM}} = \frac{1 + |\Gamma_G| \frac{\cos \theta_r}{\cos \theta_i} e^{-j[k_0 y (\sin \theta_r - \sin \theta_i) + \phi]}}{1 - |\Gamma_G| e^{-j[k_0 y (\sin \theta_r - \sin \theta_i) + \phi]}} \quad (5-8)$$

5.1.B. Power Conservation Model

Consider a segment with a unit length along the panel, as shown in fig. 5. 2. The incident power flows in a window whose width is $\cos \theta_i$ while the reflected power flows within a window whose width is $\cos \theta_r$. The magnitude of Γ_G is chosen to comply with power conservation.

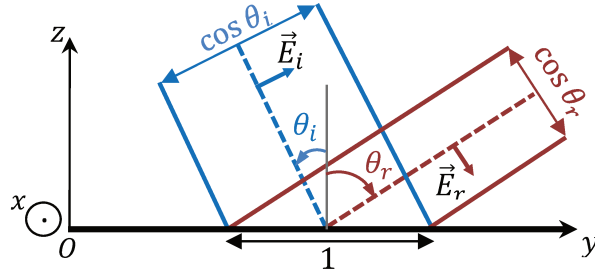


Figure 5. 2. Incident and Reflected waves for power conservation model.

Calculating incident and reflected Poynting vectors from (5-1) to (5-4) and equalizing incident and reflected powers in the unit window, leads to the following:

$$\frac{|E_0|^2}{\eta_0} \cos \theta_i = \frac{|\Gamma_G|^2 |E_0|^2}{\eta_0} \cos \theta_r \quad (5-9)$$

Consequently, for power conservation the following condition in (5-10) should be met:

$$|\Gamma_G| = \sqrt{\frac{\cos \theta_i}{\cos \theta_r}} \quad (5-10)$$

and in turn, the surface impedance in eq. (5-8) that respects the power conservation becomes:

$$\frac{Z_s(y)}{Z_{TM}} = \frac{1 + \sqrt{\frac{\cos \theta_r}{\cos \theta_i}} e^{-j[k_0 y (\sin \theta_r - \sin \theta_i) + \phi]}}{1 - \sqrt{\frac{\cos \theta_i}{\cos \theta_r}} e^{-j[k_0 y (\sin \theta_r - \sin \theta_i) + \phi]}} \quad (5-11)$$

Eq. (5-11) actually matches the ones obtained in [59, 60, 75, 78]. However, the derivation process is different. In our case, power conservation relies on the introduction of a single global parameter $|\Gamma_G|$. As we will see later in this chapter, it may offer a simple and convenient degree of freedom to control the reflection phenomenon from a SIM panel.

5.2. Numerical analysis

In the previous section, we formulated a generalized expression for the surface impedance over a reflecting SIM panel. It depends on the incident and reflected angles for a given configuration along with a global reflection coefficient that regulates the amount of reflected power from the panel. In this section, for a given configuration, different surface impedance distributions are implemented over a semi-infinite panel and compared in the far field regime. The goal here is to find a generalized distribution that is able to mitigate parasitic lobe levels due to the periodicity of the classical impedance distribution (discussed in chapter 4).

5.2.A. Semi Infinite SIM Panel settings and Impedance Distributions

In the numerical implementation, the variation of $Z_s(y)$ is discretized over the panel, which means the panel is divided into I elements with different surface impedances Z_{si} . The details of this procedure were already discussed in chapter 4 (sub-section 4.1.B.i.). The given configuration is for an incident angle $\theta_i = 0^\circ$ and a reflected angle $\theta_r = 60^\circ$. The spatial period also remains the same as in eq. (4-3) with $T_y = 1.15\lambda_0$ in this particular case. The total length of the panel is $L_t = 9T_y = 10.36\lambda_0$ at $f = 8GHz$. The number of elements $I = 36$, and the length of each element is $d = 0.288\lambda_0 = 10.8mm$ corresponding to 4 elements per period T_y .

The surface impedance Z_{si} for each element i over the panel is calculated using (5-11) and plotted in fig. 5.3. In that case, power conservation leads to $|\Gamma_G| = 1.41$. For comparison, another distribution corresponding to the specific case where $|\Gamma_G| = 1$ is given. It must be highlighted that this configuration is obtained from (5-8) and it does not comply with power conservation. For completeness, we also compare with the classical distribution that is classically used for metasurfaces [60, 76, 77] and many other antenna applications (introduced since chapter 4 (in eq. 4-9)). If we were to compare eq. (5-11) with (4-9), both distributions yield periodic variations along the panel due to their geometrical dependence to the incidence and reflection angles. On the other hand, it is important to remind that (4-9) enforces a pure imaginary X_{si} distribution while (5-11) yields complex impedances with two different distributions for the real part R_{si} and the imaginary part X_{si} as shown in fig. 5.3.

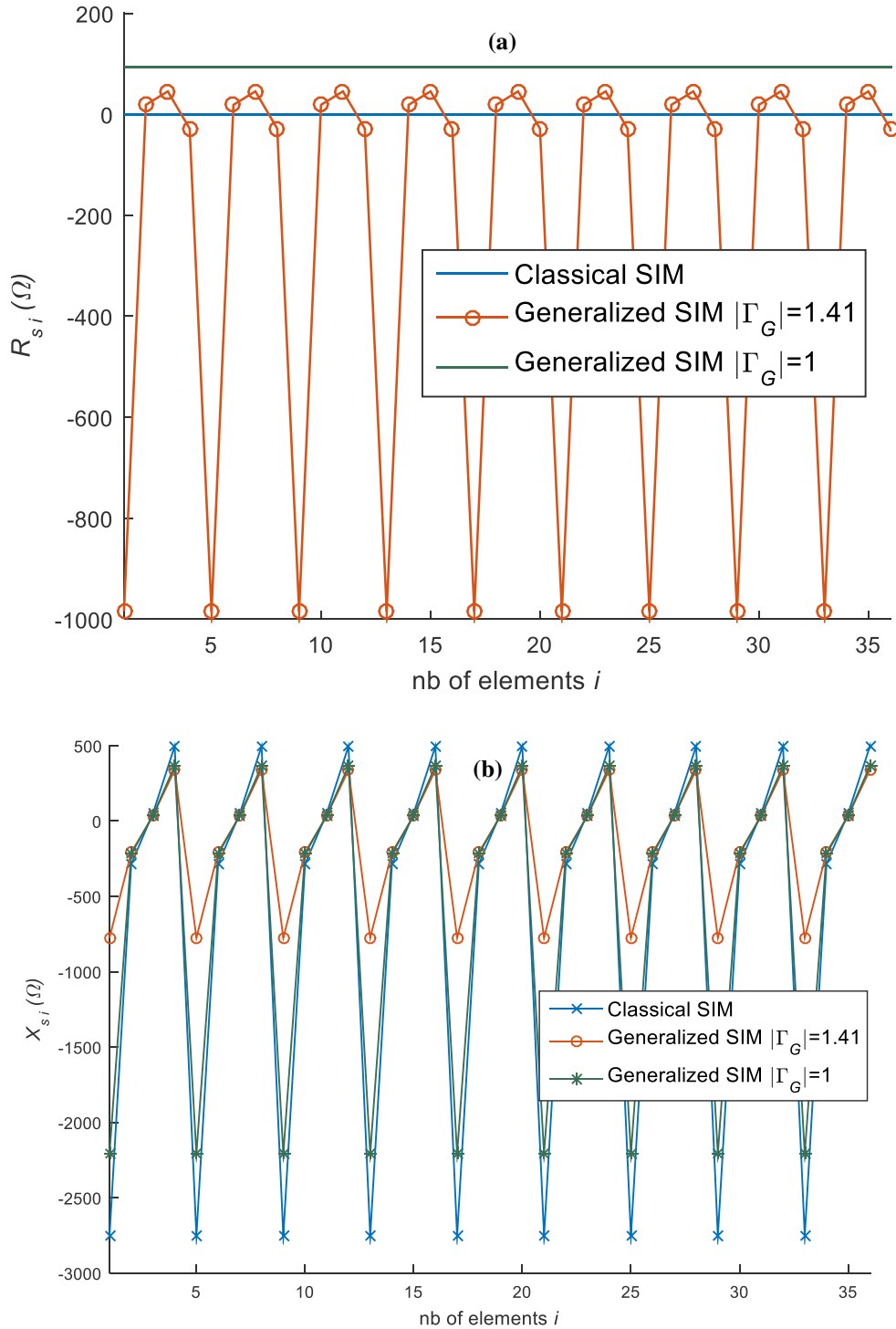


Figure 5. 3. Values of the real (a) and imaginary (b) parts of Z_{si} over the panel for $\{\theta_i = 0^\circ; \theta_r = 60^\circ\}$.

As can be seen from fig. 5. 3., the imaginary parts (from fig. 5. 3. (b)) all exhibit the same periodicity with less pronounced variations for the conservative case ($|\Gamma_G| = 1.41$). This means that SIM panels that implement all three of those distributions are prone to the appearance of Floquet's harmonic lobes.

More differences can be observed in the real parts (Fig. 5. 3. (a)). The conservative case shows large and periodic variations for the real part, with both positive and negative values.

This is fully consistent with the interpretation given in [76] that stipulates that power is balanced between lossy and active zones when reflected over the panel.

On the contrary, the case where $|\Gamma_G| = 1$ corresponds to a constant and positive real part which suggests a lossy configuration. Finally, the classical case corresponds to the situation where the real part is zero everywhere, only requiring reactive elements over the reflective panel.

5.2.B. SIM Simulation Results

Radiated far field results are shown in this sub-section for the same intended panel configuration using the different formulations. The surface impedance distributions used for each of the panels are those introduced in fig. 5.3. The obtained far field lobes directions are compared with their theoretical directions from eq. (4-5).

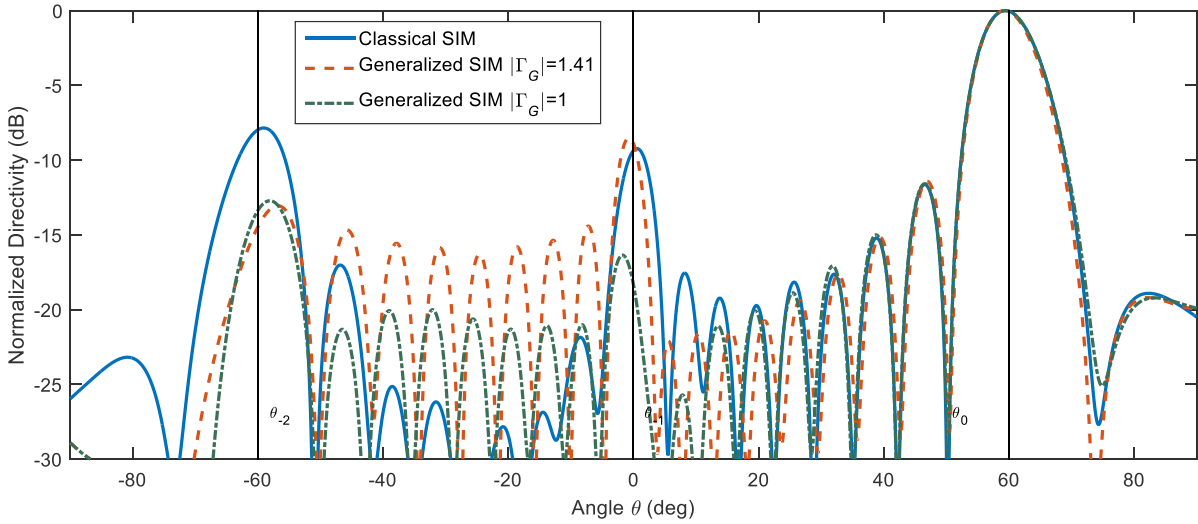


Figure 5.4. Normalized Radiated far field, E-plane cut (along yz), for the classical SIM distribution and Generalized SIM distributions with two different $|\Gamma_G|$. The vertical black lines represent the analytical directions for each harmonic lobe.

All configurations yield a radiated main beam in the desired direction ($\theta_r = \theta_0 = 60^\circ$). This demonstrates both generalized Z_s distributions of (eq. (5-8) with $|\Gamma_G| = 1$ and that of eq. (5-11)) along with the classical distribution comply with the desired redirection of the reflected beam.

The theoretical directions (vertical black lines) fit pretty well the lobes we observe in fig. 5.4. It is important to highlight that these parasitic lobes are particularly high for the classical distribution (-9.5dB at θ_{-1} and -7dB at θ_{-2}).

Alternatively, it appears the proposed generalized distribution with $|\Gamma_G| = 1.41$, as formulated in (5-11), mitigates mainly one of the parasitic lobes (-13.5dB at θ_{-2}) but not so much the other delimited as the specular reflection (-8.5dB at θ_{-1}). These HLL variations are mainly due to the introduction of a magnitude distribution (also periodic) with active and lossy elements over the panel.

Finally, the case $|\Gamma_G| = 1$ is particularly interesting since it involves a constant and positive resistive loading as shown from fig 5. 3., which can be easily implemented in practice (this will be discussed in the next section). This case demonstrated mitigation of both HLL when compared to other distributions (-16.5dB at θ_{-1} and -13dB at θ_{-2}). These HLL attenuations can be related to the additional losses introduced over the panel.

In the next section, we will demonstrate a practical scenario, where the lossy $|\Gamma_G| = 1$ distribution affects only the parasitic lobe levels while preserving the same radiated level for the main lobe (at the desired direction of reflection) when compared to that of a practical panel that implements the classical distribution.

5.3. Practical Analysis

In this section, a practical implementation of the generalized SIM formulated in eq. (5-8) with $|\Gamma_G| = 1$ is presented using a new type of unit cell. Such unit cell should be able to regulate the magnitude and phase of the reflection coefficient. A semi-infinite panel that realizes such control over the reflection coefficient is simulated with HFSS and compared with one of the panels that implemented classical SIM and had high HLL.

5.3.A. Studied Configuration and Practical Panel Settings

It was demonstrated in 5. 2. B. that using eq. (5-8) with $|\Gamma_G| = 1$ added resistive losses to the panel and in turn produced a decrease in all HLL levels when compared to a classical SIM panel and the generalized panel with $|\Gamma_G| = 1.41$ for the given configuration $\{\theta_i = 0^\circ; \theta_r = 60^\circ\}$.

To practically implement a SIM panel with added losses over its elements, we start by determining the local reflection coefficient distribution (in magnitude and phase) for each of its unit cells. It can be inherently calculated from its corresponding impedance distribution Z_{si} using eq. (5-12):

$$\Gamma_L = \frac{Z_{si} - 1}{Z_{si} + 1} \quad (5-12)$$

In fig. 5. 5., the desired local magnitude and phase reflection distributions are plotted. For comparison, we present once again the reflection coefficient distribution for the classical SIM case.

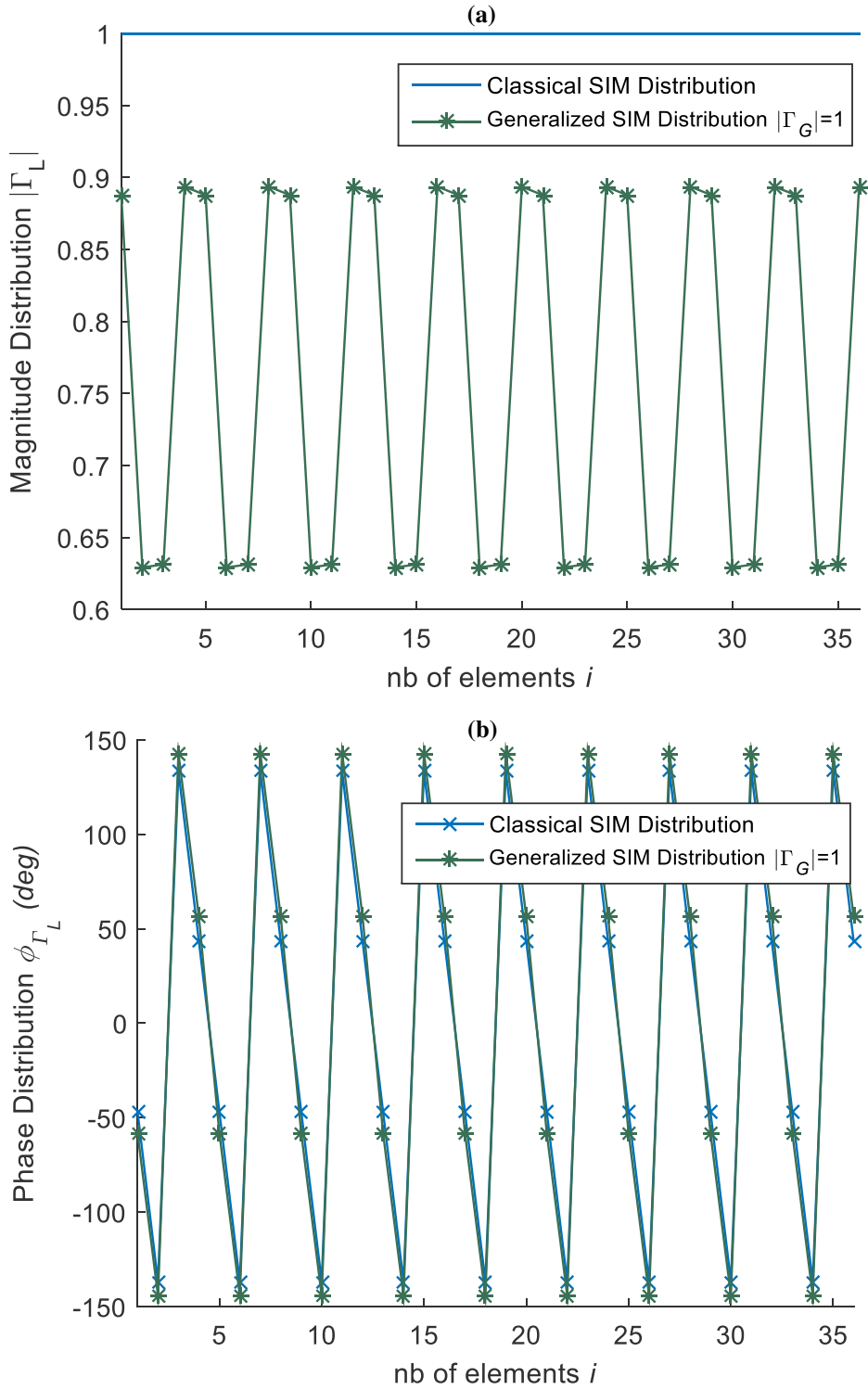


Figure 5.5. Magnitude (a) and phase (b) local reflection coefficient distributions needed over the practical panel.

Fig. 5.5. (a) Shows that the generalized SIM distribution with $|\Gamma_G| = 1$ yields a periodic distribution of magnitudes for the local reflection coefficient $|\Gamma_L|$ lower than 1 conversely to what is obtained for the classical SIM distribution. This proves that such unit cells should have controlled local losses as discussed earlier in section 5.2.A.

On the other hand, from fig. 5.5. (b), it is shown that generalized SIM reflection phase only slightly deviates (no more than 12°) from its classical counterpart.

One of many ways to implement those local losses ($|\Gamma_L| < 1$) over a practical panel, is a configuration which allows a fraction of that incident power to flow across the panel instead of being reflected. This “transmission loss” is illustrated by the red arrows in Fig. 5. 6. (as opposite to the reflected power illustrated by the blue arrows). This transmitted power insures that the magnitude of the local reflection coefficient is smaller than 1.

The methodology chosen to implement this principle consists of double printed metallic elements separated by a dielectric layer as illustrated in the same figure. In other words, the reflecting panel does not involve any ground plane anymore, which effectively prevent from total reflection.

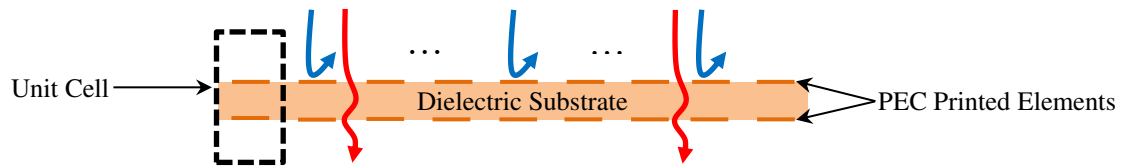


Figure 5. 6. Illustration of a Practical Generalized SIM Panel (Cross Section View). (The reflected power is presented in blue arrows; Transmitted power in red arrows).

5. 3. B. Reflection Response of the Unit Cell

The elements used on both sides of the unit cell are slotted square patches as illustrated in fig. 5. 7. As chosen in chapter 4, the dielectric substrate used is the “Cuclad 5880” with a relative permittivity $\epsilon_r = 2.17$ and height $h = 0.0426\lambda_0 = 1.6mm$.

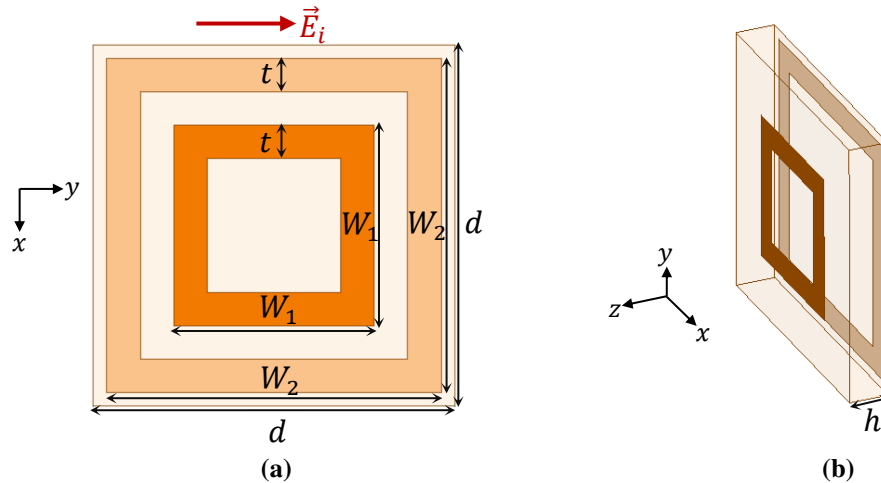


Figure 5. 7. Illustration of the simulated unit cell Top View (a) 3D view (b) using slotted square patch elements; Incident E-field along +y.

In this unit cell, we fix the thickness $t = 2mm$ for both square patch elements while varying their widths (W_1, W_2) independently. These are the control parameters of this unit cell. Such degrees of freedom permit the control of both the magnitude and phase reflection responses in infinite periodic simulations.

Fig 5. 8. plots the obtained magnitude and phase responses of the double slotted square patches unit cell as a function of W_1 and W_2 .

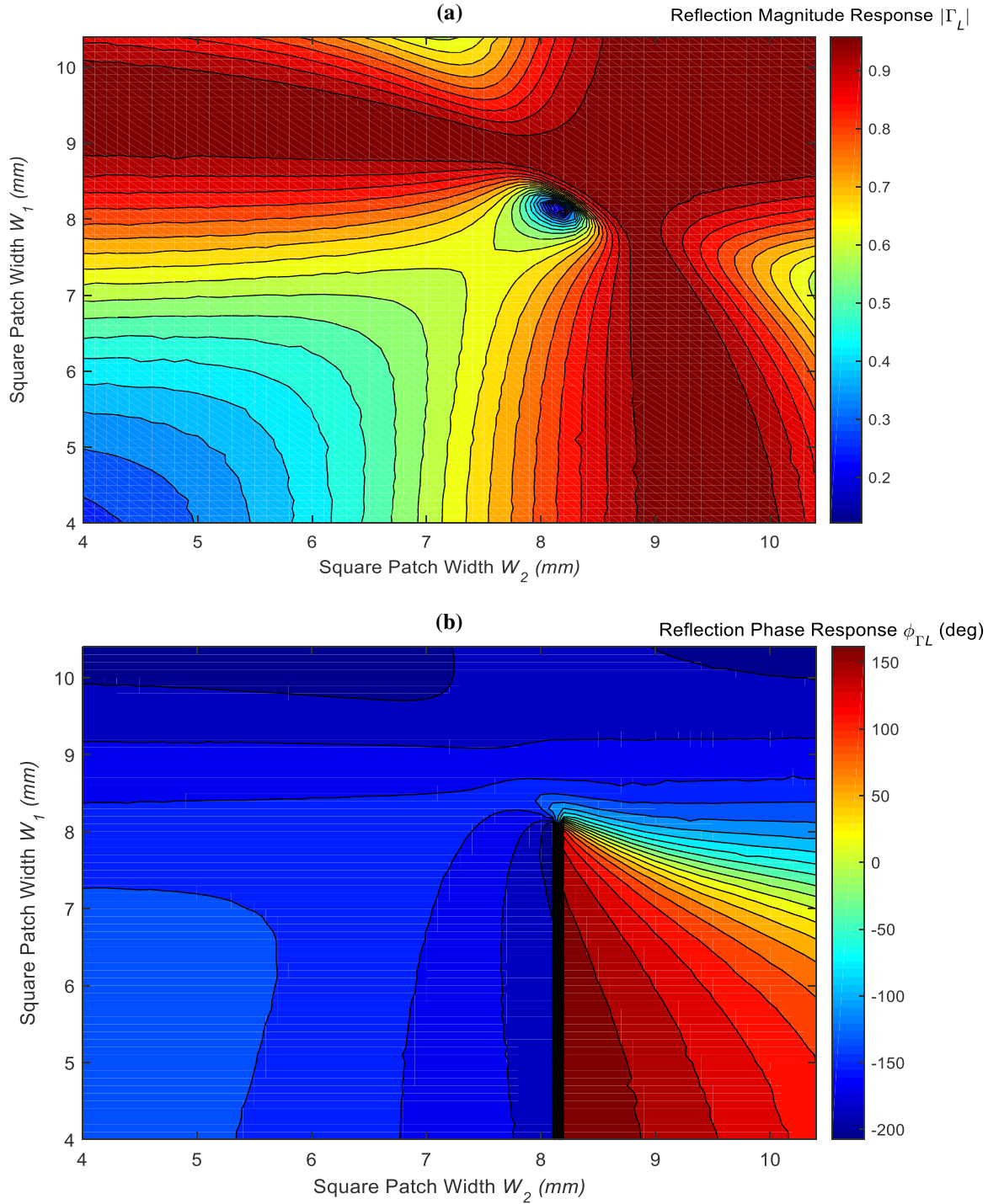


Figure 5. 8. Magnitude (a) and phase (b) reflection response obtained for the unit cell in infinite periodic environment.

It is shown from fig. 5. 8. (a), that the magnitude response of such a unit cell varies between $0.1 \leq |\Gamma_L| \leq 1$. It is also observed that the magnitude $|\Gamma_L|$ drops significantly at the resonance for $W_1 = 8.2$ mm and $W_2 = 8.2$ mm.

A phase range $\phi_{\Gamma_L} = [-200^\circ; 160^\circ]$ is obtained in fig. 5. 8. (b). It is important to point out here that the magnitude and phase response are associated together with the control parameters of the simulated unit cell. Both should be fulfilled in order to correctly implement the reflection distribution that utilizes the generalized SIM with $|\Gamma_G| = 1$.

The cells chosen from fig. 5. 8. are those that satisfy both the intended magnitude and phase reflection distributions at the same time (fig. 5. 5.). The element widths (W_1, W_2) are presented in table 5. 1.

Table 5. 1. Unit Cell Parameters used for the simulated Configuration of a panel with Generalized SIM distribution with $|\Gamma_G| = 1$.

Needed Unit Cell Reflection Coefficient Γ_L from fig. 5. 5.		Element Control Parameters		Implemented Unit Cell Reflection Coefficient Γ_L from fig. 5. 9.	
Magnitude Response $ \Gamma_L $	Phase Response $\phi_{\Gamma_L} (deg)$	Top Element Width $W_1 (mm)$	Bottom Element Width $W_2 (mm)$	Magnitude Response $ \Gamma_L $	Phase Response $\phi_{\Gamma_L} (deg)$
0.88	-58	7.8	9.3	0.9	-58.7
0.62	-144	7.4	6.6	0.633	-143.5
0.63	143	7.7	8.2	0.61	146.4
0.89	56	7.1	9.5	0.9	56.4

From table 5. 1., we can clearly determine that the chosen control parameters for the double square patch elements do not perfectly match those needed for the given configuration. Consequently, this might deviate to certain extents the realized results for the generalized SIM with $|\Gamma_G| = 1$ from those obtained in fig. 5. 4. In fact, the obtained magnitude and phase reflection response for such parameters are closest to those needed for the implemented generalized reflection law as shown in table 5. 1. It is important to remind here that the magnitude and phase responses need to be correlated for proper realization of such law. Still, those unit cells are implemented in the semi-infinite panel configuration with the spatial period T_y presented in fig. 5. 9.

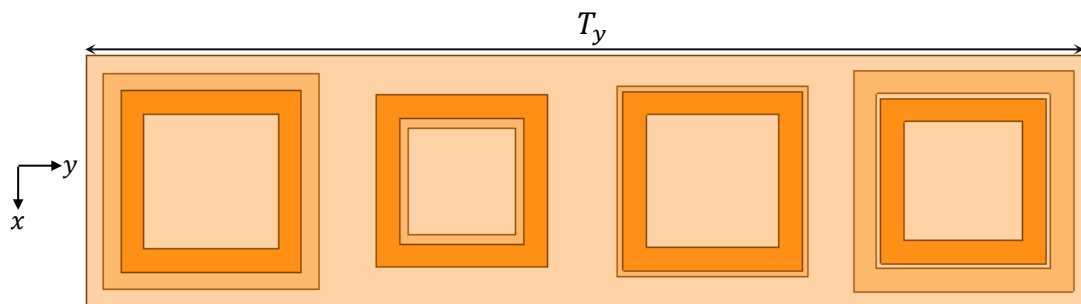


Figure 5. 9. Spatial period T_y (Top View) for the double squared patch panel.

5.3.C. Radiated Field Simulations for Practical Panels

5.3.C.i. Comparison with theory

Radiated far field results are presented in fig. 5. 10. for the same intended panel configuration using different methodologies. One with generalized surface impedance distribution having $|\Gamma_G| = 1$ (cf. fig. 5. 4.) and the other being its practical implementation using double square patches as presented in fig. 5. 9.

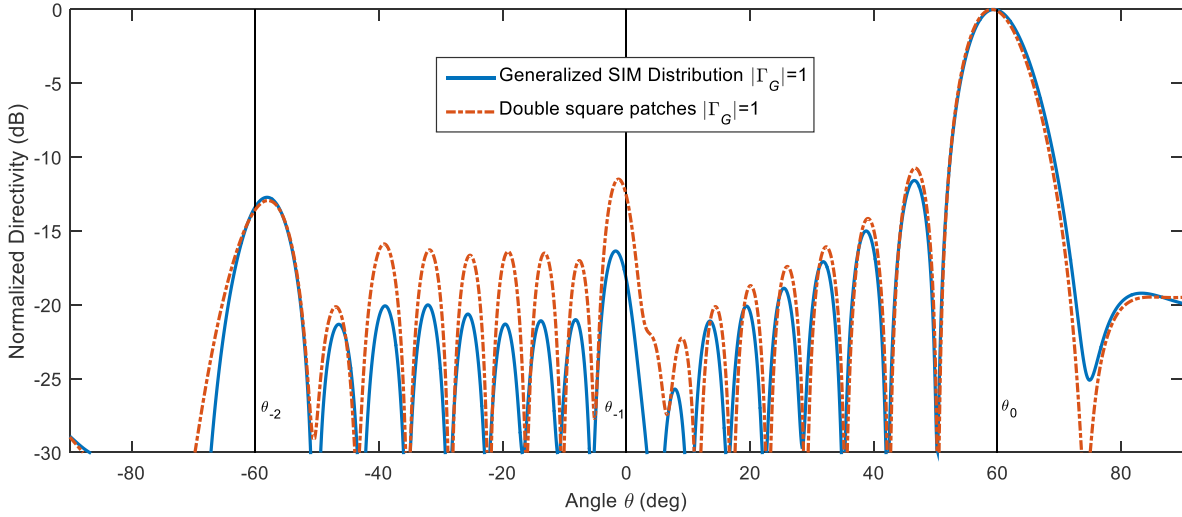


Figure 5. 10. Normalized radiated field E-plane cut (along yz plane) for Generalized SIM panel with $|\Gamma_G| = 1$ (from fig. 5. 4.) and Double Square Patch Panel implementing the same solution (from table 5. 1.).

As expected, from fig. 5. 10., it is shown that the realized practical panel using double square patches yields deviated results since it did not perfectly match the needed magnitude and phase responses for its unit cells (as presented in table 5. 1.). Specifically, the noticeable HLL increase at θ_{-1} from -16.4dB for the generalized SIM panel to -11.5dB for the double square patch panel. Still, it is interesting to compare the radiated fields from such a realization to another panel that implements classical SIM with grounded square patch elements.

5.3.C.ii. Comparison with Classical SIM

Radiated far field E-plane cuts for practical panels are compared here. The directivity levels in such a scenario are computed with HFSS taking into account the dimensions of the simulated panel (a total length $L_t = 9T_y = 10.368\lambda_0$ along the y axis and $d = 0.288\lambda_0$ along the x axis).

For comparison, we use the semi-infinite panel that implemented unit cells using slotted square patches from one side and a ground plane from the other (classical reflection distribution with pure reactive cells discussed in chapter 4). Cross section views for the compared panels are given in fig. 5. 11.

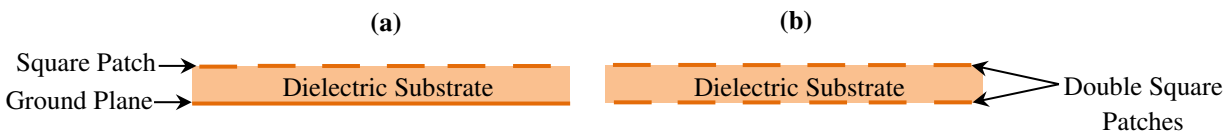


Figure 5. 11. Illustrations (Cross Section Views) of a grounded square patch panel implementing classical SIM (a) and double square patches panel implementing Generalized SIM with $|\Gamma_G| = 1$ (b).

Using 4 unit cells per T_y with $t = 2mm$, the grounded square patch configuration (implementing classical SIM) did not respect the design rules introduced for phase sensitivity and the resonance ratio (discussed in section 4. 4.). It is noteworthy to remind that the configuration simulated, in fig. 5. 12., for the double slotted square patches uses the same number of unit cells per spatial period.

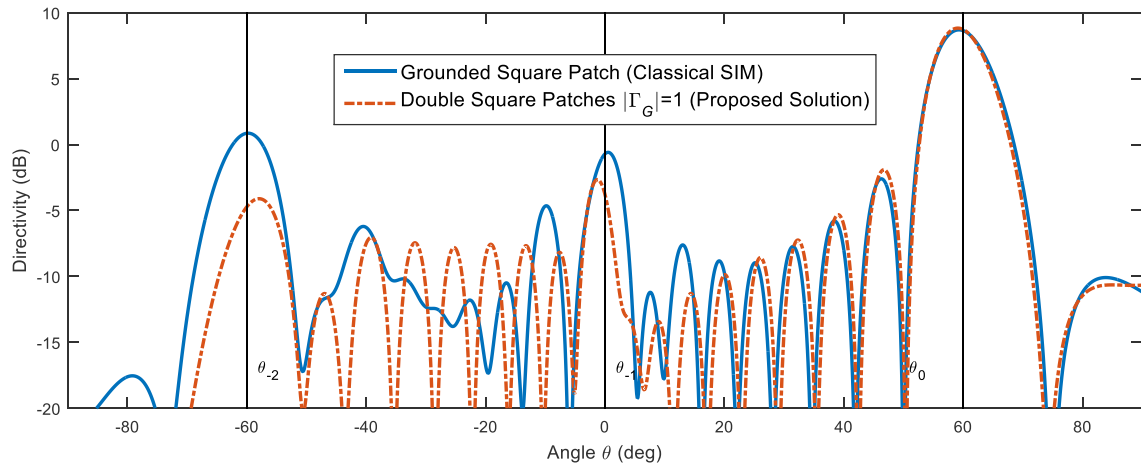


Figure 5. 12. Radiated field E-plane cut (along yz plane) for Grounded Square Patch Panel implementing Classical SIM distribution and Double Square Patch Panel implementing Generalized SIM with $|\Gamma_G| = 1$.

It is shown in fig. 5.12., that the desired reflection is achieved (for $\theta_0 = \theta_r = 60^\circ$). The main lobe level is at 8.7dB for both configurations. This means that a double Square Patch panel does not decrease the directivity level at the desired direction, although it involves no ground plane.

On the other hand, HLL decrease from -0.7dB at θ_{-1} for the grounded square patch panel to -2.7dB for the double square patch panel. At θ_{-2} , HLL decrease from 0.85dB to -4.8dB.

This decrease in HLL can be associated to the magnitude distribution introduced over the panel. The losses hosted by such a distribution, decreases HLL only, without affecting the level of the desired beam.

Though HLL are mitigated to certain extent, the fact that both magnitude and phase distributions are periodic means that reflected parasitic lobes persist and cannot be eliminated completely. This can be further analyzed and considered as a potential solution to improve the design of reflecting panels.

5.4. Conclusion

A new way of deriving SIM on a reflective panel has been proposed to set the direction of the reflected beam. It is done by introducing a global reflection coefficient that also controls the level of reflected power.

Numerical validations have been carried out with full-wave simulations with HFSS® demonstrating the effectiveness of the technique. Comparisons with a classical SIM formulation have also been presented. Due to the impedance periodicity over the panel, both the classical and generalized formulations lead to the excitation of higher order Floquet harmonics in unwanted directions.

It has then been observed that the introduced global reflection coefficient offers a new degree of freedom that can be tuned in order to decrease these parasitic lobes. At a specific value of the global reflection coefficient, the generalized formulation showed advantages in terms of decreasing those parasitic lobe levels.

A potential application of the generalized formulation with a tuned global reflection coefficient has been presented. It suggested using double layered elements to control both magnitude and phase of the reflection distribution over the panel. It eliminated the need of a ground plane for practical reflective panels and showed promise in terms of mitigating parasitic lobe levels.

General Conclusion

The research conducted in this thesis focuses, in its first part, on finding practical solutions to lower the profile of the dihedral corner reflector.

It explores the capabilities of a transformation optic (TO) medium that can be realized in practice. Restricting the TO approach to fill the inner volume of a compressed reflector for the transverse magnetic linear polarization, all dielectric medium using a double layered system is achieved. Though able to attain any compression rate, it is limited by the high anisotropic factor needed that is translated into very high number of dielectric layers that adds complexity to the fabrication process of the reflector.

Surface Impedance Modulation (SIM) is introduced as another solution to flatten the reflector by acting over its surface panels. When combined with the TO medium, SIM is able to relax the constraint associated with the anisotropic factor. Conversely, the TO medium is able to bring closer the RCS performance (at $\theta = 0^\circ$) of the reflector with combined approaches (28.02dBsm) to that of the conventional one (28.2dBsm) when compared with the reflector implementing SIM only (25.2dBsm).

In its second part, this thesis focuses on mitigating the levels of parasitic reflections associated with SIM over a reflecting panel. Those reflections are discussed as being Harmonic lobes due to the periodicity introduced by SIM over the panel. They are verified analytically and using a physical model that implemented discretized surface impedance distribution over a reflective panel. Furthermore, semi-infinite practical panels using printed unit cells with dipoles, patches and miniaturized elements are considered. The reflection response of the conceived panels gives an insight on the source of the parasitic lobes. They show that there is a close relation between the phase sensitivity of the element along with its resonance ratio to mitigate harmonic lobe levels. Limitations based on the simulated database for a given configuration are defined to obtain minimal harmonic lobe levels ($< -13.5\text{dB}$ with respect to the max of the desired main lobe).

Last, a new theoretical formulation for the generalized SIM is introduced. It presents a new parameter called “global reflection coefficient” $|\Gamma_G|$ that delimits power conservation between incidence and reflection from a reflective panel. This parameter gives the ability to regulate the power reflected. For a given configuration that doesn't respect the limitations imposed for the classical SIM, it also provides mitigated levels for the harmonic lobes. A practical scenario applying double slotted square patches over the panel is proposed as a realization of generalized SIM with the tuned global reflection $|\Gamma_G| = 1$. This specific scenario presents lower harmonic lobe levels compared to that implementing classical SIM.

Perspectives

This thesis introduces a simple TO medium that is able to flatten the dihedral corner reflector. It suggests realizing it through the use of a multilayered dielectric system. However, such a fabrication requires a very high number of thin dielectric layers. In literature, there exist many different dielectric mixtures that can be exploited for the same purpose (which might be more practical to realize). One interesting perspective would then be to go further in the fabrication process and to explore the more relevant implementation techniques.

The combination between TO (implemented over a volume) and SIM (over the surface panel) is able to mitigate the inconvenients of both approaches for the dihedral reflector. This combination actually opens up interesting new perspectives towards more realizable EM devices with improved performances. A practical implementation of this methodology can also be discussed and applied for many different applications to further attain its potentials.

This thesis also gave an insight on the relation between the harmonic lobe levels obtained from periodic SIM panels and two new parameters (the phase sensitivity and resonance ratio) of the conceived printed elements. The conducted studies include different elements including printed dipoles, H and slotted square patches which all can be grouped under the passive type. While these studies were able to produce clear limitations to obtain minimal HLL, they are not comprehensive for all element types. Many different elements already used for SIM panels can be also exploited such as multi-resonant elements or even reconfigurable ones.

Moreover, it is evident that all researches on SIM panels consider an incident plane wave. It is interesting to direct those studies towards more concrete applications (e. g. reflect-arrays). In these structures, the impinging wave is produced by a primary source at a given distance from the reflecting panel. The consequence is that the incident wave is no more a plane wave. Then, the panel does not exhibit perfect periodicity, which makes the analysis of parasitic reflections much more complex.

Last, generalized SIM with the tuned global reflection coefficient presented advantages when compared to classical SIM for one specific configuration (for $\theta_i = 0^\circ$ and $\theta_r = 60^\circ$). Complementary analysis for some other configurations (at oblique incidence for example) should be taken into consideration in order to confirm the interest of using a tuned global reflection coefficient.

Publications

International Journal Articles:

1. H. Haddad, R. Loison, R. Gillard, A. Harmouch, A. Jrad, "A combination of transformation optics and surface impedance modulation to design compactretrodirective reflectors", AIP Advances, 025114, 8 : 2, 10.1063/1.5020204,2018.

International Conferences:

1. H. Haddad, R. Loison, R. Gillard, A. Jrad, A. Harmouch., "Compression technique for retrodirective reflectors using transformation optics", MECAP2016, Sep 2016, Beirut, Lebanon. pp.1 - 4, IEEE, 10.1109/MECAP.2016.7790081.
1. H. Haddad, R. Loison, R. Gillard, A. Jrad, A. Harmouch., " Mitigation of Parasitic Reflections over Periodic Surface Impedance Modulated Panels", EUCAP2019, Krakow, Poland, April, 2019. (Accepted paper)

National Conferences:

2. H. Haddad, R. Loison, R. Gillard, A. Jrad, A. Harmouch., "*Combinaison de l'Optique de Transformation (OT) et de la Modulation d'Impédance de Surface (MIS) pour la Conception des Réflecteurs Rétrodirectifs Aplatis*", GDR-Ondes, Sophia Antipolis, France, Oct., 2017.
3. H. Haddad, R. Loison, R. Gillard, A. Jrad, A. Harmouch., "*Technique de Compression pour les réflecteurs en utilisant l'optique de transformation*", JNM, Saint-Malo, France, May, 2017.
4. H. Haddad, R. Loison, R. Gillard, A. Jrad, A. Harmouch., " Réduction des réflexions parasites produites par des panneaux à modulation périodique *d'impédance de surface*", JNM, Caen, France, May, 2019. (Accepted paper)

Bibliography

- [1] J. Stastny, S. Cheung, G. Wiafe, K. Agyekum, H. Greidanus, “Application of RADAR Corner Reflectors for the Detection of Small Vessels in Synthetic Aperture Radar”, in IEEE Journal of Selected Topics in App. Earth Obs. and Remote Sensing, vol. 8, no. 3, pp. 1099-1107, (2015).
- [2] K. Sarabandi, Tsen-Chieh Chiu, “Optimum corner reflectors for calibration of imaging radars”, IEEE Transactions on Antennas and Propagation, Volume: 44, Issue: 10, pp. 1348-1361, (1996).
- [3] E. F. Knott, J. Shaeffer, and M. Tuley, “Radar Cross Section ”, 2nd edition, SciTech Publishing (2004).
- [4] Leonhardt, U. Optical conformal mapping. Science 312, 1777–1780 (2006).
- [5] Pendry, J. B., Schurig, D. & Smith, D. R. Controlling electromagnetic fields. Science 312, 1780 1782 (2006).
- [6] D. Werner and D.-H. Kwon, Transformation Electromagnetics and Metamaterials. London: Springer, (2014).
- [7] N. B. Kundtz, D. R. Smith, and J. B. Pendry, “Electromagnetic design with transformation optics,” Proc. IEEE, vol. 99, no. 10, pp. 1622–1633, (2011).
- [8] J. B. Pendry “Perfect Cylindrical Lenses,” Optics Express, vol. 11, no. 7, pp. 755-760, (2003).
- [9] D. Kwon and D. H. Werner “Flat Focusing Lens Designs Having Minimized Reflection Based on Coordinate Transformation Techniques,” Optical Express, vol. 17, no. 10, pp. 7807-7817, (2009).
- [10] Li, J. & Pendry, J. B. Hiding under the carpet: A new strategy for cloaking. Phys. Rev. Lett. 101,203901 (2008).
- [11] Y. Feng, Shuai Xiong, Bo Zhu, J. Zhao and T. Jiang, “Design and realization of planar reflectors through transformation optics”, 2013 International Workshop on Antenna Technology (iWAT), Karlsruhe, pp. 187-190, (2013)
- [12] D. H. Kwon and D. H. Werner, “Transformation optical designs for wave collimators, flat lenses and right-angle bends,” New J. Phys. 10, 115023 (2008).
- [13] E. G. Post, “Formal Structure of Electromagnetics: General Covariance and Electromagnetics”, New York: Interscience Publishers, (1962).
- [14] I. Gallina, G. Castaldi, and V. Galdi, “Transformation Media for Thin Planar Retrodirective Reflectors”, IEEE Antennas Wireless Propag. Lett. 7, 603–605 (2008).

- [15] S. Xiong, Y. Feng, T. Jiang, & J. Zhao, "Designing retrodirective reflector on a planar surface by transformation optics", *AIP Advances*, 3, 012113 (2013).
- [16] V. G. Veselago, "The Electrodynamics of Substances with Simultaneously negative values of ϵ and μ ," *Sov. Phys. Usp.*, vol. 10, pp. 509-514, (1968).
- [17] R. A. Shelby, D. R. Smith, and S. Schultz, "Experimental verification of a negative index of refraction", *Science*, vol. 292, no. 5514, pp. 77-79, (2001).
- [18] D. R. Smith, W. J. Padilla, D. C. Vier, S. C. Nemat-Nasser, and S. Schultz, "Composite medium with simultaneously negative permeability and permittivity", *Phys. Rev. Lett.*, vol. 84, pp. 4184-4187, (2000).
- [19] H. S. Chen, Bl Wu, B. Zhang, J.A. Kong, "Electromagnetic wave interactions with a metamaterial cloak", *Phys. Rev. Lett.* 99, 063903 (2007).
- [20] H. S. Chen, C.T. Chan, P. Sheng, "Transformation optics and metamaterials", *Nature Materials* volume 9, pages 387–396 (2010).
- [21] S. Maci, G. Minatti, M. Casaletti, and M. Bosiljevac, "Metasurfing: Addressing waves on impenetrable metasurfaces", *IEEE Antennas and Wireless Propagation Letters*, vol. 10, pp. 1499-1502, (2011).
- [22] Huang, J., and Encinar, J., "Reflectarray antennas", John Wiley & Sons, (2007).
- [23] D. R. Jackson and N. G. Alexopoulos, "Gain enhancement methods for printed- circuit antennas", *IEEE Transactions on Antennas and Propagation*, vol. 33, pp. 976-987, (1985).
- [24] A. P. Feresidis and J. C. Vardaxoglou, "High gain planar antenna using optimized partially reflective surfaces", *IEEE Transactions on Antennas and Propagation*, vol. 148, pp. 345-350, (2001).
- [25] D. R. Jackson and A. A. Oliner, "A leaky-wave analysis of the High-Gain Printed Antenna Configuration", *IEEE Transactions on Antennas and Propagation*, vol. 36, pp. 905-910, (1988).
- [26] A. P. Feresidis, G. Goussetis, S. Wang, and J. C. Vardaxoglou, "Artificial Magnetic Conductor Surfaces and Their Application to Low-Profile High-Gain Planar Antennas", *IEEE Transactions on Antennas and Propagation*, vol. 53, pp. 209-215, (2005).
- [27] N. Yu, P. Genevet, M. A. Kats, F. Aieta, J.-P. Tetienne, F. Capasso, and Z. Gaburro, "Light propagation with phase discontinuities: Generalized laws of reflection and refraction", *Science* 334, 333, (2011).
- [28] D.M.Pozar, S.D.Targonski and H.D.Syrigos, "Design of millimeter wave microstrip reflectarrays", *IEEE Transactions on Antenna and Propagation*, Vol.45, No.2, pp.287-295, (1997).

- [29] S.Xu, H.Rajagopalan, Y.Rahmat-Samii and W.A. Imbriale, "A novel reflector surface distortion compensating technique using a sub-reflectarray", IEEE International Symposium on Antenna and Propagation, pp.5315-5318, (2007).
- [30] R.D. Javor, X.D. Wu, "Offset-fed microstrip reflectarray antenna", Electronics letters, vol. 30, no. 17, pp. 1363-1365, (1994).
- [31] R.D. Javor, X.D. Wu, "Design and Performance of a Microstrip Reflectarray Antenna," IEEE Transactions on Antennas and Propagation, vol. 43, no. 9, pp. 932-939, (1995).
- [32] D. M. Pozar and T. A. Metzler, "Analysis of a reflectarray antenna using microstrip patches of variable size," Electronics Letters, vol. 29, no. 8, pp. 657-658, (1993).
- [33] M. R. Chaharmir, J. Shaker, N. Gagnon, and D. Lee, "Design of Broadband, Single Layer Dual- Band Large Reflectarray Using Multi Open Loop Elements," IEEE Transactions on Antennas and Propagation, vol. 58, no. 9, pp. 2875-2883, (2010).
- [34] L. Moustafa, R. Gillard, F. Peris, R. Loison, H. Legay, and E. Girard, "The Phoenix Cell: A New Reflectarray Cell With Large Bandwidth and Rebirth Capabilities", IEEE Trans. Antennas And Wireless Propag. Letters, vol. 10, (2011).
- [35] D. Cadoret, A. Laisne, R. Gillard, H. Legay, "A New Reflectarray Cell Using Microstrip Patches Loaded with Slots," Microwave and Optical Technology Letters, vol. 44, Issue 3, pp. 270-272, (2005).
- [36] J. A. Encinar, and J. A. Zornoza, "Broadband Design of Three-Layer Printed Reflectarrays," IEEE Transactions on Antennas and Propagation, vol. 51, no. 7, pp. 1662-1664, (2003).
- [37] B. Wu, A. Sutinjo, M. E. Potter, and M. Okoniewski, "On the Selection of the Number of Bits to Control a Dynamic Digital MEMS Reflectarray," IEEE Antennas and Wireless Propagation Letters, vol. 7, pp. 183-186, (2008).
- [38] H. Salti, E. Fourn, R. Gillard, and H. Legay, "Minimization of MEMS Breakdown Effects on the Radiation of a MEMS Based Reconfigurable Reflectarray," IEEE Transactions on Antennas and Propagation, vol. 58, no. 7, pp. 2281-2287, (2010).
- [39] J. Song, J. Wang, K. Peng, C. Pan, and Z. Yang, "Quantization Error Reduction for the Phased Array with 2-bit Phase Shifter," Wireless Personal Communication, vol. 52, no. 1, pp. 29-41, (2010).
- [40] D. M. Pozar, "Wideband reflectarrays using artificial impedance surfaces," Electronics Letters, vol. 43, no. 3, pp. 148-149, (2007).
- [41] G. Zhao, Y. C. Jiao, F. Zhang, and F. S. Zhang, "A Subwavelength Element for Broadband Circularly Polarized Reflectarrays," IEEE Antennas and Wireless Propagation Letters, vol. 9, pp. 330-333, (2010).

- [42] J. Ethier, M. R. Chaharmir, and J. Shaker, "Reflectarray design comprised of sub-wavelength coupled-resonant square loop elements," *Electronics Letters*, vol. 47, no. 22, pp. 1215-1217, (2011).
- [43] D. Lipuma, S. Meric, R. Gillard, "RCS enhancement of a flattened dihedral corner reflector using a reflectarray approach", *IET Electronic Letters*, Vol. 49, Issue 2, pp. 152 – 154, (2013).
- [44] I.L. Morrow, K. Morrison, M. Finnis, and W. Whittow. "A low profile retrodirective frequency selective surface for radar earth observation", *LAPC, Loughborough*, pages 1–4. *IEEE*, (2015).
- [45] H. Srour, R. Gillard, S. Meric, D. Seetharamdoo, "Improved Retrodirective Flattened Dihedral Using Incidence Angle Correction". *LAPC, Loughborough, UK*, pages 1–4. *IEEE*, doi: 10.1109/LAPC.2016.7807511, (2016).
- [46] H. Srour, R. Gillard, S. Méric and D. Seetharamdoo, "Analysis of the retrodirective mechanism of a flattened dihedral", *IET Microwaves, Antennas & Propagation*, vol. 12, no. 5, pp. 699-705, doi: 10.1049/iet-map.2017.0491, (2018).
- [47] M.Mussetta, P.Pirinoli, R.E.Zich and M.Orefice, "Design of printed microstrip reflectarrays reducing the groundplane reflection", *Proceedings URSI General Assembly, New Delhi, India*, (2005).
- [48] J.Budhu and Y.Rahmat-Samii,"Understanding the appearance of specular reflection in offset fed reflectarray antennas", *IEEE International Antenna and Propagation Symposium Digest*, pp.97-100, USA, (2011).
- [49] R.El-Hani and J.Laurin, "Phase analysis for off-specular reflectarray antennas", *IEEE International Antenna and Propagation Symposium Digest*, pp.380-383, USA, (2011).
- [50] R.El-Hani and J.Laurin, "Specular reflection analysis for off-specular reflectarray antennas", *IEEE Transactions on Antenna and propagation*, Vol.61, No.7, pp.3582 – 3588, (2013).
- [51] R.Romanovsky, "Cellular reflectarray antenna and method of making same", *US Patent 7,791,522*, (2010).
- [52] F. Kong, B. I. Wu, J. A. Kong, J. Huangfu, S. Xi, and H. Chen, "Planar focusing antenna design by using coordinate transformation technology", *App. Phys. Lett.* 91, 253509 (2007).
- [53] Y. Luo, L. He, S. Zhu, Helen L. W. Chan, and Y. Wang, "Flattening of conic reflectors via a transformation method", *Phys. Rev. A* 84, 023843 (2011).
- [54] D. Schurig, J. B. Pendry, and D. R. Smith, "Calculation of material properties and ray tracing in transformation media", *Opt. Express* 14, 9794-9804 (2006).

- [55] R. E. Collin and J. Brown, "The Design of Quarter-Wave Matching Layers for Dielectric Surfaces", *Proceedings of the IEE - Part C: Monographs*, vol. 103, no. 3, pp. 153-158, (1956).
- [56] Wood, B., Pendry, J. B. & Tsai, D. P. "Directed subwavelength imaging using a layered metal-dielectric system", *Phys. Rev. B* 74, 115116 (2006).
- [57] E. Tuncer, "Dielectric mixtures: Importance and theoretical approaches", Niskayuna NY, 12309, USA, arXiv:1304.5516, (2013).
- [58] S. J. Orphanidis, "Electromagnetic Waves and Antennas", Piscataway, NJ 08854-8058, USA, (2016).
- [59] S. Maci, G. Minatti, M. Casaletti, and M. Bosiljevac, "Metasurfing: Addressing waves on impenetrable metasurfaces," *IEEE Antennas and Wireless Propagation Letters*, vol. 10, pp. 1499-1502, (2011).
- [60] J. Huang, J. A. Encinar, *Reflectarray Antennas*, USA, NJ, Hoboken-Piscataway: Wiley—IEEE Press, (2007).
- [61] A. M. Patel and A. Grbic, "A printed leaky wave antenna with a sinusoidally modulated surface reactance," *IEEE A. P. S.*, Charleston, SC, (2009).
- [62] G. Minatti, F. Caminita, M. Casaletti and S. Maci, "Spiral Leaky-Wave Antennas Based on Modulated Surface Impedance, " *IEEE Transactions on Antennas and Propagation*, vol. 59, no. 12, pp. 4436-4444, (2011).
- [63] N. Mohammadi Estakhri and A. Alù, "Wave-front Transformation with Gradient Metasurfaces", *Phys. Rev. X* 6, 041008, (2016).
- [64] V. S. Asadchy, M. Albooyeh, S. N. Tsvetkova, A. Díaz-Rubio, Y. Ra'di, and S. A. Tretyakov, "Perfect Control of Reflection and Refraction Using Spatially Dispersive Metasurfaces", *Phys. Rev. B* 94, 075142, (2016).
- [65] J. Lekner, "Theory of Reflection, of Electromagnetic and Particle Waves", Springer, ISBN 9789024734184 (1987).
- [66] N. Mohammadi Estakhri and A. Alù, "Manipulating Optical Reflections Using Engineered Nanoscale Metasurfaces", *Phys. Rev. B* 89, 235419 (2014).
- [67] A. G. Roederer, "Reflectarray antennas", 3rd European Conference on Antennas and Propagation, Berlin, pp. 18-22, (2009).
- [68] H. Rajagopalan and Y. Rahmat-Samii, "Reflectarray antennas: An intuitive explanation of reflection phase behavior", XXXth URSI General Assembly and Scientific Symposium, Istanbul, , pp. 1-4, (2011).

- [69] Bryan H. Fong, Joseph S. Colburn, John J. Ottusch, et al. “Scalar and Tensor Holographic Artificial Impedance Surfaces”, *IEEE Trans. Antennas and Propagation*, 56, pp.1624-1632, (2010).
- [70] L. Matekovits and Y. Ranga, “Controlling the phase of the scattered and/or radiated field from a high impedance surface of quasi-periodic sequences”, *IEEE Antennas Wireless Propag. Lett.*, vol. 12, pp. 321–324, (2013).
- [71] C. L. Holloway, E. F. Kuester, J. A. Gordon, J. O’Hara, J. Booth, and D. R. Smith, “An overview of the theory and applications of metasurfaces: The two-dimensional equivalents of metamaterials”, *IEEE Antennas Propag. Mag.* 54, 10, (2012).
- [72] D. J. Gregoire, “Impedance modulation patterns for artificial-impedance surface antennas,” in *Proc. IEEE Antennas Propag. Soc. Int. Symp.*, Orlando, FL, USA, pp. 2339–2340, (2013).
- [73] Y. Zhang et al., “Conformal antennas based on holographic artificial impedance surfaces,” in *Proc. IEEE Antennas Propag. Soc. Int. Symp.*, pp. 1552–1553, (2014).
- [74] L. Jiang, Y. Chun, C. Qi and L. Bo, “Millimetre wave circularly polarized holographic antenna based on artificial impedance surface”, *IET International Radar Conference 2015*, Hangzhou, pp. 1-3, (2015).
- [75] A. Díaz-Rubio, V. S. Asadchy, A. Elsakka, Sergei A. Tretyakov, “From the generalized reflection law to the realization of perfect anomalous reflectors,” *Science Advances*, Vol. 3, no. 8, e1602714, (2017).
- [76] A. Pors, S. I. Bozhevolnyi, “Plasmonic metasurfaces for efficient phase control in reflection”. *Opt. Express* 21, 27438–27451, (2013).
- [77] M. Esfandyarpour, E. C. Garnett, Y. Cui, M. D. McGehee, M. L. Brongersma, “Metamaterial mirrors in optoelectronic devices”. *Nat. Nanotechnol.* 9, 542–547, (2014).
- [78] D.H. Kwon, S.A. Tretyakov, “Perfect reflection control for impenetrable surfaces using surface waves of orthogonal polarization”, *Phys. Rev. B* 96, 085438, (2017).
- [79] D. S. Goshi, K. M. K. H. Leong and T. Itoh “Recent advances in retrodirective system technology”, *IEEE Radio and Wireless Symposium*, pp. 459-462, (2006).

AVIS DU JURY SUR LA REPRODUCTION DE LA THESE SOUTENUE

Titre de la thèse:

Techniques de contrôle de la réflexion d'une onde plane à l'aide de l'optique de transformation et la modulation d'impédance de surface - application à l'aplatissement du réflecteur rétro-directif

Nom Prénom de l'auteur : HADDAD HASSAN

Membres du jury :

- Madame MAZE-MERCEUR Geneviève
- Monsieur GILLARD Raphaël
- Monsieur LOISON Renaud
- Monsieur LHEURETTE Eric
- Madame RICHALOT Elodie
- Monsieur JRAD Akil

Président du jury : *Elodie RICHALOT*

Date de la soutenance : 27 Novembre 2018

Reproduction de la these soutenue

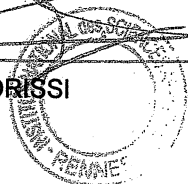
- Thèse pouvant être reproduite en l'état
 Thèse pouvant être reproduite après corrections suggérées

Fait à Rennes, le 27 Novembre 2018

Signature du président de jury

Le Directeur,

M'hamed DRISSI



E. Richalot
E. RICHALOT

Titre : Techniques de contrôle de la réflexion d'une onde plane à l'aide de l'optique de transformation et la modulation d'impédance de surface - Application à l'aplatissement du réflecteur rétro-directif.

Mots clés: Réflecteur Rétro-directif, Dièdre, Optique de transformation, Modulation d'impédance de surface, Lobes parasites.

Résumé: Ces dernières années, un intérêt croissant est porté aux réflecteurs rétro-directifs aplatissés dans le but de remplacer le réflecteur diédrique conventionnel, trop encombrant pour de nombreuses applications.

Dans un premier temps, cette thèse étudie deux techniques différentes permettant de réduire l'épaisseur d'un réflecteur diédrique. L'Optique de transformation modifie la constitution matérielle de son volume intérieur alors que la modulation d'impédance de surface introduit une distribution d'impédance à sa surface. On examine également la possibilité de combiner ces deux techniques pour tirer le meilleur parti de chacune d'elle.

La deuxième partie de cette thèse étudie l'origine des réflexions parasites pour les panneaux utilisant la modulation d'impédance de surface et propose de nouvelles règles de conception pour atténuer leurs niveaux. Finalement, une mise en œuvre pratique est proposée pour une modulation d'impédance de surface généralisée qui utilise des impédances complexes et surpasse les performances de la modulation d'impédance classique.

Title : Reflection control techniques of a plane wave using transformation optics and surface impedance modulation - Application to the flattening of the retro-directive reflector.

Keywords: Retrodirective Reflector, Dihedral, Transformation Optics, Surface Impedance Modulation, Parasitic lobes.

Abstract: In recent years, increasing interest in compact reflectors with retrodirective response is perceived since the conventional dihedral reflector is too bulky to be integrated within most applications.

First, this thesis investigates two different techniques that might lead to lower profiles of the dihedral reflector. It explores the use of Transformation Optics that modifies the filling volume of such a device and Surface Impedance Modulation that introduces an impedance distribution over its surface. It also inspects the possibility of combining those two techniques to take benefit of their complementary advantages.

The second part of this thesis investigates the source of parasitic lobes for surface impedance modulated panels and proposes new design rules to mitigate their levels. Finally, it also proposes a practical implementation for a specific setting of the generalized surface impedance modulation that makes use of complex impedances and outperforms a panel implementing the classical modulation.